Gallium Nitride-based Device Simulation and Development

Dottorando:
Stefano Russo

Relatore:
Prof. Aldo Di Carlo

Coordinatore di Dottorato
Prof. Giancarlo Cardarilli

Università di Tor Vergata
Dottorato in Sistemi e Tecnologie per lo Spazio

Contents

Chapter 1

Introduction

Since its reappearance in the early 1990s gallium nitride (GaN) has been regarded as a very interesting and highly promising material system for both optical and microwave high-power electronic applications. Over the last fifteen years researchers all around the world have made great efforts in order to redeem these promises. GaN-based optical applications have first reached the stage of commercialization while microwave high-power electronics are on the verge of their commercial breakthrough. The value of the worldwide GaN device market, which at present is about $3.5 billion, is estimated to be $7.2 billion by the year 2009.

This chapter will start with highlights of GaN research history. After this we will put GaN into perspective with conventional semiconductors and other wide-bandgap (WBG) materials. Among others we will give an overview of the application areas and the state-of-the-art of GaN-based microwave high-power electronics. Finally, we will discuss the objectives and organization of this thesis.

1.1 Highlights of Gallium Nitride research history

The material system of interest in this thesis is the wide-bandgap III-V compound semiconductor gallium nitride (GaN). GaN was first synthesized by Juza and Hahn in the 1930s by passing ammonia (NH_3) over liquid gallium (Ga) at elevated temperatures [1]. This method resulted in a powder consisting of small needles and platelets. Their purpose was to investigate the crystal structure and lattice constant of GaN. Due to the lack of a native GaN substrate no vapor phase epitaxial growth had ever been attempted.

In 1968, Maruska and Tietjen were the first to try the hydride vapor phase epitaxy (HVPE) approach to grow centimeter-sized GaN layers on sapphire substrates. In a traditional HVPE reactor the group III element such as Ga is transported as the monochloride. For example, gallium chloride (GaCl) is generated in situ by passing hydrochloric acid vapor ($HCl_{(g)}$) over liquid Ga. The group V element such as nitrogen (N) is transported as the hydride. Sapphire was chosen as substrate material because it is a robust material that is not reactive with ammonia. To date, sapphire has remained a very popular substrate for heteroepitaxial GaN growth.

The early HVPE GaN films were grown at temperatures below 600°C to prevent decomposition. However, these films were all polycrystalline. In 1969, Maruska realized that in an ammonia environment at temperatures above 600°C GaN growth actually would occur instead of decomposition. He increased the growth temperature to 850°C, the temperature typically used for gallium arsenide (GaAs), and obtained the first single crystalline GaN film [2]. The film quality could even be improved by increasing the temperature to 950°C. All GaN films grown at that time showed very high electron concentrations ($1020\ cm^{-3}$) even without intentional doping. The responsible n-type donors were believed to be nitrogen vacancies (V_N), a concept that has caused a lot of controversy over the years. Eventually oxygen (O_2) has been proposed as the responsible donor. Oxygen with its six valence electrons on an N site (N has five valence electrons) would be a single donor [3].

In order to create a pn junction a suitable p-type dopant had to be found. Zinc (Zn) seemed to be an appropriate acceptor as it worked for GaAs and gallium phosphide (GaP). Although heavy Zn concentrations rendered GaN films to be insulating, the films never became conducting p-type.

Despite of this, Pankove et al. achieved the first GaN light emitting diode (LED) in 1971. This device consisted of an undoped n-type region, an insulating Zn-doped layer and an indium (In) surface contact. It could emit blue, green, yellow or red light depending on the Zn concentration in the light emitting region [4]. In 1972, Maruska was the first to propose magnesium (Mg) to be a better choice of p-type dopant than Zn. Using the same device structure as Pankove, Maruska grew the first HVPE GaN LED, emitting at a wavelength of 430 nm (violet) with Mg as the luminescent center [5]. Although Mg-doped devices (GaN:Mg) were much brighter than

their Zn-doped equivalents, they were never very efficient (< 1 %) and no successful commercial product ever appeared. Nevertheless, Mg-doping has remained the basis for all commercial GaN-based LEDs and laser diodes (LDs) to date.

In the late 1970s, GaN research ceased virtually everywhere because of the continuing difficulties encountered with the growth of high quality films needed for device development. Remaining issues were the choice and availability of a suitable substrate, how to control the very high intrinsic n-type conductivity, and difficulties with obtaining conducting p-type GaN films. In 1982 only a handful of papers were published world-wide on this material system.

It was the perseverance of Isamu Akasaki that eventually resulted in obtaining conducting p-type GaN films in 1989. The conducting p-type films were discovered during cathodoluminescence (CL) observations of GaN:Mg in a scanning electron microscope (SEM). A photoluminescence (PL) study of the GaN:Mg material before and after low-energy electron beam irradiation (LEEBI) treatment showed that luminescence efficiency had increased by two orders of magnitude [6]. A Hall effect measurement indicated that the film had become p-type and conducting. The explanation for this phenomenon was given by Van Vechten et al. in 1992 who proposed that the shallow acceptor level of Mg was compensated by a hydrogen atom complexing with the Mg acceptor [7]. This Mg:H complex passivates the acceptor and prohibits p-type conduction. The energy of the electron beam breaks up this complex and enables Mg to be a shallow acceptor approximately 0.16 eV above the valence band [8]. In 1992, Nakamura et al. discovered that annealing GaN:Mg above 750°C in nitrogen (N2) ambient or vacuum also converted the material to conducting p-type. However, annealing in NH3 reintroduced atomic hydrogen and rendered GaN:Mg insulating again [9].

In 1986, a milestone was achieved when Amano et al. reported highly improved surface morphology, and optical and electrical properties of GaN films grown by metal organic chemical vapor deposition (MOCVD) on sapphire substrates through the use of a low-temperature (600°C) aluminum nitride (AlN) nucleation layer. This layer is grown between the sapphire substrate and the bulk GaN film, which is typically grown at 1050°C [10]. In 1991, Shuji Nakamura of the Japanese company Nichia Chemical Industries Ltd. (now Nichia Corp.) extended this concept with the introduction of a low-temperature (450–600°C) GaN nucleation layer.

The reason for this was that the large lattice mismatch between the low-temperature AlN nucleation layer and the following GaN film could cause defect generation and that the use of a low-temperature GaN nucleation layer would prevent this [11]. To date, MOCVD is the workhorse for the growth of GaN and related materials.

The breakthroughs achieved by Amano, Akasaki and Nakamura have lead to the revival of the GaN material system in the early 1990s. Researchers in the fields of optical and microelectronic applications showed renewed interest in GaN as most well-developed semiconductors, e.g. silicon (Si) and GaAs, approached their theoretical limits and the great potential of GaN predicted tremendous performance enhancement over these existing technologies. In 1991, Khan et al. reported first evidence for two-dimensional electron gas (2DEG) formation at an $Al_xGa_{1-x}N$/GaN heterojunction grown by MOCVD on sapphire [12]. The first GaN metal semiconductor field-effect transistor (MESFET) and heterostructure field-effect transistor (HFET) grown by MOCVD on sapphire substrates were reported in 1993 and 1994, respectively by Khan et al. [13, 14]. In 1993, Nakamura et al. demonstrated the first high-brightness (HB) blue double-heterostructure (DH) GaN LEDs [15]. In 1996, Nakamura et al. reported the first continuous wave (CW) blue GaN LD [16]. Since these giant steps in material and device development, both research and commercial GaN activities have gained enormous attention. GaN-based optical applications have first reached the stage of commercialization while microwave high-power electronics are on the verge of their commercial breakthrough. Producibility, reproducibility and reliability of the epitaxial material and process technologies are key issues that need to be addressed to redeem the great promises GaN-based devices hold.

1.2 GaN put into perspective

Relevant questions that have to be answered when choosing any particular semiconductor material system are:

• What are the advantages and disadvantages over existing material systems for the intended application?

• What are the application areas?

• What are the costs and the expected market-value?

We will answer these questions in the following subsections.

1.2.1 Advantages and disadvantages of GaN

In this subsection we will answer the question what are the advantages and disadvantages of GaN by comparing its basic material properties with those of conventional semiconductors like Si, GaAs, and InP and other wide-bandgap (WBG) materials such as SiC and diamond. Furthermore we will compare GaN devices to existing and competing alternatives.

Material properties

Table 1.1 shows the fundamental material properties of GaN, SiC, diamond, Si, GaAs, and InP that are most important to electronic device performance [17- 19].

A large bandgap energy (Eg) results in high electric breakdown fields (Ec), which enable the application of high supply voltages. Furthermore, it allows the material to withstand high operating temperatures and provides for improved radiation hardness. GaN and SiC have bandgap energies about two to three times those of conventional semiconductors such as Si, GaAs, and InP. The electric breakdown fields for the WBG materials are excellent and very high, typically one order of magnitude larger than for the conventional semiconductors.

Generally, to achieve high currents and high frequency operation, high charge carrier mobility (μ) and high saturation velocity (vsat) are desirable. The high value for electron mobility of GaAs (8500 cm^2/Vs) is the main reason that field-effect transistors (FETs) fabricated from this material have such excellent high-frequency performance.

A primary disadvantage of fabricating transistors from bulk GaN and SiC is the relatively low values for the electron mobilities, which are 900 cm^2/Vs for GaN and depending on the polytype approximately 700 cm^2/Vs for SiC. However, these values are sufficient for transistors specifically designed for high-power operation. In general, WBG semiconductors have relatively low mobility but very high values for the saturation velocity, which is reached at high electric fields that can easily be supported.

The mobility and saturation velocity of the 2DEG at the $Al_xGa_{1-x}N/GaN$ heterojunction is very suitable for high-power, high-frequency device applications. The room temperature (RT) mobility of the 2DEG, which is typically between 1200 cm^2/Vs and 2000 cm^2/Vs, is significantly better than that of bulk GaN and SiC. The 2DEG sheet charge density (ns) of the $Al_xGa_{1-x}N/GaN$ structure is very high (experimental values up to 1×10^{13} cm^{-2}) due to piezoelectric and spontaneous polarization induced effects. The measured sheet charge density is about a factor of 10 better than those of $Al_xGa_{1-x}As/In_xGa_{1-x}As$ and $In_xAl_{1-x}As/In_xGa_{1-x}As$ heterostructures.

The thermal conductivity (k) of a semiconductor material is extremely important since this parameter is a measure for the ease with which dissipated power can be extracted from the device. Poor thermal conductivity leads to degraded device operation at elevated temperatures. In general, conventional semiconductors are poor thermal conductors, particularly GaAs and InP. Conversely, SiC and especially diamond are excellent thermal conductors and GaN is comparable with Si, the best of the conventional semiconductors.

Property	GaN AlGaN/GaN	SiC	Diamond	Si	GaAs AlGaAs/ InGaAs	InP InAlAs/ InGaAs
Bandgap energy, E_g (eV)	3.44	3.26	5.45	1.12	1.43	1.35
Electric breakdown field, E_c (MV/cm)	3	3	10	0.3	0.4	0.5
Saturated (peak) velocity electrons, v_{sat} (v_{peak}) ($\times 10^7$ cm/s)	2.5 (2.7)	2.0 (2.0)	2.7	1.0 (1.0)	1.0 (2.1)	1.0 (2.3)
Electron mobility, μ_n ($cm^2/V \cdot s$)	900 2000^{α}	700	4800	1500	8500 $10{,}000^{\beta}$	5400 $10{,}000^{\chi}$
2DEG density, n_s ($\times 10^{13}$ cm^{-2})	1.0	N.A.	N.A.	N.A.	< 0.2	< 0.2
Thermal conductivity, κ (W/cm·K)	1.3 – 2.1	3.7 – 4.5	22	1.5	0.5	0.7
Relative permittivity, ε_r	9.0	10.1	5.5	11.8	12.8	12.5

$^{\alpha, \beta, \chi}$ values for the corresponding heterostructures.

Table 1.1: Material properties of conventional and wide-bandgap semiconductors at 300 K [17, 18, 19].

The relative permittivity (ε_r) is an indication of the capacitive loading of a transistor and affects the device terminal impedances. Table 1.1 shows that the values of ε_r for the WBG semiconductors are considerably lower than those for the conventional semiconductors. In the case of GaN and SiC the values of ε_r are about 20% lower whereas for diamond the value of ε_r is even about 55% lower. This permits for example a GaN device to be about 20% larger in area for a given impedance. As a consequence, this increased area enables the generation of larger currents and higher microwave output power.

For a better comparison of the possible high-power and high-frequency performance of different semiconductor materials, several figures of merit have been proposed. These figures of merit combine the most relevant material properties with respect to high-power and high-frequency applications into one number that represents a rough measure of the relative strengths of the alternative materials.

Johnson's figure of merit (JFOM) [20] takes into account the breakdown voltage and saturated electron drift velocity in defining a value for the high-frequency handling capability of a certain semiconductor. For GaN, the JFOM is 728 times that of silicon, about 93 times that of GaAs, and about twice that of SiC.

Baliga's figure of merit (BFOM) [21] is calculated based on the relative permittivity, electron mobility, and electric breakdown field and is a measure for the high-power handling capability. Based on its properties, the BFOM for GaN is about 133 times that of Si, 11 times that of GaAs and three times that of SiC [22].

Form these figures it is very clear that GaN offers much better high-power/high-frequency performance possibilities than GaAs and SiC. GaN devices compared to existing and competing alternatives.

Besides AlGaN/GaN HFETs a wide range of existing technologies for the generation of solid-state microwave power is available, including Si bipolar, Si laterally diffused metal oxide semiconductor (LDMOS), GaAs MESFET and pseudomorphic HFETs (pHFET), AlGaAs/InGaAs HFET, GaAs, InP, InGaP, and silicon germanium (SiGe) heterojunction bipolar transistors (HBT) as well as SiC MESFETs.

SiC MESFETs and GaN HFETs offer superior microwave performance compared to similar components fabricated from Si or GaAs, particularly at elevated temperatures. Microwave output power densities on the order of 4 - 7 W/mm and 10 - 12 W/mm are achievable from SiC MESFETs and GaN HFETs, respectively. For high-power/high-frequency applications GaAs has several major drawbacks. Among them are high substrate costs and low thermal conductivity. The latter makes it very difficult to effectively remove heat when used in high-power applications. An additional drawback is its critical electric field which is much smaller than that of the WBG materials. This explains why GaN HFETs can provide output power densities 10 times higher than GaAs pHFETs. SiC MESFETs benefit from the excellent thermal conductivity of the substrate. However, their electron mobility is significantly lower than that of GaN HFETs, which is related to the lack of heterojunction technology in this material system.

SiGe HBTs have found applications in many microwave and mixed-signal products where they offer high-performance, yet cost-effective, products previously unavailable on a Si platform. However, the SiGe HBT's device structure remains a relatively low-power configuration. The high-frequency performance exhibited by SiGe HBTs largely results from reduced minority carrier transit time through the base layer and reduced base resistance. To render this structure suitable for high-power applications, the collector layer would have to be made thicker up to a point where most of the advantages of the reduced base transit time would be eliminated because of a much larger collector delay. Therefore, SiGe HBTs are unlikely candidates for high-power/high-frequency applications. Si LDMOS transistors are the workhorses of today's base-station power amplifiers (PAs) owing to their excellent price-to-performance ratio compared with other commercially available technologies such as GaAs HFETs and Si bipolar junction transistors (BJTs).

Emerging third-generation (3G) wireless cellular networks are designed to provide high data rate services beyond traditional voice. To support these higher data rates, 3G air interfaces such as wide-band code-division multiple access (W-CDMA) place severe demands on the linearity of the base station power amplifiers and associated power transistors. The transistor linearity spec, which is commonly expressed in terms of the adjacent channel power ratio (ACPR), also known as the adjacent channel leakage ratio (ACLR), can be as stringent as -65 dBc.

ACPR is a measure for the amount of power spilling into the adjacent channels referenced to the power in the transmit channel. To achieve the required linearity W-CDMA transistors must operate with the power backed-off to well below their peak capability. For example, a state-of-the-art LDMOS transistor with a P_{1dB} rating of 180 W is capable of producing about 38 W (approximately 80 mW/mm) of linear power under W-CDMA modulation, at 28 V operation.

As GaN HFETs show much higher linearity than Si LDMOS, it may be possible on a system level to reduce the complexity of the linearization circuitry necessary for high-bandwidth wireless systems. As LDMOS technology is capable of providing only moderate power density, it is necessary to use devices with very large gate peripheries and correspondingly very low die impedances to realize the required large powers. As a consequence, the bandwidth of the matching circuit is reduced.

GaAs HFET manufacturers face an even more challenging task than their Si counterparts as the operating voltages (12 - 15 V) are lower, operating currents are higher and thermal conductivity is lower than Si.

All these issues can be circumvented by using a higher power density technology that enables higher total output power and increased bandwidth resulting from a more compact layout as in

the case of GaN-based HFETs. In this way a same-sized device can handle higher power that results in lower costs per watt of power and lower system costs. The higher impedance levels of these smaller devices considerably ease input matching and high-bandwidth design.

1.2.2 Application areas

The direct bandgap of GaN and its alloys enables the material to be used for both optical and electronic applications. At 300 K the bandgap of GaN is 3.44 eV which corresponds to a wavelength in the near ultra violet (UV) region of the optical spectrum. Figure 1.1 shows a plot of the bandgap energy versus lattice constant in combination with the visible optical spectrum for various semiconductors including the wide-bandgap materials SiC, GaN and its alloys indium nitride (InN) and aluminum nitride (AlN). It can be seen that the AlxInyGa1-x-yN alloys cover bandgap energies from 1.9 eV to 6.2 eV, which correspond to wavelengths ranging from red to deep UV.

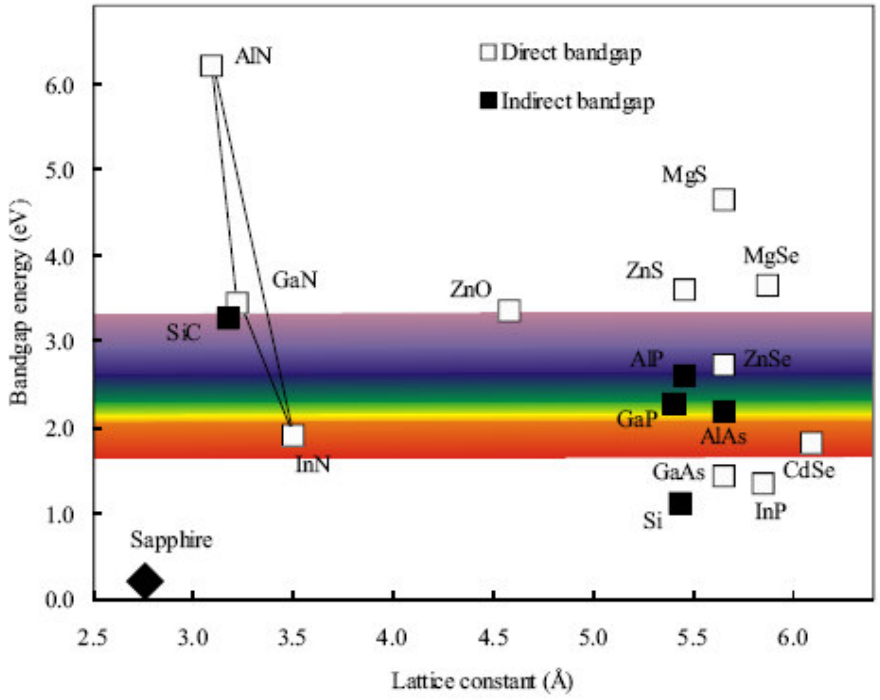

Figure 1.1: Bandgap energy versus lattice constant for various semiconductors including the wide-bandgap materials SiC and GaN with its alloys.

1.2.2.1 Optical applications

In 1968 James Tietjen, working at the Materials Research Division of the Radio Corporation of America (RCA), came up with the idea to develop a flat television that could be hung on the wall like a painting. A full color image can be created combining red, green, and blue pixels in the display. Red and green LEDs were available using gallium arsenide phosphide ($GaAs_{1-x}P_x$) and gallium phosphide nitride (GaP:N) materials, respectively. All that was missing to realise a flat LED-based television set was a bright blue LED.These devices became available using either SiC or II-VI compounds such as zinc oxide (ZnO). However, because of their indirect bandgap SiC LEDs were not very efficient. The devices based on II-VI compounds mainly suffered from much too short lifetimes for commercial applications. Hence these devices could not be used in the envisioned display application.

As stated in Sect. 1.1 this void in solid-state lighting was filled in 1993 by Nakamura et al.. By realizing high-brightness blue GaN-based LEDs that were about 100 times brighter than the previous blue SiC LEDs they made feasible the daylight visible full color display application.

LED applications

The main economical benefits of LED-based lighting are low power requirement, high efficiency, and long lifetime. In addition, solid-state design renders LEDs impervious to electrical and mechanical shock, vibration, frequent switching and environmental extremes. Several major markets are being addressed with these newly developed solid-state light sources. Automobile exterior lighting has been moving rapidly to incorporate transparent-substrate $Al_xIn_yGa_{1-x-y}P$ technology into high-mount braking lights and into the full amber and red-orange taillight assembly. Full-color, outdoor, changeable message signs and full-motion video displays have been adopting $Al_xIn_yGa_{1-x-y}N$ and $Al_xIn_yGa_{1-x-y}P$ technologies and will continue to proliferate as costs are reduced. Traffic-signal applications have begun to incorporate red AlInGaP and AlGaAs LEDs for traffic lights and are moving toward incorporating amber and blue-green LEDs to produce a completely LED-based signal head. All of these markets are rapidly expanding and will provide enormous growth opportunities in the future. By using multiple LEDs, an LED cluster lamp continues to provide light even if one or more emitters fail unlike when the filament breaks in an incandescent bulb. Taking also into account an average life span of more than 100,000 hours (approximately 11 years), LEDs operate reliably year after year and are an excellent replacement for incandescent bulbs in hard-to-reach places and environments that depend on reliable lighting (e.g. hospitals, airports). Furthermore, colored lenses or filters are not needed since LEDs emit colored light that is determined by the composition of the semiconductor material comprising the diode. As LEDs are an energy-efficient light source and are virtually maintenance free, the cost savings are substantial. Other important GaN-based LED applications are backlighting (cell phones, PDAs), white light (flashlights, car head lights), general lighting (interior and exterior), water purification systems, and medical (sensors, surgical goggles).

Laser applications

Infra-red AlGaAs-based and red AlInGaP-based laser diodes (LDs), such as those in today's CD and DVD systems, have been around for decades. To increase the storage capacity on a CD, the pit size must be made smaller. A shorter wavelength LD is required to focus onto the smaller pit size. The current generation of DVD systems uses a LD with an emission wavelength of 650 nm. In the last few years the market for DVD systems has increased rapidly. However, the majority of these systems is read-only and is based on a 5 mW AlInGaP LD emitting at 650 nm. For further advances in the market recordable DVD was an obvious necessity. This required higher output power from the 650 nm LD (typically 30 - 40 mW). To also achieve faster read/write speeds even higher powers are required. GaN-based blue-violet LDs with an emission wavelength of 405 nm will be the cornerstone of next-generation DVD player-recorders and optical high-density data-storage systems for computers.

Using these components it is already possible to write huge amounts of data (27 GB) on a single-layer 12 cm DVD disk which is almost six times the storage capacity possible with ordinary red LDs. This is enough to store more than two hours of high-definition (HD) video or 13 hours of standard-definition (SD) video. In 2003, Tokyo-based Sony Corporation was the first consumer electronics company to begin offering next-generation DVD recorders. Sony leads a consortium called Blu-ray Disc, which is pushing one of two competing standards for the design of the discs, players, and recorders that use blue GaN-based LDs. The consortium further consists of the following major consumer electronics companies: Hitachi, LG Electronics, Matsushita Electric Industrial, Pioneer, Royal Philips Electronics, Samsung Electronics, Sharp, and Thomson. The other standard, high-density DVD (HD-DVD), has been proposed by Toshiba, Sanyo, and NEC.

Other GaN-based LD applications are laser printing, projection displays, and medical. GaN-based blue LDs are used for the laser-induced fluorescence method (LIF) employing endogenous ("autofluorescence") and exogenous fluorophores. LIF is applied for clinical diagnosis in dermatology, gynecology, urology, lung tumors as well as for early dentin caries.

The LIF method, which is fundamental for many medical applications, uses excitation radiation with a wavelength around 400 nm that could only be applied using tunable dye lasers or titanium lasers. This makes it only adequate for laboratory investigations. Development of GaN-based LDs provides the possibility to design portable, compact diagnostic devices as multi-channel analyzers of fluorescence spectra and surface imaging devoted to clinical applications. The designed systems used for spectra measurement and registration of fluorescence images include LDs with an output power of 5 - 30 mW at wavelengths of 405 - 407 nm. Dentistry diagnosis is a new field in which GaN-based LDs can be applied. After induction with blue light, decreased autofluorescence intensity can be observed when dentin caries occur.

1.2.2.2 Electronic applications

With respect to electronics, GaN is an excellent option for high-power/high-temperature microwave applications because of its high electric breakdown field (3 MV/cm) and high electron saturation velocity (1.5 x 10^7 cm/s). The former is a result of the wide bandgap (3.44 eV at RT) and enables the application of high supply voltages, which is one of the two requirements for high-power device performance. In addition, the wide bandgap allows the material to withstand high operating temperatures (300°C – 500°C). A big advantage of GaN over SiC is the possibility to grow heterostructures, e.g. AlGaN/GaN. The resulting two-dimensional electron gas (2DEG) at the AlGaN/GaN heterojunction serves as the conductive channel. Large drain currents (> 1 A/mm), which are the second requirement for a power device, can be achieved because of the high electron sheet densities (1 x 1013 cm−2) and mobilities (1500 - 2000 cm^2/Vs). These material properties clearly indicate why GaN is a serious candidate for next-generation microwave high-power/high-temperature applications. Figure 1.2 shows an overview of GaN based micro-electronic applications.

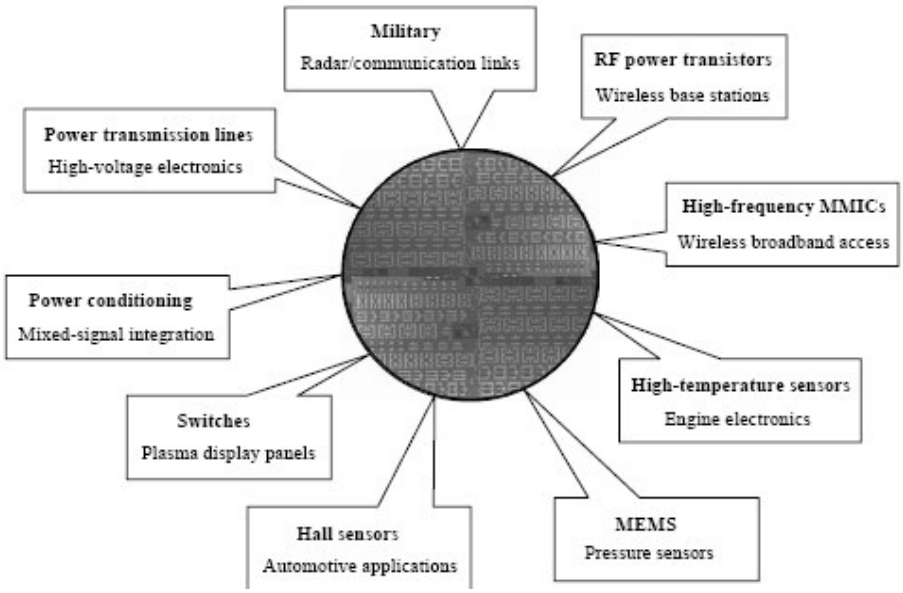

Figure 1.2: GaN-based micro-electronic applications.

Military applications

Despite the superior material properties and expected advances in device and system performance, the driving force behind research towards GaN-based microwave high-power/high-temperature electronics over the last decade has been almost exclusively military in nature. The main reason for this is the enormous costs that are involved with the early stages of GaN electronic device research. Several European countries, including France, Germany, United Kingdom, Italy, Spain, Sweden, and the Netherlands have defense oriented research

programs, some of which are joint efforts such as the Swedish - Dutch SiC and GaN program (period: 2000 - 2005) and the new very big European GaN program KORRIGAN (Key Organization for Research on Integrated Circuits in GaN Technology) (period: 2005 - 2009). The frontiers of academic and military research and the commercialization of GaN-based electronics however are mainly in the US and to a lesser extent in Japan. US and Japanese research programs towards military microwave systems have been and continue to be heavily funded by the respective Departments of Defense (DoD). The US's Defense Advanced Research Projects Agency (DARPA) has granted a huge GaN program, total investment up to $144.5 million, with a triple-pronged approach to speed up the development of GaN-based microelectronics and assure a rapid transition into military systems. Former research programs have focused on achieving hero values with respect to current densities and output power densities at microwave frequencies in order to prove the high expectations. The new programs however start for the basics (material growth, etching, contacts) and move through the stage of discrete devices to the eventual goal of GaN-based microwave monolithic integrated circuits (MMICs). The focus now is on understanding the physical reasons behind device failures and the development of physical models to predict performance in order to increase reproducibility and reliability.

In general, defense research programs focus on the development of GaN technology for use in components such as surface radars, broadband seekers, jammers, battlefield communication, satellite communication links, transmit/receive modules, broadband high-power amplifiers (HPAs), and low noise amplifiers (LNAs).

The frequencies of interest for these applications range from 2 GHz - 40 GHz.

Commercial applications

Commercial GaN-based applications are on the verge of their breakthrough. The first products will most probably be high-efficiency and high-linearity power amplifiers for base-stations, which power 3G wireless broadband cellular networks in the so-called S-band (2 GHz - 4 GHz). The US-based company RF Micro Devices (RFMD), the biggest player in this field, announced that it has sampled 100 W GaN amplifiers to customers early 2005. Competition can be expected from Japanese companies Fujitsu, Matsushita Electric, and OKI Electric. Other high-volume commercial applications in which GaN-based electronics could lead to significant performance enhancement and cost reduction are high-frequency MMICs (wireless broadband communication links), hybrid electric vehicles (DC-AC conversion), high temperature electronics (automotive, energy production), switches (plasma display panels, low-frequency high-power switching), high-voltage power rectifiers (inverter modules), microelectro-mechanical systems, MEMS (pressure sensors), and Hall sensors (automotive applications). Current hybrid electric vehicle (HEV) platforms, which use silicon-based power electronics, are faced with two major challenges: size and weight. In addition to traditional cars containing internal combustion engines (ICEs), HEVs must also accommodate power electronics, energy storage, and an electric motor in the predefined volume of the automobile platform. The HEV's motor drive, a power-electronics component that converts stored energy into an alternating-current (AC) source needed to operate the electric motor, is one of the main contributors to the system's size and weight. Typically, HEV motor drives use silicon insulated gate bipolar transistors (IGBTs) for the primary switching element, with Si p-i-n diodes as the fly-back diode, configured in a module designed to control three-phase motors. The module is positioned inside the engine compartment as close to the electric motor as possible to minimize parasitic inductance and reduce cabling weight. However, like all silicon devices they are limited to junction temperatures of 150°C – 175°C. Controlling the junction temperature of the Si electronics in the engine compartment's harsh environment requires large heat sinks and liquid cooling, but both these solutions are costly and difficult to integrate into the volume available within the engine compartment. The temperature limitations inherent to Si technology mean that state-of-the-art Si electronic components cannot meet the demands of HEV platforms to produce smaller, lighter, and cheaper electrical systems. Besides the great opportunities that GaN-based

high-temperature electronics present to HEVs, they also offer important capabilities to aerospace, energy production, and other industrial systems that will affect modern everyday life. The inherent ability of a GaN junction to properly rectify with low reverse leakage current at junction temperatures as high as 600°C enables power-device operation at higher ambient temperatures. In addition, superior power switching properties of WBG devices are also present at room temperature ambient [118]. Therefore, if remaining technical challenges (e.g. material with low defect density, temperature stable contacts, and reliable packaging technologies) can be overcome, GaN is likely to play a critical role in realizing high-power electronics beyond the capability of Si at all temperatures. For low-power circuits, GaN-based electronics will likely be relegated to the temperature range beyond the reach of silicon-on-insulator (SOI) electronics, which appears to be above 300°C [25]. High-voltage power rectifiers are key components of inverter modules, which are used in power flow control circuits. Lateral AlGaN-based Schottky rectifiers with spacings of 100 μm between the Schottky and ohmic metal contacts have shown reverse blocking voltages up to 9.7 kV. The figure of merit V^2_B / R_{on}, where V_B is the reverse breakdown voltage and R_{on} is the on-state resistance, was as high as 270 MW/cm^2 for these devices.

1.2.3 Costs and market

The allowable costs depend to a great extent on the application area. For commercial applications it is eminent that cost reduction is the driving force for any material system to survive. To service the wide range of applications discussed in Subsect. 1.2.2, GaN technology must be cost-competitive throughout the range of frequencies presently addressed by Si LDMOS, GaAs MESFET, and InP pHFET. To meet strict cost requirements the technology must be based on a large diameter, low cost substrate material such as Si or HVPE grown bulk GaN. Cost reduction on a system level is feasible because of GaN's high-temperature operation that eliminates the need of bulky cooling units. In addition, GaN devices do not require as much off-chip circuit protection as GaAs transistors hence elimination of these circuits leads to weight and cost savings. Furthermore, the ability of GaN transistors to produce higher power densities not only allows the use of smaller and fewer transistors in total but also the reduction or even elimination of costly linearization circuitry necessary for high-bandwidth wireless systems. It should be noted that these cost requirements stand in strong contrast with military applications which are mainly performance driven.

In 2004, the worldwide GaN device market, which was overwhelmingly dominated by LED sales, was worth $3.2 billion. For the year 2009, Strategies Unlimited estimates this value to be $7.2 billion. It is expected that optical applications will still dominate sales and account for 83% of this amount, leaving 17% to electronic applications such as microwave high-power amplifiers (HPAs) .

1.3 State-of-the-art for GaN-based microwave high-power applications

The state-of-the-art values for GaN-based HFETs in literature are very scattered as they depend heavily on substrate type, epitaxial material quality, device layout, and mode of operation i.e. continuous wave (CW) or pulsed. Therefore, we will specify these numbers for the most commonly used substrates for GaN heteroepitaxial growth: sapphire, semi-insulating (s.i.) SiC, and Si. In addition, we will briefly consider single-crystal AlN substrates and provide state-of- the-art values from literature for hybrid and monolithic integrated GaN-based microwave high-power amplifiers.

Sapphire substrate

Traditionally, sapphire is the most commonly used substrate for GaN heteroepitaxy. Sapphire is an interesting choice because it is semi-insulating, it can withstand the required high

growth temperatures, and it is relatively cheap ($ 100 for a 2 inch wafer). However, its very low thermal conductivity (0.47 W/cmK at 300 K), large lattice mismatch (13%), and large thermal expansion coefficient (TEC) mismatch (34%) with the GaN epilayers makes it the worst choice for high-power applications. Nevertheless, the power results for GaN HFETs on sapphire substrates are astonishing and are more than 10 times as high as can be achieved by GaAs HFETs. The state-of-the-art values for output power density of small gate periphery devices (typical total gate widths of 100 - 250 μm) with conventional T-shaped submicron gates are about 6.5 W/mm at 8 GHz and 3.3 W/mm at 18 GHz [25]. However, using a field-modulating plate (FP), which is an extension of the top of a conventional T-gate towards the drain contact, has overwhelmingly increased the power density of small devices to 12 W/mm at 4 GHz [26].

SiC substrate

The high thermal conductivity (3.7 - 4.5 W/cmK at 300 K), low lattice mismatch (3.4%), and relatively low TEC mismatch (25%) are the main reasons for the superior material quality of GaN epilayers grown on s.i. SiC compared to those grown on sapphire. As a consequence, the 2DEG transport properties of GaN epilayers on s.i. SiC are much better and it is very clear that at the moment s.i. SiC is the substrate of choice for GaN microwave high-power applications. For small periphery devices with conventional gates state-of-the-art values for output power density are 10 - 12 W/mm at X-band (8.0 - 12.4 GHz) [27, 28]. For small devices with a FP gate, record output power densities of over 30 W/mm at C- (4 GHz - 8 GHz) and X-band have been reported [29].

Si substrate

Despite the very large lattice mismatch (17%) and enormous TEC mismatch (56%), the advantages of low substrate cost, excellent availability of large substrate diameters, acceptable thermal conductivity (1.5 W/cmK at 300 K), and integration possibilities with Si electronics make Si substrates interesting candidates for GaN hetero-epitaxy. Although the epitaxial growth process of GaN on Si differs considerably from the ones on sapphire and s.i. SiC, the current state-of-the-art transistor results level those obtained on sapphire and even those on s.i. SiC. For small gate periphery devices with conventional gates the best reported output power densities are 12 W/mm at 2.14 GHz [30] and 7.0 W/mm at 10 GHz [31], respectively.

AlN substrate

Single-crystal aluminium nitride (AlN) substrates are possibly the best candidates for the heteroepitaxial growth of GaN epilayers because they have the same structure (wurtzite), high thermal conductivity (2.85 - 3.2 W/cmK at 300 K), high electrical resistivity (10^7 - 10^{13} Wcm) [32], and their lattice mismatch (2.4 %) and TEC mismatch (approximately 5.2 % from RT up to 1000°C) are very low. As a result of the last two properties, the defect density of GaN epilayers on AlN substrates is on the order of 10^3 - 10^4 cm^{-2} for 2 inch substrates [33], which is about four to five orders of magnitude lower than that of layers grown on 2 inch s.i. SiC substrates. It should be noted that the growth of high-quality large diameter bulk AlN substrates has proven to be very complicated. Only since early 2006, the US-based company Crystal IS has made 2 inch single-crystal AlN substrates available for the first time [33]. First AlGaN/GaN HFETs fabricated on small AlN substrates have shown DC current-voltage characteristics comparable to those fabricated on s.i. SiC [34].

Hybrid and monolithic integrated microwave high-power amplifiers

The majority of GaN-based high-power amplifiers that has been shown up to now is hybrid in nature. This means that the passive circuits needed for matching, biasing, and stabilization of the transistors are fabricated on a different substrate, which is connected to the active substrate by e.g. wire/ribbon bonding or flip-chip technology. It has to be noted that the GaN-based microwave monolithic integrated circuits (MMICs) are exclusively fabricated on SiC as substrate material. Table 1.2 provides a more detailed overview of reported state-of-the-art power results for small and large gate periphery GaN-based HFETs on sapphire, SiC, and Si substrates and for hybrid and monolithic integrated microwave power amplifiers.

Mat/Amp	f	$L_g \times W_g$	P_{out}	P_D	PAE	G_p	V_{DS}	mode	class	ref.
	(GHz)	(μm)	(W)	(W/mm)	(%)	(dB)	(V)			
sapphire	1.95	0.9 x 32,000	113	3.5	–	6.8	40	pulsed	–	[9]
sapphire	2.0	0.9 x 1,000	2.1	2.1	37.1	16.7	35	CW	–	[9]
sapphire	4.0	0.25 x 150 (FP)	1.8	12.0	58.0	15.0	26	CW	–	[30]
sapphire	8.0	0.15 x 100	0.65	6.5	47.0	15.0	26	CW	–	[161]
sapphire	18.0	0.15 x 100	0.33	3.3	–	–	26	CW	–	[161]
SiC	2.0	1.0 x 1,000	12.0	12.0	48.8	21.2	66	CW	–	[8]
SiC	2.0	0.5 x 4,000	28.4	7.1	76.0	16.1	48	CW	–	[132]
SiC	2.0	0.5 x 48,000	230.0	4.8	67.0	9.5	53	CW	–	[132]
SiC	3.5	0.4 x 250	3.0	12.0	34.0	16.0	90	pulsed	A	[140]
SiC	4.0	0.55 x 246 (FP)	7.9	32.2	54.8	–	120	CW	–	[174]
SiC	8.0	0.55 x 246 (FP)	7.5	30.6	49.6	–	120	CW	–	[174]
SiC	10.0	0.35 x 150 (FP)	2.5	16.5	47.0	16.0	60	CW	AB	[155]
SiC	10.0	0.25 x 1,500	13.8	9.2	33.0	10.0	55	pulsed	–	[179]
SiC	18.0	0.25 x 100	0.67	6.7	26.6	–	35	CW	–	[95]
SiC	26.0	0.25 x 200	1.0	5.0	30.1	5.24	25	CW	–	[102]
SiC	30.0	0.25 x 1,000	5.8	5.8	43.2	9.2	30	CW	–	[65]
SiC	35.0	0.25 x 200	0.83	4.13	23	7.54	30	CW	AB	[101]
Si	2.14	0.7 x 100	1.2	12.0	52.7	15.3	50	CW	AB	[73]
Si	2.14	0.5 x 36,000	55	1.53	–	13.4	28	CW	–	[24]
Si	4.0	0.5 x 100	0.18	1.8	32.0	16.0	30	CW	A	[161]
Si	10.0	0.3 x 200	1.4	7.0	52.0	12.0	40	CW	AB	[43]
Amp	2.0	0.4 x 24,000	102	4.25	54.0	8.0	37	CW	AB	[140]
Amp	10.0	0.4 x 12,000	38	3.2	29.0	8.0	37	CW	AB	[140]
Amp	16.0	0.4 x 6,000	24.2	4.0	22.0	12.8	31	pulsed	AB	[140]

Table 1.2: Detailed overview of reported state-of-the-art results for small and large gate periphery GaN-based HFETs on sapphire, SiC, and Si substrates and for hybrid and monolithic integrated microwave power amplifiers.

1.4 Objectives of this research

The research described in this thesis has been carried out within a joint ESA project (ATHENA). More in details our department has cooperated with the IMEC institute: based on the experimental results provided by IMEC, we first tried to reproduce the observed devices behaviour, which has been sometime unobvious and thus hint towards special properties of the GaN based devices. Then we have found some optimization rules to be applied to IMEC devices.

The work proceeded under two different impulses: from one side IMEC was proposing us the issues which were emerging during their process development, from another side we were proposing new design in order to solve specific issues observed either experimentally either in literature.

Our study was based on a solid theoretical background offered by the other group people activities which explained the most relevant properties of AlGaN/GaN hetero-structures,

mainly spontaneous and piezoelectric polarization. These background allowed the understand of the DC hemt properties that as we will see requires a correct position of the polarization fixed charges.

A further study was necessary in order to understand the time dependent behaviour of the GaN based devices. This study involved different bias conditions.

Once the most impacting issues affecting GaN based devices have been explained we tried to optimize the devices with a trough study involving the material properties, the hemt geometry design and conventional and non conventional field plates optimization. Another matter of study has been the design of GaN based schottky diodes: here too very interesting findings emerged.

1.5 References

[1] R. Juza and H. Hahn, "Über die kristallstrukturen von Cu3N, GaN und InN metallamide und metallnitride," Zeitschrift für anorganische und allgemeine Chemie, vol. 239, pp. 282–287, Oct. 1938.

[2] H. P. Maruska and J. J. Tietjen, "The preparation and properties of vapor-deposited single-crystalline GaN," Appl. Phys. Lett., vol. 15, pp. 327–329, Nov. 1969.

[3] W. Seifert, R. Franzheld, E. Butter, H. Subotta, and V. Riede, "On the origin of free carriers in high-conducting n-GaN," Crystal Res. and Technol., vol. 18, p. 383, 1983.

[4] J. I. Pankove, E. A. Miller, and J. E. Berkeyheiser, RCA Review, vol. 32, p. 383, 1971.

[5] H. P. Maruska, W. C. Rhines, and D. A. Stevenson, "Preparation of Mg-doped GaN diodes exhibiting violet electroluminescence," Mat. Res. Bull., vol. 7, pp. 777–781, Aug. 1972.

[6] H. Amano, M. Kito, K. Hiramatsu, and I. Akasaki, "p-type conduction in Mg-doped GaN treated with low-energy electron beam irradiation (LEEBI)," Jpn. J. Appl. Phys., vol. 28, pp. L2112–L2114, Dec. 1989.

[7] J. A. van Vechten, J. D. Zook, R. D. Horning, and G. Goldenberg, "Defeating compensation in wide gap semiconductors by growing in H that is removed by low temperature de-ionizing radiation," Jpn. J. Appl. Phys., vol. 31, pp. 3662–3663, 1992.

[8] I. Akasaki, H. Amano, M. Kito, and K. Hiramatsu, "Photoluminescence of Mg-doped p-type GaN and electroluminescence of GaN p-n junction LED," J. Lumin., vol. 48, pp. 666–670, 1991.

[9] S. Nakamura, T. Mukai, M. Senoh, and N. Iwasa, "Thermal annealing effects on p-type Mg-doped GaN films," Jpn. J. Appl. Phys., vol. 31, pp. L139–L142, Feb. 1992.

[10] H. Amano, N. Sawaki, I. Akasaki, and Y. Toyoda, "Metalorganic vapor phase epitaxial growth of a high quality GaN film using AlN buffer layer," Appl. Phys. Lett., vol. 48, pp. 353–355, Feb. 1986.

[11] S. Nakamura, "In situ monitoring of GaN growth using interference effects," Jpn. J. Appl. Phys., vol. 30, no. 8, pp. 1620–1627, Aug. 1991.

[12] M. Khan, J. Kuznia, A. Bhattarai, and D. Olson, "Metal semiconductor field effect transistor based on single crystal GaN," Appl. Phys. Lett., vol. 62, no. 15, pp. 1786–1787, 1993.

[13] M. Khan, J. van Hoven, J. Kuznia, and D. Olson, "High electron mobility GaN/AlGaN heterostructures grown by low-pressure metalorganic chemical vapor deposition," Appl. Phys. Lett., vol. 58, no. 21, pp. 2408–2410, 1991.

[14] M. Khan, J. N. Kuznia, D. T. Olson, W. Schaff, J. Burm, and M. Shur, "Microwave performance of a 0.25 μm gate AlGaN/GaN heterostructure field effect transistor," Appl. Phys. Lett., vol. 65, no. 9, pp. 1121–1123, 1994.

[15] S. Nakamura, M. Senoh, and T. Mukai, "p-GaN/n-InGaN/n-GaN double-heterostructure bluelight- emitting diodes," Jpn. J. Appl. Phys., vol. 32, pp. L8–L11, Jan. 1993.

[16] S. Nakamura, "Characteristics of room temperature CW operated InGaN multi-quantum-wellstructure laser diodes," in Proc. Mat. Res. Soc. Vol. 449. MRS, USA, Dec. 1996.

[17] R. T. Kemerley, H. B. Wallace, and M. N. Yoder, "Impact of wide bandgap microwave devices on DoD systems," Proceedings of the IEEE, vol. 90, pp. 1059–1064, June 2002.

[18] L. M. Tolbert, B. Ozpineci, S. K. Islam, and M. S. Chinthavali, "Wide bandgap semiconductors for utility applications," in Proc. Power and Energy Systems. ACTA Press, USA, Feb. 2003.

[19] R. J. Trew, "SiC and GaN transistors - Is there one winner for microwave power applications?" Proceedings of the IEEE, vol. 90, pp. 1032–1047, June 2002.

[20] E. O. Johnson, “Physical limitations on frequency and power parameters of transistors,” RCA Review, vol. 26, pp. 163–177, 1965.
[21] B. J. Baliga, “Semiconductors for high-voltage, vertical channel FET’s,” J. Appl. Phys., vol. 53, pp. 1759–1764, 1982.
[22] R. Borges, J. Brown, A. Hanson, S. Singhal, A. Vescan, and P. Williams, “GaN HFETs on silicon target wireless infrastructure market,” Compound Semiconductor, vol. 9, pp. 22–24, Aug. 2003.
[23] M. Kwasny and Z. Mierczyk, “Devices for medical diagnosis with GaN lasers,” in Laser Technology VII: Applications of Lasers. Edited by Wieslaw L. Wolinski and Zdzislaw Jankiewicz and Ryszard Romaniuk, vol. 5229, Oct. 2003, pp. 104–115.
[24] G. Meneghesso, A. Neviani, R. Oesterholt, M. Matloubian, T. Liu, J. J. Brown, C. Canali, and E. Zanoni, “On-state and off-state breakdown in GaInAs/InP composite-channel HEMT’s with variable GaInAs channel thickness,” IEEE Transactions on Electron Devices, vol. 46, no. 1, pp. 2–9, Jan. 1999.
[25] N. Vellas, C. Gaquière, A. Minko, V. Hoël, J. C. D. Jaeger, Y. Cordier, and F. Semond, “Power results at 4 GHz of AlGaN/GaN HEMTs on high resistivity silicon (111) substrate,” IEEE Microwave and Wireless Components Letters, vol. 13, no. 3, pp. 99–101, Mar. 2003.
[26] A. Chini, D. Buttari, R. Coffie, S. Heikman, S. Keller, and U. K. Mishra, “12 W/mm power density AlGaN-GaN HEMTs on sapphire substrate,” Electron. Lett., vol. 40, no. 1, pp. 73–74, Jan. 2004.
[27] V. Tilak, B. Green, V. Kaper, H. Kim, T. Prunty, J. Smart, J. Shealy, and L. Eastman, “Influence of barrier thickness on the high-power performance of AlGaN-GaN HEMTs,” IEEE Electron Device Letters, vol. 22, pp. 268–270, Nov. 2001.
[28] Y. F. Wu, D. Kapolnek, J. P. Ibbetson, P. Parikh, B. P. Keller, and U. K. Mishra, “Very-high power density AlGaN-GaN HEMTs,” IEEE Transactions on Electron Devices, vol. 48, pp. 586–590, Mar. 2001.
[29] Y. F. Wu, A. Saxler, M. Moore, R. P. Smith, S. Sheppard, P. M. Chavarkar, T. Wisleder, U. K. Mishra, and P. Parikh, “30-W/mm GaN HEMTs by field plate optimizaztion,” IEEE Electron Device Letters, vol. 25, no. 3, pp. 117–119, Mar. 2004.
[30] J. W. Johnson, E. L. Piner, A. Vescan, R. Therrien, P. Rajagopal, J. C. Roberts, J. D. Brown, S. Singhal, and K. J. Linthicum, “12 W/mm AlGaN-GaN HFETs on silicon substrates,” IEEE Electron Device Letters, vol. 25, no. 7, pp. 459–461, July 2004.
[31] D. C. Dumka, C. Lee, H. Q. Tserng, P. Saunier, and M. Kumar, “AlGaN/GaN HEMTs on Si substrate with 7W/mm output power density at 10 GHz,” Electron. Lett., vol. 40, no. 16, Aug. 2004.
[32] L. Liu and J. H. Edgar, “Substrates for gallium nitride epitaxy,” Materials Science and Engineering R, vol. 37, pp. 61–127, 2002.
[33] --“LED breakthrough highlights AlN promise,” Compound Semiconductor, vol. 12, no. 5, pp. 31–32, June 2006.
[34] X. Hu, J. Deng, N. Pala, R. Gaska, M. S. Shur, C. Q. Chen, J. Yang, G. Simin, M. A. Khan, J. C. Rojo, and L. J. Schowalter, “AlGaN/GaN heterostructure field-effect transistors on single-crystal bulk AlN,” Appl. Phys. Lett., vol. 82, no. 8, pp. 1299–1301, Feb. 2003.

Chapter 2

Physical modeling of GaN transistors and Schottky diodes

2.1 Introduction

Depending on the device under investigation and the level of modelling accuracy required, we can select within four different simulation modes:

1. **Drift-diffusion**: Isothermal simulation, described by basic semiconductor equations. Suitable for low-power density devices with long active regions.
2. **Thermodynamic**: Accounts for self-heating. Suitable for devices with low thermal exchange, particularly, high-power density devices with long active regions.
3. **Hydrodynamic**: Accounts for energy transport of the carriers. Suitable for devices with small active regions.
4. **Monte Carlo**: Allows for full band Monte Carlo device simulation.

The Monte Carlo code is presented in section 2. The equations for the drift-diffusion, is presented in sections 3 and 4. Advanced models such as thermodynamic, hydrodynamic etc are discussed in section 5. A simplified quasi 2D model is presented in Section 6. Finally, in section 8 we present the theory for strain calculation in SiN/AlGaN/GaN structures.

2.2 Monte-Carlo simulations

Our model is a two-dimensional self-consistent Monte-Carlo code which accounts for four conduction valleys and three valence bands [1](fig 2.1). Poisson equation is solved by applying a multigrid technique [2]. Impact ionization, which can be described by a modified Kane model [3], has not be implemented in the following simulations.

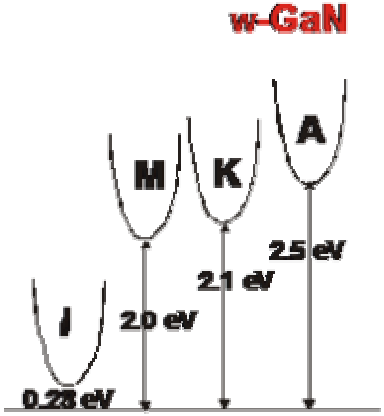

Fig. 2.1: Conduction Band structure used for GaN Monte Carlo simulations.

In our model the parameters for the valleys are estimated from band structure calculations [4,5]. Phonon scattering (acoustic, optical, and polar optical modes), and ionized impurity scattering were accounted for. The parameters assumed for GaN and Al_xGaN, shown in table I, have been

taken from Refs. [4-7]. The ionized impurity scattering was taken into account according to Brooks-Herring formula. The alloy scattering was neglected, since inclusion of this process causes small changes in velocity-field characteristics for III-V alloys [8].
Optimized parameters for GaN and AlGaN used in the Monte Carlo Simulator have been summarized in Table 2.1.

Table 2.1: Parameters of wurtzite GaN, and AlGaN

Parameters	Symbols	h-GaN (bulk)	h-AlN (bulk)	h-$Al_xGa_{1-x}N$
Lattice constant	a(Å) c(Å)	3.189 5.185	3.10 4.98	3.189-0.089x 0.4272x+0.222 x^2
Density	$\rho\left(Kg/m^3\right)$	6.15	3.23	6.15-2.92x
Sound Velocity	$S_v\left(m/s\right)$	4330	4330	4330
Dielectric constants	ε_0 ε	10 5.5	8.5 4.68	10-1.5x 5.5-0.82x
Piezoelectric constants	$C_p\left(Cb/m^2\right)$	0.56	0.56	0.56
Binding potential	$P_1\left(eV\right)$	0	0	0.42
Bottom valley energy	$\varepsilon_\Gamma\left(eV\right)$ $\varepsilon_M\left(eV\right)$ $\varepsilon_K\left(eV\right)$ $\varepsilon_A\left(eV\right)$	3.5 5.4 5.5 6.0	6.20 6.7 6.9 8.3	3.5+2.65x+0.05 x^2 5.4+1.3x 5.5+1.4x 6.0+2.3x
Effective masses near the valley minimum	$m_\Gamma\left(m_0\right)$ $m_M\left(m_0\right)$ $m_K\left(m_0\right)$ $m_A\left(m_0\right)$	0.21 0.30 0.36 0.27	0.29 0.40 0.42 0.33	0.21+0.08x 0.3+0.1x 0.36+0.06x 0.27+0.06x
Non-parabolicity coefficient	$\alpha_\Gamma\left(eV\right)$ $\alpha_M\left(eV\right)$ $\alpha_K\left(eV\right)$ $\alpha_A\left(eV\right)$	$\sim\left(1-m_\Gamma^*\right)^2/\varepsilon_\Gamma$ 0.029 0.065 0.01	$\sim\left(1-m_\Gamma^*\right)^2/\varepsilon_\Gamma$ 0.029 0.065 0.01	$\sim\left(1-m_\Gamma^*\right)^2/\varepsilon_\Gamma$ 0.029 0.065 0.01
Polar Optical phonon Energy	$\hbar\omega_{LO}\left(eV\right)$	0.092	0.113	0.092-0.113x
Intervalley phonon energy	$\hbar\omega_{i,j}\left(eV\right)$	$0.8\times\hbar\omega_{LO}$	$0.8\times\hbar\omega_{LO}$	$0.8\times\hbar\omega_{LO}$
Acoustic deformation potential	$\Phi a_\Gamma\left(eV\right)$ $\Phi a_M\left(eV\right)$ $\Phi a_K\left(eV\right)$ $\Phi a_A\left(eV\right)$	10.1 10.1 10.1 10.1	10.1 10.1 10.1 10.1	10.1 10.1 10.1 10.1
Polar optical deformation potential	$\Phi_{NPO}\left(eV/m\right)$	9.0×10^{10}	9.0×10^{10}	9.0×10^{10}
Inervalley deformation potential	$\Phi_{i,j}\left(eV/m\right)$	10^{11}	10^{11}	10^{11}
Band offset with respect to h-GaN	$\Delta Ec\left(eV\right)$ $\Delta Ev\left(eV\right)$	0.0 0.0	2.0 0.8	$\Delta Ec/\Delta Ev$ $=62/38$

2.2.1 Bulk MC Simulations

In order to verify the correctness of our Monte Carlo simulation and the parameter used in the code, we have performed a series of MC simulations of carrier transport in wurtzite GaN. In particular, we have calculated the velocity-field characteristics and compared with published results obtained via Full-Band Monte Carlo approaches. Result of the simulations are shown in Fig.2. 2 considering a non intentional doping of 10^{17} cm^{-3}

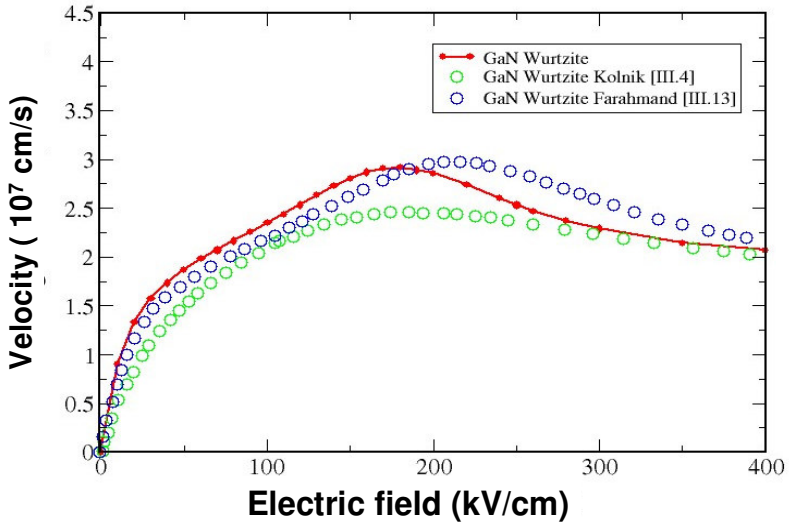

Fig. 2.2 Comparison between MC simulation of velocity-field characteristics obtained in the present work with those obtained by other groups

The steady-state peak velocity is $2.3x10^7$ cm/s. The saturation velocity $2.0x10^7$ cm/s is approximatively three times as high as GaAs (6.0^x10^6 cm/s at 300 kV/cm) [9] and a region of negative differential resistance is observed. Satisfactory agreement was obtained between the present and previous theoretical findings [4,10]. These results show the accuracy of our model.

2.2.2 Comparison with Full-band MC Simulations

In order to check the correctness of our MC device simulations, we have compared the result of our MC with those of Ando and coworkers (IEEE TED 47, 1965, (2000)) obtained with Full-Band MC simulations. The result of the comparison is shown in Fig. 2.3

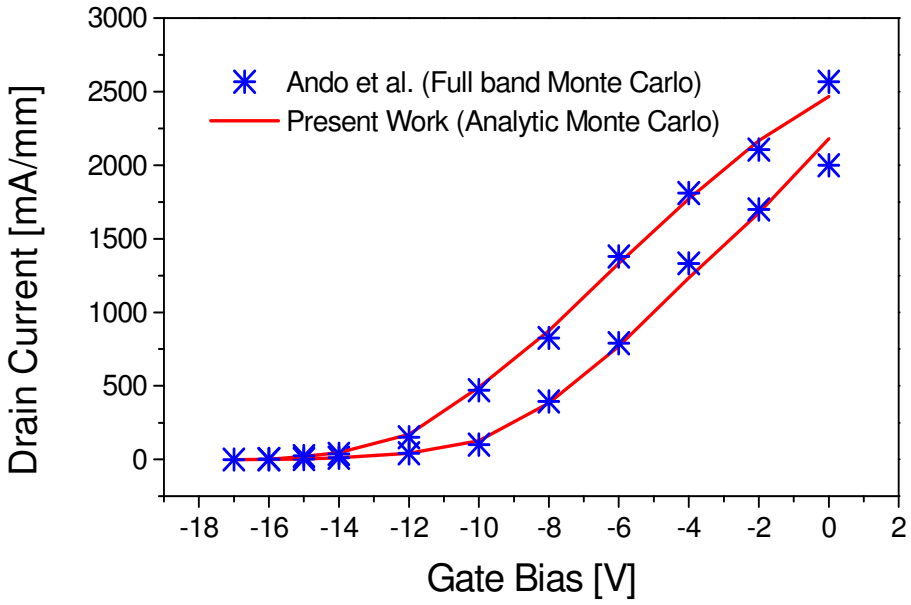

Fig. 2.3 Comparison between our MC approach and the Full- band MC results of Ando and coworkers.

The agreement between the two models is quite remarkable and underline the quality of our MC simulator.

2.3 Drift-Diffusion (DD) simulations

The Drift-Diffusion (DD) code used here is a DESSIS-ISE release **9.1** [11]. The transport equation considered in this model are the following

$$J_n = qn\mu_n F + qD_n \nabla n$$
$$J_p = qp\mu_p F - qD_p \nabla p$$
$$\frac{\partial n}{\partial t} = \frac{1}{q}\nabla \cdot J_n + G - R$$
$$\frac{\partial p}{\partial t} = -\frac{1}{q}\nabla \cdot J_p + G - R$$
$$\nabla \cdot (\varepsilon_0 \varepsilon_r \nabla V) = -q(p - n + N_D - N_A)$$

where μ is the mobility, D is the diffusion coefficient, n and p are the charge densities for electron and holes, respectively, and $G(R)$ is the generation (recombination) term.
This version of the DESSIS has no built-in GaN parameters for device simulations. We have obtained these parameters from the Table 2.2.1 and from other literature data. However, a critical point is the determination of the relation between mobility and electric field. In order to determine a mobility field relation which can produce reliable device characteristics, we have compared Monte Carlo simulations for GaN based MESFET device with those obtained with DD simulator. We have considered a functional for of the mobility of the form

$$v(E) = \mu_0 E \left[1 + \left(\frac{\mu_0 E}{v_{sat}} \right)^{\beta} \right]^{-1/\beta}$$

Where μ_o, β and v_{sat} are parameters to be identified via MC-DD comparison.

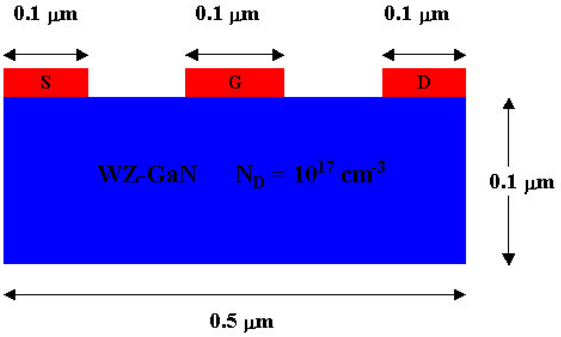

The device considered for the determination of the mobility for the DD simulator is the one shown in figure 2.4. We have chosen to simulate MESFET because we do not have to include polarization at the interface between AlGaN and GaN (see discussion below).
The output characteristics obtained with MC and with DD are shown in Fig. 2.5. A remarkable good agreement between the two simulation is found

Fig. 2.4 Simulated device for MC-DD comparison

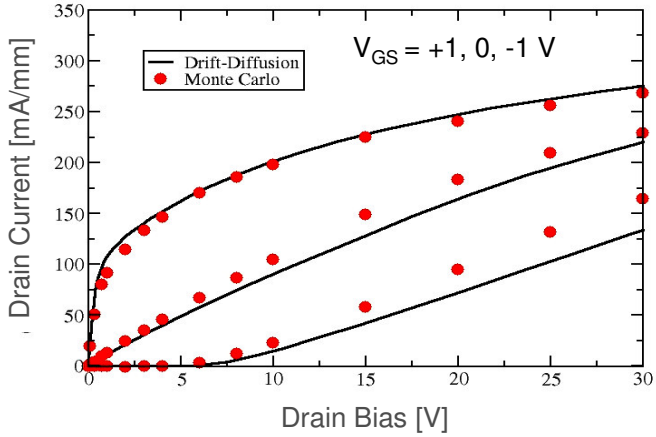

Fig. 2.5 Comparison between MC and DD simulation of the MESFET structure

In order to have the shown agreement between DD and MC we have chosen the following parameters for the DD simulations:

Parameter	Value
Density of states N_c	$2.4\times10^{18}\ cm^{-3}$
Electron affinity	4.1 eV
Donor Ionization energy (Si) $E_t - E_c$	0.022 eV
Low field mobility μ_0	$850\ cm^2/V\cdot s$
Saturation velocità v_{sat}	$1.9\times10^7\ cm/s$
Exponent, β	2
Schottky Barrier Metal-GaN	1.2 eV

Such parameters produce the velocity-field characteristics shown in fig. 2.6

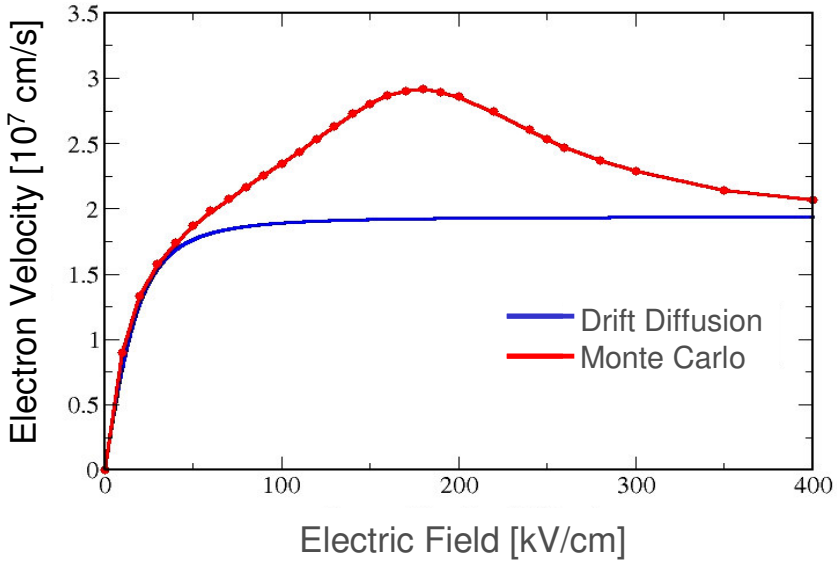

Fig. 2.6 Velocity-Field characteristics of GaN as obtained with MC and DD

We see, from Fig. 2.7 that, in order to reproduce MC output characteristics of the MESFET structure, the DD should only consider the low field mobility and the saturation velocity regions while should neglect the negative mobility region. Drift-Diffusion simulations with mobility model accounting also the negative mobility region, do not reproduce MC results for device simulations. Such effect is well known for GaAs mobility model where negative differential mobility in never considered in Drift-Diffusion simulations of real devices. We should also point out that electron mobility will also depend of the quality of the epilayer. In several simulations, for the most recent devices of IMEC, mobility of the quantized AlGaN/GaN 2DEG has been improved and we have used a value of 1700 cm^2/Vs for the DD simulations.

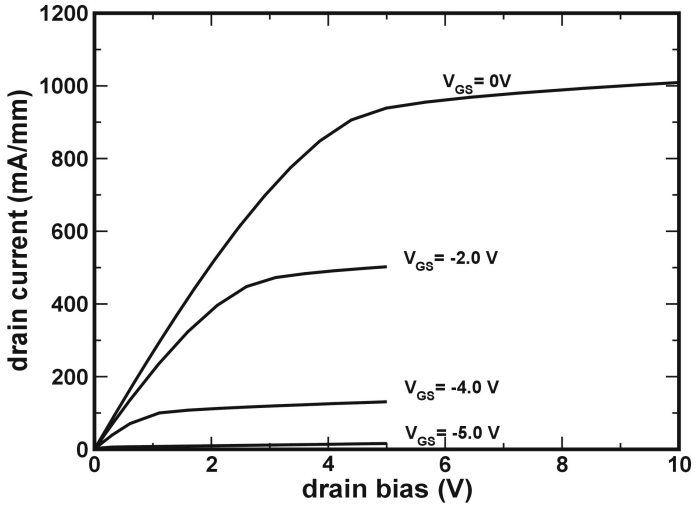

Fig. 2.7 Output characteristics of the symmetric GaN HEMT as obtained with Drift-Diffusion simulations.

After this preliminary phase of calibration, we have consider DD simulations of GaN based HEMTs. We have considered the polarization charges as a thin δ-doping layer at the AlGaN/GaN interface. A δ-doping (1 nm) of (10^{20} cm^{-3}) is needed in order to induce a 2D electron gas density of 10^{13} cm^{-2} at the AlGaN/GaN interface. Fig. 2.8 shows the output characteristics obtained with the DD simulations for a typical GaN/AlGAN HENTS. Comparison with MC results is shown in Fig. 2.3.5

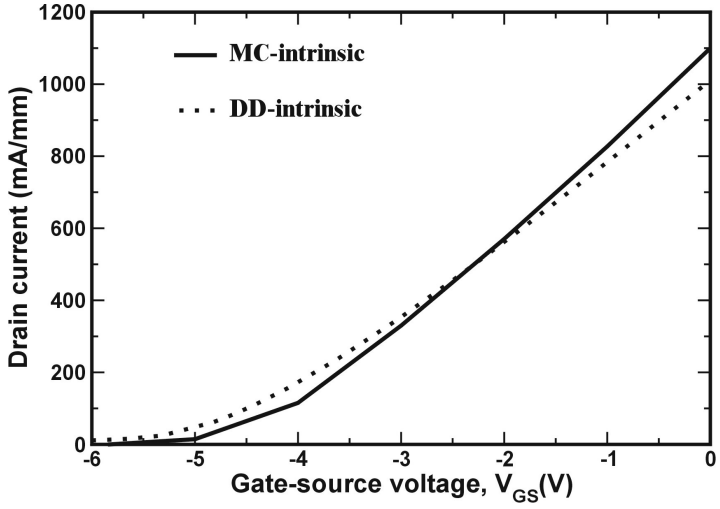

Fig. 2.8: Static transfer characteristics I_{DS}-V_{GS} of AlGaN/GaN HFETs obtained at V_{DS}=10V. Results obtained by both methods are very close. The drain current obtained here is for intrinsic device (.i.e the contact resistance has been excluded from calculations).

In conclusion, we have developed consistent Drift-Diffusion simulations of electron transport for AlGaN/GaN HEMTs . DD simulations have been tuned in order to reproduce Monte Carlo results.

2.4 Time dependent simulations

2.4.1 Transient Simulations

The Current Collapse induces a strong RF Drain current dispersion and is one of the most limiting factors in the development of AlGaN/GaN HEMTs: various hypotheses have been done to explain such effect. As a matter of fact, its entity is strictly connected with surface states present at the interface between AlGaN and air, and it is reduced by surface passivation [1] or by adding p^+ and n^+ doped layer at the access region [2].

An high density of surface states between the gate and source/drain contacts will act as virtual gates, modulating the depletion region, through changes in the trapped charge density. These virtual gates respond to a gate voltage pulse with times characteristic of carrier capture/emission phenomena, thus leading to a delay in I_D switching and to RF collapse.

There are two main models which have been suggested to explain these phenomena: the “electron” model [3] and the recent “hole” model [4] (see Fig. 2.9 and 2.10 for details)

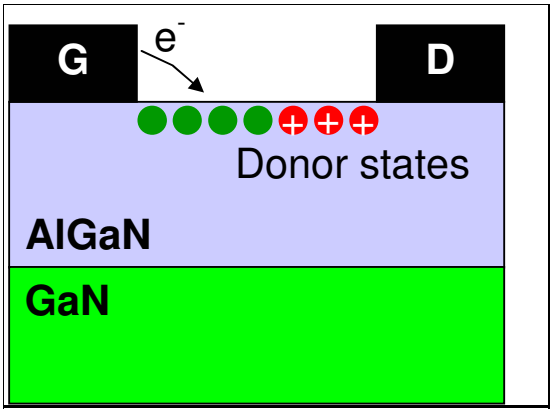

Fig. 2.9 "electron" model for current collapse.

For large –VGS donor states are filled with electrons and σ_{top} is negative and large (low current). When VGS becomes smaller electrons are detrapped with a given time constant

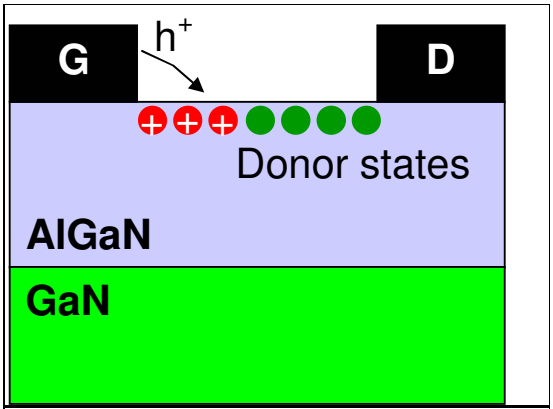

Fig. 2.10 "hole" model for current collapse.

For large –VGS donor states are filled (neutral) and σ_{top} is negative and large (low current). When V_{GS}

becomes smaller, holes flow from the gate into the surface accumulation layer and trapping mechanism will take place.

In order to investigate current collapse induced by surface traps we have performed a two-dimensional time-dependent drift diffusion simulation of the device of Fig.2.4.2 using the DESSIS tool. In this investigation we have considered the more recent "hole" model [4] which supposes donor-like traps in the Air/AlGaN interface. Traps are charged in a characteristic time by holes so to balance the negative surface charge and to determine a higher level of current. The holes are supplied by the gate contact and, according to this model, the traps charging efficiency strictly depends on their energy level. To perform these simulation we have extended the drift diffusion model by adding a time dependent charging of surface traps.
In the transient case, the differential equations for the electron-related occupation probability at each energy level are:

$$\frac{df_n}{dt} + \left[v_{\mathrm{th}}^n \sigma_n \left(n + \frac{n_1}{g_n} \right) + v_{\mathrm{th}}^p \sigma_p \left(p + \frac{p_1}{g_p} \right) \right] f_n = v_{\mathrm{th}}^n \sigma_n n + v_{\mathrm{th}}^p \sigma_p \frac{p_1}{g_p}$$

with the usual meaning for the parameters.[11] These equations are solved self-consistently with the transport and Poisson equations. In the transient case, the recombination processes for electrons and holes are different, and the SRH form cannot be applied. For one level, this becomes:

$$R_{\mathrm{Et}}^n = v_{\mathrm{th}}^n \sigma_n N_{\mathrm{Et}} \left[n(1-f_n) - \frac{n_1}{g_n} f_n \right]$$

$$R_{\mathrm{Et}}^p = v_{\mathrm{th}}^p \sigma_p N_{\mathrm{Et}} \left[p f_n - \frac{p_1}{g_p} (1-f_n) \right]$$

with

$$p_1 = n_{\mathrm{i,eff}} \exp(-E_t / k_B T)$$

Here, E_t is a trap energy, N_{Et} the trap density p/*n* is the free hole/electron concentrations, v_{th} is the thermal velocity, σ is the capture cross section, f_n the electron distribution (f_p=*1*-f_n), *g* the trap degeneration, and *T* is the lattice temperature.
The total recombination terms for the electron and hole continuity equations are also equal to the sum for all levels as in the steady state case.

2.4.2 Model for reliability study

A necessary part of reliability prediction is the simulation of the time dependence of interface trap generation. To cover as wide a range as possible, this simulation should accurately reflect the physics of the interface trap formation process. The passivated AlGaN-SiO_2 (or AlGaN-SiN) interface have been shown to be a plausible placement of the trap generation process. Up to now the model suppose hot electrons to cross the hetero-barrier reaching high energy traps at the surface. Hence the trapped electrons reduce the 2-DEG density providing a fixed negative charge at the interface. Such model is compatible with a first order kinetic low, that is experimentally observed. In addition, the field dependence of the activation energy (Poole–Frenkel effect) is included, so that all these factors lead to an enhanced trap formation kinetics.
The trap formation low can be represented by different kinetic laws. However we chose the following one:

$$\frac{dn}{dt} = -kn + \gamma(N - n)$$

where *N-n* is the concentration of generated traps, while *k* has a energy dependence expressed by Arrhenius law:

$$k = k_0 \exp\left[-\frac{\varepsilon_A}{kT}\right]$$

where ε_A is the trap formation energy, T is the electrons temperature.
To include the effect of the electric field on the trap creation-occupation dynamics we included in our physical model the Poole-Frenkel effect.
More in detail, applying an high electric field, *F*, the trap walls result lowered due to the band bending induced by the potential slope. Such lowering can be evaluated by a factor $\beta\sqrt{F}$ on the electric field direction where $\beta = q^{3/2} / \sqrt{\pi\varepsilon\varepsilon_0}$ is the Frenkel-Poole constant.
According to this model the equations previously written become:

$$k = k_0 \exp\left(\frac{\Delta\varepsilon_A}{\varepsilon_T}\right)\exp\left(\frac{\varepsilon_A}{k_B T_0} - \frac{\varepsilon_A}{\varepsilon_T}\right) k_{FN} k_{HC}$$

$$\varepsilon_T = k_B T + \delta_{//} F_{//}^{\rho_{//}}$$

$$k_{HC} = 1 + \delta_{HC} I_{HC}^{\rho_{HC}}$$

$$k_{FN} = 1 + \delta_{Tun} I_{Tun}^{\rho_{Tun}}$$

$$\Delta\varepsilon_A = \delta_\perp F_\perp^{\rho_\perp} + (1+\beta)\varepsilon_T \ln\frac{N-n}{N-n_0}$$

$$\beta = \beta_0 + \beta_{//} F_{//} + \beta_\perp F_\perp$$

where $F_{//}$ and $F_\perp$ are the components of the electric field at the trap site, while I_{HC} and I_{Tun} are the local current densities due to hot electrons and tunnelling effects. ε_T is the energy of saturated bounds at the $Si_3N_4 / AlGaN$ interface; $\Delta\varepsilon_A$ is the activation energy variation induced by the electric field presence, while δ_0, ρ_0, $\delta_{//}$, $\rho_\perp$, δ_{HC}, ρ_{HC}, δ_{Tun}, ρ_{Tun}, β_0, $\beta_{//}$ and $\beta_\perp$ are the coefficients used to express the current variation as a function of the electric field. [11]

2.5 Additional advanced models

2.5.1 Thermodynamic model

The heat generation in the channel is caused by an energy transfer from the electron to the lattice, which is related to inelastic phonon scattering processes of the electron. For this reason it is necessary to include a thermodynamic (or nonisothermal) model in order to extends the drift-diffusion approach. In the following simulations we made the assumption that the charge carriers are in thermal equilibrium with the lattice. Therefore, the carrier temperatures and the lattice temperature are described by a single temperature. The thermodynamic model is defined by the basic set of partial differential equations and the lattice heat flow equation. The drift diffusion equations relations are generalized to include the temperature gradient as a driving term:

$$J_n = -nq\mu_n\left(\nabla\varphi_n + P_n\nabla T\right)$$
$$J_n = pq\mu_p\left(\nabla\varphi_p - P_p\nabla T\right)$$

Where P_n and P_p are the absolute thermoelectric powers.
To calculate the temperature distribution in the device due to self-heating, the following equation is solved:

$$c\frac{\partial T}{\partial t} - \nabla\cdot\kappa\nabla T = -\nabla\cdot[(P_nT+\phi_n)\vec{J_n} + (P_pT+\phi_p)\vec{J_p}] - \left(E_C + \frac{3}{2}k_BT\right)\nabla\cdot\vec{J_n} - \left(E_V - \frac{3}{2}k_BT\right)\nabla\cdot\vec{J_p} + qR(E_C - E_V + 3k_BT)$$

where κ is the thermal conductivity and c is the lattice heat capacity. E_C and E_V are the conduction and valence band energies, respectively, and R is the recombination rate.
In our simulations k=1.3 W cm^{-1}K^{-1} and c=3.0 J cm^{-3}K^{-1}.
In the heat flow calculation, the top of the device is assumed to face an air with thermal resistance (RP) of 4.3×10^{-2} m^{2}K/W. The bottom of the device are assumed to face the substrate (i.e., sapphire, SiC and Si). The corresponding RP are 6.0×10^{-7} m^{2}K/W for sapphire, 0.89×10^{-7} m^{2}K/W for SiC and 1.8×10^{-7} m^{2}K/W for Si, respectively, which are determined on the assumption that the thickness of the substrate is 300 μm. For the back contact a 0 thermal resistance is assumed. The substrate is assumed on a heat sink, whose temperature is 300 K. The temperature dependencies of the thermal conductivities of the substrate and the constituent materials of the device are not taken into account.

2.5.2 Hydrodynamic model

With continued scaling into the deep submicron regime, neither internal nor external characteristics of state-of-the-art semiconductor devices can be described properly using the conventional drift-diffusion transport model. In particular, the drift-diffusion approach cannot reproduce velocity overshoot and often overestimates the impact ionization generation rates. The Monte Carlo method for the solution of the Boltzmann kinetic equation is the most general approach, but because of its high computational requirements, it cannot be used for the routine simulation of devices in an industrial setting.
In this case, the hydrodynamic (or energy balance) model provides a very good compromise. Since the work of Stratton and Bløtekjær, there have been many variations of this model. The full formulation, including the so-called convective terms, consists of eight partial differential equations (PDEs) , while the simpler form (no convective terms) includes six PDEs. The transport model implemented in DESSIS [11] is based on the approach involving the solution of six PDEs. In the hydrodynamic model, the carrier temperatures and are assumed to not equal the lattice temperature. Together with basic semiconductor equations, up to three additional equations can be solved to find the temperatures. In general, the model consists of the basic set of PDEs (the Poisson equation and continuity equations) and the energy conservation equations for electrons, holes, and the lattice.
In the hydrodynamic case, current densities are defined as:

$$J_n = q\mu_n\left(n\nabla E_C + k_BT_n\nabla n + f_n^{td}k_Bn\nabla T_n - 1.5k_BnT_n\nabla\ln m_e\right) \quad \text{[Eq. 5.1]}$$
$$J_p = q\mu_p\left(p\nabla E_V + k_BT_p\nabla p + f_p^{td}k_Bp\nabla T_p - 1.5k_BpT_p\nabla\ln m_h\right) \quad \text{[Eq. 5.2]}$$

where E_C and E_V are the conduction and valence band energies, respectively. The first term takes into account the contribution due to the spatial variations of electrostatic potential, electron affinity, and the band

gap. The three remaining terms in [Eq. 5.1] and [Eq. 5.2] take into account the contribution due to the gradient of concentration, the carrier temperature gradients, and the spatial variation of the effective masses m_e and m_h.

The energy balance equations read:

$$\frac{\partial W_n}{\partial t} + \nabla \cdot \vec{S}_n = \vec{J}_n \cdot \nabla E_C + \frac{dW_n}{dt}\Big|_{coll}$$

$$\frac{\partial W_p}{\partial t} + \nabla \cdot \vec{S}_p = \vec{J}_p \cdot \nabla E_V + \frac{dW_p}{dt}\Big|_{coll}$$

$$\frac{\partial W_L}{\partial t} + \nabla \cdot \vec{S}_L = \frac{dW_L}{dt}\Big|_{coll}$$

where the energy fluxes are:

$$\vec{S}_n = -\frac{5r_n}{2}\left(\frac{K_B T_n}{q}\vec{J}_n + f_n^{hf}\hat{k}_n \nabla T_n\right)$$

$$\vec{S}_p = -\frac{5r_p}{2}\left(\frac{K_B T_p}{q}\vec{J}_p + f_p^{hf}\hat{k}_p \nabla T_p\right)$$

$$\vec{S}_L = -k_L \nabla T_L$$

$$\hat{k}_n = \frac{k_B^2 T_n n \mu_n}{q}$$

$$\hat{k}_p = \frac{k_B^2 T_p p \mu_p}{q}$$

Different values of the r_n, r_p, f_n^{td}, f_p^{td}, f_n^{hf} and f_p^{td} parameters can significantly influence the physical results, such as velocity distribution and possible spurious velocity peaks. By changing these parameters, DESSIS can be tuned to a very wide set of hydrodynamic/energy balance models as described in the literature. The default parameter values are:

$r_n = r_p = 0.6$

$f_n^{td} = f_p^{td} = 0$

$f_n^{hf} = f_p^{td} = 1$

The default constants were obtained for $\nu = -1$, which means that the carrier mobility is inversely proportional to the carrier temperature.

2.5.3. Impact Ionization

Impact ionization and avalanche generation effects are fundamental in a framework where the power applications play a dominant role.

The characterization of avalanche generation in GaN have been performed by means of the ISE-TCAD DESSIS simulator; hydrodynamic features have been included, such as an electron temperature different from bulk temperature.

Impact ionization has been studied according to the Van Overstraeten – de Man model. This model is based on the Chynoweth law [12], according to which the impact ionization generation rate for electrons is defined by the following law:

$$G = \alpha n v_{drift} \;;$$

where n is electron concentration, v_{drift} is drift velocity of electrons, and α is a field and temperature dependent parameter. The expression used for α_{low} ($E<E_0$) and for α_{high}, as well as the fitted parameters for electrons, are shown below.

$$\alpha(E) = a\gamma \exp\left(\frac{-b\gamma}{E}\right), \qquad \text{[Eq. 5.3]}$$

where

$$\gamma = \frac{\tanh(\omega/2kT_0)}{\tanh(\omega/2kT)}$$

and the parameters used for GaN are

a(low) = 2.0x10^6 [cm^{-1}]
a(high) = 1.0 x10^5 [cm^{-1}]
b(low) = 3.0 x10^7 [V/cm]
b(high) = 2.2 x10^7 [V/cm]
E_0 = 3.2 x10^6 [V/cm]
ω = 0.035 [eV]
T_0 =300 [K]

The impact ionization rate obtained with these values of the parameters is shown in Fig. 2.11, while in Fig. 2.12 we show a comparison with Monte-Carlo calculations taken from Ref [13]. Our results are also in good agreement with other theoretical and experimental findings [14,15]. The same expression (Eq. 5.1) has been used for holes; in this case, as for now, only one parameterization has been used: a = 1.0 x10^5 [cm^{-1}]; b = 2.0 x10^7 [V/cm]

The fitted parameters have been then used for simulation of GaN HEMTs and Schottky diodes.

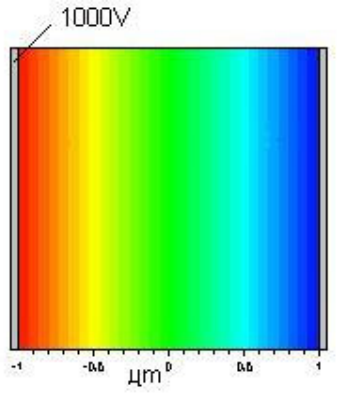

Fig. 2.11: Impact ionization rate obtained applying a 1000V voltage drop to a 2μm sample of GaN. The colours indicate a logarithmic drop from 75000 to 68000 cm^{-1}.

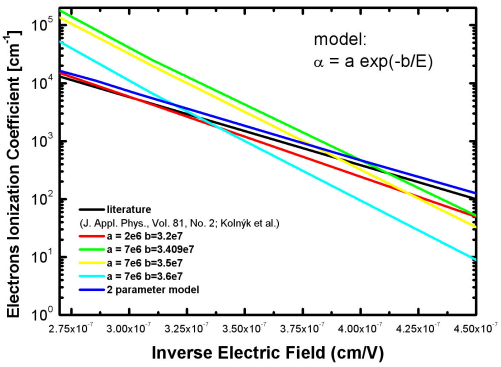

Fig. 2.12: Impact ionization rate fitting. The blue line result is found with a different parameterization for high and low field.

2.6 Self-Consistent Schroedinger-Poisson equation and quasi 2D model

2.6.1 Schroedinger-Poisson solver

In order to study the mechanisms of channel formation and of current flow in GaN based MODFET, Schrödinger's equation can be used self-consistently coupled with Poisson equation.
Within the effective mass theory, Schroedinger's equation takes the form

$$-\frac{\hbar^2}{2}\frac{d}{dz}\left(\frac{1}{m(z)}\frac{d}{dz}\right)\varphi + \left(eV(z) + \Delta E(z)\right)\varphi = E\varphi \qquad \text{[Eq. 6.1]}$$

where m(z) is the position dependent effective mass, V(x) the electrostatic potential, ΔE the band discontinuity, φ the electron wavefunction and E the electron energy. Non-parabolicity may induce deviations from the simple parabolic band model, however this will not substantially change the results.
In the nitride semiconductors grown in the wurtzite structure, the presence of spontaneous and piezoelectric polarization effects implies that Poisson equation has to be solved for the displacement field, D(z)

$$\frac{d}{dz}D(z)=\frac{d}{dz}\left(-\varepsilon(z)\frac{d}{dz}V(z)+P(z)\right)=e\left(p(z)-n(z)+N_D^+-N_A^-\right) \qquad \text{[Eq. 6.2]}$$

where ε(z) is the position-dependent dielectric constant, P the total polarization, n(p) the electron(holes) charge concentration and $N_D^+(N_A^-)$ the ionized donor(acceptor) density. The total polarization charge can be written as $P_{tot}= P_{piezo}+P_{spont}$, where P_{piezo} is the piezoelectric charge
whereas P_{spont} represents the spontaneous polarization of the GaN/AlGaN interface. The piezoelectric charge induced by the lattice in-plane mismatch ($\sigma_{\|}$) can be calculated as

$P_{lm} = -2 \left(e_{33}\frac{C_{11}}{C_{33}}-e_{31}\right)\sigma_{\|}$, where e_{ij} and C_{ij} are the piezoelectric tensor components and the elastic constants, respectively [16]. Since the layers are grown on thick GaN buffer layers, we expect that the GaN layers are relaxed and take the bulk GaN lattice constant of the buffer (3.189 A).
Moreover, we assume that the AlGaN layers grow pseudomorphically in our structures and undergo a tensile in-plane strain $\sigma_{\|}$. As far as the spontaneous polarization charge is concerned, we take the values of P_{sp}= -0.034 C/m^2 for the GaN and P^b_{sp}= -0.09 C/m^2, for the AlN [17]. The spontaneous polarization for the AlGaN alloy has been obtained by a non linear interpolation of the binary compound values, according to the law: $P_{sp}(x) = x\,P_{sp}(AlN) + (1-x)\,P_{sp}(GaN) - bx(1-x)$, where the bowing parameter is b = -0.021 .
A self-consistent procedure has been set up, where the potential V is obtained using Eq. 6.2 from an initial guess of the mobile charge concentration, and then inserted into the Schrödinger's equation, (Eq. 6.1)) which is solved to obtain the energy levels and wavefunctions of the system. The new electron charge density, calculated by applying Fermi statistics, is then plugged into Poisson equation (Eq. 6.2)) and the iteration repeated until convergence is achieved.

The calculations have been performed by considering only the polarization charge at the AlGaN/GaN interface. In principle, polarization charges that form at the metal-AlGaN and at the end of the GaN buffer region should be also accounted for. However, the metal-AlGaN charge is completely screened by the charges induced on the metal surface and can therefore be neglected. On the other hand, the charges at the end of the buffer region may have a strong effect. The exact amount of such charge depends, however, on the morphology of the heterojunction. The situation is less critical if the bottom interface is far away from the main AlGaN/GaN heterojunction. In this case, the polarization charge that arises can be completely screened by the residual doping of the GaN substrate. On the contrary, if such interface is close to the AlGaN/GaN heterojunction, the polarization charge can completely deplete the channel.
In our simulations we have considered a thick GaN substrate. Thus, the effect of the polarization charge at the end of the GaN substrate can be considered completely screened.

2.6.2 Quasi - 2D Model for calculation of current

We have implemented a quasi-2D model for the calculation of the current-voltage characteristics of the nitride FETs. The quasi two-dimensional models are in general based on a solution of the Poisson and current equations using a two-dimensional description of the active channel and on the assumption that the electric field E = E(x) is one-dimensional in the channel (see fig. 2.13). These assumptions are verified by reference to the results from full two-dimensional models, and allow a considerable reduction of the scale of computational burden.
Our quasi 2D model makes use of the exact value of the sheet charge density in a HFET channel, obtained from the self-consistent 1D Schrödinger-Poisson solution discussed above.
We use the FET model shown in Fig. 6.1, where the x-axis is along the channel and the z-axis is along the growth direction. The model also considers the presence of a drain (R_D) and source (R_S) resistance. When a

drain bias (V_D) is applied, the potential along the channel may be considered to vary gradually from the source to the drain. In this situation it is possible to calculate the sheet charge density n_s in different sections of the channel, provided that one considers the proper potential V(x) (on the top surface). Since generally V_D is positive, while V_S is zero, V(x) contributes to the channel depletion and the sheet charge density n_s for the generic *x* section of the FET will therefore be:

$$n_s(x) = n_s(V_G - V(x))$$

Since we deal with unipolar devices, we can neglect diffusion contributions and the source-to-drain current I_{DS} is given by:

$$I_{DS} = -qWv(x)n_s(x) \qquad \text{[Eq.6.3]}$$

where W is the gate width and v(x) the electron mean velocity, taken independent from the transverse coordinate.

The drift velocity dependence on the longitudinal electric field is given by:

$$v(x) = \frac{\mu_0 F(x)}{1 + \frac{F(x)}{F_C}}$$

where F(x) is the electric field, μ_0 is the low field mobility and $F_c = v_{sat}/\mu_0$ is the electric field at saturation. Parasitic components are included explicitly through the value of the drain and source resistance (R_D, R_S).

For a given value of I_{DS}, we can calculate the corresponding V_D by solving Eq. 6.3. The explicit equation for the current is:

$$I_{DS} = qW \frac{\mu_0 F(x)}{1 + \frac{F(x)}{F_C}} n(V_G - V(x))$$

The numerical solution is based on the discretization of this expression on a number N of sections, each one with amplitude h, so that Nh=L, where L is the gate length. Given the (i-1)-th section potential, the i-th potential is $V_i = V_{i-1} + F_i h$ where F_i is the i-th section electric field. We have then N relations:

$$I_{DS} = qW \frac{\mu_0 F_i}{1 + \frac{F_i}{F_C}} n(V_G - V_{i-1} - F_i h)$$

Since the (i-1)-th section potential is known from the previous step, this is a non-linear equation in the unknown F_i. Solving iteratively for all the N sections, one obtains the value of drain voltage V_D consistent with the assumed current. Repeating this procedure for a suitable range of values of I_{DS}, one obtains the set of corresponding V_{DS} values and builds the device I-V characteristics.

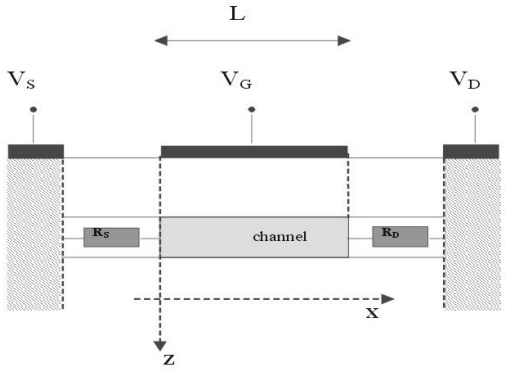

Fig. 2.13. Schematic representation of the quasi-2D FET model implemented.

2.6.3 Non-linear polarization model

Contrary to early device modelling, where linear interpolation between the values of parent binary compounds was largely used, it was recently shown that macroscopic polarization in nitride alloys is a non-linear function of composition [18].
In Ref. [18], the so-called bowing parameters, including higher-order dependence on molar fraction, are given for spontaneous polarization in AlGaN alloys.
Besides, the authors provide empirical expressions of the dependence of piezoelectric polarization for GaN and AlN on the basal strain $\varepsilon(x) = [a_0 - a(x)]/a(x)$, where a_0 and $a(x)$ are the lattice constants of the substrate and of the unstrained alloy respectively. Given these values, a linear interpolation (Vegard law) provide the alloy piezoelectric polarization .

Our 1D Schrödinger-Poisson simulation code includes a built-in polarization model which can reproduce non linear features.
In fact, basing on the appropriate values of elastic and piezoelectric constants for the materials GaN and AlN (wurtzite structure) , a linear interpolation of these physical quantities is used in the AlGaN alloy , yielding the correct values for piezoelectric polarizations, which reproduce the non-linear behaviour.
We tested our non-linear polarization model on the sample structure of Ref.18, calculating the sheet charge densities in a AlGaN/GaN structure with a 30 nm AlGaN barrier, for several Al molar fractions. We found a very good agreement with the experimental sheet charge densities reported in Ref.18, as is shown in fig. 2.14 Here, the values calculated with the non-linear model are also compared with those obtained using a linear model for spontaneous polarization: it is clear that a linear model is not sufficiently accurate. Besides, our results are almost coinciding with those calculated with the non-linear model of Ref. 18.

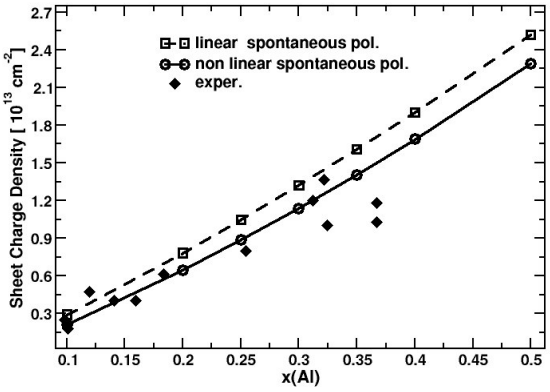

Fig. 2.14. 2DEG carrier concentration with non-linear polarization model, for a 30 nm AlGaN barrier HFET.

2.7 Numerical calculation of elastic deformations in a lattice mismatched structure

2.7.1 Elastic energy.

The main object of this study is a heterostructure, i.e. a crystal that does not exist in nature but is grown artificially and consists of different phases, for example GaN, AlN, Si_3N_4 and many others. It is due to great success in the growth technology (see for example Ref. [19-27]) that semiconductor devices have become so spread and useful. Most commonly, lattice mismatch between the two constituents of the structure induces an elastic strain. Nowadays there are two approaches to deal with the elastic deformations: the *atomistic* and the *continuous media* approach. The idea of the atomistic (or microscopic) approach is to find the atomic configuration that minimizes the total energy. This task is, obviously, computationally heavy and could be performed without simplifications only for systems of about 100 atoms. This number corresponds to the systems of *molecular electronics* [28] but is too small for conventional heterostructures studied here. There are, however, empirical approaches to the problem known as the *valence force methods* [29], where the ion-ion interaction is parametrized. This approximation is still computationally heavy but can handle structures with millions of atoms [30].

In this study we use the continuous media approach. It assumes that the heterostructure layers are subjected to "chemical" forces in order to match the atomic positions at heterointerfaces. The layers react to these forces like macroscopic samples according to the laws of elasticity theory [31]. We calculated the elastic deformation of our model structures by using a continuous medium model [32, 33] thus assuming heterostructures without lattice structure defects. In this approach, we consider the small displacements of the material points **u**, defined as

$$\mathbf{u} = \mathbf{r} - \mathbf{r}', \qquad (7.1)$$

where $\mathbf{r}'$ and $\mathbf{r}$ are coordinates of a point before and after deformation. We define a local tensor ζ_{ij}, related to a deformation at a point:

$$\varsigma_{ij} = \frac{\partial u_i}{\partial x_j} \quad (7.2)$$

Since only the symmetric part of ζ_{ij} describes "pure" deformations without rotation, the strain tensor ε_{ij}
is defined as:

$$\varepsilon_{ij} = \frac{1}{2}\left(\frac{\partial u_i}{\partial x_j} + \frac{\partial u_j}{\partial x_i}\right) \qquad (7.3)$$

The diagonal components of ε_{ij} describe stretching or shrinking of the sample, while the off-diagonal components correspond to shear deformations. The energy of the elastic deformation is a quadratic form of ε_{ij}:

$$E = \frac{1}{2}\int C_{ijkl}(\mathbf{r}')\varepsilon_{ij}(\mathbf{r}')\varepsilon_{kl}(\mathbf{r}')d^3\mathbf{r}', \qquad (7.4)$$

where C_{ijkl} is the elasticity tensor.

In Eq. (7.4) the integration has to be performed over a non-deformed volume $d^3\mathbf{r}'$ (see. [34]). But due to a specific character of our problem we know the geometry of a heterostructure after the deformation rather than shape and size of non-deformed layers. Considering deformation as coordinate transformation $\mathbf{r}' \to \mathbf{r}$ we get for the elastic energy:

$$E = \frac{1}{2}\int C_{ijkl}(\mathbf{r})\varepsilon_{ij}(\mathbf{r})\varepsilon_{kl}(\mathbf{r})\left|\frac{\partial \mathbf{r}'}{\partial \mathbf{r}}\right| d^3\mathbf{r}\,, \qquad (7.5)$$

where $\left|\frac{\partial \mathbf{r}'}{\partial \mathbf{r}}\right|$ is the Jacobian of the transformation. We consider the case of a small strain only, so the Jacobian can be approximated linearly as:

$$\left|\frac{\partial \mathbf{r}'}{\partial \mathbf{r}}\right| = 1 - \mathrm{Tr}(\varepsilon_{ij}) \qquad (7.6)$$

so the elastic energy reads:

$$E = \frac{1}{2}\int C_{ijkl}(\mathbf{r})\varepsilon_{ij}(\mathbf{r})\varepsilon_{kl}(\mathbf{r})(1-\varepsilon_{pp}(\mathbf{r}))d^3\mathbf{r} \qquad (7.7)$$

As it was mentioned above, we assume a coherent growth, so that all distinct lattices are perfectly matched at the interface [34]. We used the following computational procedure in order to minimize the elastic energy of Eq. (7.7), while imposing the lattice matching conditions:

1. We first map a rectangular non-homogeneous simulation grid over the whole structure in such a way that all the material interfaces coincide with the grid lines. In this case the principal axes do not necessarily coincide with the high symmetry directions of the lattice. In doing so the Cartesian simulation system can have non-orthogonal basis. However, in this study we limit ourselves to the case of an orthogonal simulation system, possibly rotated with respect to the crystallographic one. Since the simulation system axes should coincide with the three non-coplanar Bravais lattice vectors, we can define a conventional rectangular unit cell which axes are parallel to the simulation system basis vectors.

In the case of a cubic lattice materials we can always select two orthogonal crystallographic directions both orthogonal to the growth direction. This does not hold for a wurzite crystal. Therefore, the orthogonality of the simulation system limits us in the growth direction choice. Namely, we can choose for a simulation system either the crystal system defined as:

$$\begin{aligned} x &= [10\bar{1}0] \\ y &= [\bar{1}2\bar{1}0] \\ z &= [0001] \end{aligned} \qquad (7.8)$$

or a system rotated around z axis by $\pi/3$ angle.

2. We then introduce a "lattice-matching" deformation ε_{ij}^0 which transforms any unstrained unit cell of the heterostructure material in order to match it to the reference lattice (see Fig. 2.15b). For the reference lattice we take the lattice of the substrate. Let b_1^r, b_2^r, b_3^r be the dimensions of the previously defined unit cell of the reference lattice. In the coordinate system with the axis parallel to Bravais vectors of the conventional cell we have:

$$\varepsilon_{ij}^r(\mathbf{r}) = W(\mathbf{r})\delta_{ij}\frac{b_i^r - b_i(\mathbf{r})}{b_i(\mathbf{r})}\text{, where} \qquad (7.9)$$

$$W(r) = \begin{cases} 1, & \text{if } \mathbf{r} \text{ belongs to a deformed layer} \\ 0, & \text{if otherwise} \end{cases} \qquad (7.10)$$

where $b_i(\mathbf{r})$ are the equilibrium conventional cell lattice constants of the deposited material. In a particular case of a heterostructure composed of zinc-blende materials any Bravais vector is proportional to the only lattice constant. Therefore, the lattice matching deformation in any coordinate system reads:

$$\varepsilon_{ij}^r(\mathbf{r}) = W(\mathbf{r})\delta_{ij}\frac{a^r - a(\mathbf{r})}{a(\mathbf{r})} \qquad (7.11)$$

In the case of a wurtzite crystal the ε_{ij}^0 tensor representation depends on the coordinate system. In

the crystal system we have:

$$\varepsilon_{ij}^{0}(\mathbf{r}) = \begin{pmatrix} \dfrac{a_x^r - a_x(\mathbf{r})}{a_x(\mathbf{r})} & 0 & 0 \\ 0 & \dfrac{a_y^r - a_y(\mathbf{r})}{a_y(\mathbf{r})} & 0 \\ 0 & 0 & \dfrac{a_z^r - a_z(\mathbf{r})}{a_z(\mathbf{r})} \end{pmatrix} \qquad (7.12)$$

3. The deformation tensor now is expressed via the displacements $\tilde{\mathbf{u}}(\mathbf{r})$ defined with respect to the matched lattice:

$$\varepsilon_{ij} = \tilde{\varepsilon}_{ij} + \varepsilon_{ij}^{0}, \text{ where} \qquad (7.13)$$

$$\tilde{\varepsilon}_{ij} = \frac{1}{2}\left(\frac{\partial \tilde{u}_i}{\partial x_j} + \frac{\partial \tilde{u}_j}{\partial x_i} \right) \qquad (7.14)$$

2.7.2 Free-standing and grown on a substrate heterostructures

There are two different situations that we consider.

1. **The structure is grown on a very thick substrate.** It has been shown [23] that the minimization of the elastic energy will require a zero strain in the substrate far away from the heterostructure. Therefore, we apply Dirichlet boundary conditions for $\tilde{\mathbf{u}}(\mathbf{r})$ at the plane that separates the simulation domain from the rest of the substrate. Since the reference lattice constants are those of the substrate the strain will be zero in it.

2. **The substrate thickness is comparable to the deposited layers thickness.** In this case the total substrate volume is considered as part of the simulation domain. In this case the lattice matching deformation parameters b_x^r, b_y^r, b_z^r (see Eq. (9)) are not fixed but should be considered as the parameters that minimize the elastic energy (Eq. (4)). Also in this case the lattice matching strain tensor ε_0 can have non-zero off-diagonal components.

2.7.3 Homogeneous and periodically repeated structures

There are two different types of periodic structures: the structures that are homogeneous in one or two directions (quantum wells (QWs) and quantum wires (QWRs)) and the structures that are periodically repeated in space along one, two or three directions (superlattices (SLs)).

If the structure is periodically repeated in space then for the displacement $\tilde{\mathbf{u}}(\mathbf{r})$ we have:

$$\tilde{\mathbf{u}}(\mathbf{r} + \mathbf{L}) = \tilde{\mathbf{u}}(\mathbf{r}) \qquad (7.15)$$

where $\mathbf{L}$ in the periodicity vector. For the sake of correctness all material parameter must obey the same periodicity.

The displacements $\tilde{\mathbf{u}}(\mathbf{r})$ are defined with respect to a reference lattice. In the case of a thick substrate the reference lattice is defined *a priori*. In the opposite case the reference lattice has to be

found *a posteriori* with its symmetry does not necessarily coinciding with the undeformed lattice symmetry. Really, the three reference lattice constants are different in general case. Moreover, the reference lattice can even have non-zero shear deformations. Having this in mind, we define the independent variables that are necessary for the simulation of a structure without a thick substrate. Since these variables are to define shape and size of the supercell, we'll cal them as *supercell variables.*

Structure, periodic (homogeneous) in one direction. Let the structure is periodic (homogeneous) in along direction *x*. The supercell variable is b_x^r and the lattice matching deformation tensor is:

$$\varepsilon_{ij}^0(\mathbf{r}) = \begin{pmatrix} \dfrac{b_x^r - a_x(\mathbf{r})}{a_x(\mathbf{r})} & 0 & 0 \\ 0 & \dfrac{a_y^r - a_y(\mathbf{r})}{a_y(\mathbf{r})} & 0 \\ 0 & 0 & \dfrac{a_z^r - a_z(\mathbf{r})}{a_z(\mathbf{r})} \end{pmatrix} \qquad (7.16)$$

where a_x^r and a_y^r are the arbitrary constants. From the computational point of view it is better to take them equal to the lattice constant of the material that occupies the largest volume in the heterostructure.

Structure, periodic (homogeneous) in two directions. Let the structure is periodic(homogeneous) in two directions *x* and y. Then the supercell variables are b_x^r, b_y^r and ε_{xy}^0, and the lattice matching deformation gets:

$$\varepsilon_{ij}^0(\mathbf{r}) = \begin{pmatrix} \dfrac{b_x^r - a_x(\mathbf{r})}{a_x(\mathbf{r})} & \varepsilon_{xy}^0 & 0 \\ \varepsilon_{xy}^0 & \dfrac{b_y^r - a_y(\mathbf{r})}{a_y(\mathbf{r})} & 0 \\ 0 & 0 & \dfrac{a_z^r - a_z(\mathbf{r})}{a_z(\mathbf{r})} \end{pmatrix} \qquad (7.17)$$

where a_z^r is the arbitrary constant.

Structure, periodic (homogeneous) in three directions. The supercell variables are b_x^r, b_y^r, b_z^r and $\varepsilon_{xy}^0, \varepsilon_{xz}^0, \varepsilon_{yz}^0$ and the lattice matching deformation gets:

$$\varepsilon_{ij}^0(\mathbf{r}) = \begin{pmatrix} \dfrac{b_x^r - a_x(\mathbf{r})}{a_x(\mathbf{r})} & \varepsilon_{xy}^0 & \varepsilon_{xz}^0 \\ \varepsilon_{xy}^0 & \dfrac{b_y^r - a_y(\mathbf{r})}{a_y(\mathbf{r})} & \varepsilon_{zy}^0 \\ \varepsilon_{xz}^0 & \varepsilon_{zy}^0 & \dfrac{b_z^r - a_z(\mathbf{r})}{a_z(\mathbf{r})} \end{pmatrix} \qquad (7.18)$$

2.7.4 Minimization of the elastic energy

The elastic energy Eq. (7) can be written as:

$$E = \frac{1}{2}\Omega_{\parallel}\int C_{ijkl}(\mathbf{r})\varepsilon_{ij}(\mathbf{r})\varepsilon_{kl}(\mathbf{r})(1-\varepsilon_{pp}(\mathbf{r}))d^{N}\mathbf{r}, \qquad (7.19)$$

where N is the dimension of the heterostructure and $\Omega_{\parallel}$ is the measure of the heterostructure "parallel" space. If the heterostructure is grown on a substrate then $\Omega_{\parallel}$ can be considered as a constant and, therefore, can be put to 1 while minimizing the elastic energy. In the case of a free-standing structure the parallel space measure is a variable, namely, it is equal to:

$$\Omega_{\parallel} = A\prod b_i^r \qquad (7.20)$$

where A is a constant. The Eq. (20) holds both for homogeneous and periodic structures. The constant A can be expressed as $A = \prod A_i$, where i runs over variable reference lattice constants:

$$A_i = \begin{cases} 1, i \text{ is a homogeneous direction} \\ \dfrac{N_i}{L_i}, i \text{ is a periodic direction} \end{cases} \qquad (7.21)$$

where N_i and L_i are the number of unit cells and length along the period. Finally, the functional that has to be minimized takes the form:

$$E = \frac{1}{2}\left(\prod b_k^r\right)\int\limits_{\Omega_{\perp}} C_{ijkl}(\mathbf{r})\varepsilon_{ij}(\mathbf{r})\varepsilon_{kl}(\mathbf{r})(1-\varepsilon_{pp}(\mathbf{r}))d^{N}\mathbf{r} = \qquad (22)$$

$$= \frac{1}{2}\left(\prod b_k^r\right)\int\limits_{\Omega_{\perp}} L\left(\frac{\partial u_i}{\partial x_j}, b_i^r, \varepsilon_{ij}^0\right)d^{N}\mathbf{r} \qquad (23)$$

with

$$L = C_{ijkl}(\mathbf{r})\varepsilon_{ij}(\mathbf{r})\varepsilon_{kl}(\mathbf{r})(1-\varepsilon_{pp}(\mathbf{r}))d^{N}\mathbf{r} \qquad (7.24)$$

Minimization of the functional of Eq. (7.22) is done assuming continuous partial derivatives of $\mathbf{u}$. We get:

Variation $\delta E = 0$ along $\dfrac{\partial u_i}{\partial x_j}$ gives:

$$\frac{1}{2}\frac{\partial}{\partial x_j}\frac{\partial L}{\frac{\partial u_i}{\partial x_j}} = 0 \qquad (7.25)$$

Derivative $\dfrac{\partial E}{\partial b_j^r} = 0$ gives:

$$\frac{1}{2}\left(\frac{1}{b_j^r}\int L d^{N}\mathbf{r} + \int\frac{\partial L}{\partial b_j^r}d^{N}\mathbf{r}\right) = 0 \qquad (7.26)$$

Derivative $\dfrac{\partial E}{\partial \varepsilon_{ij}^0} = 0$ gives:

$$\frac{1}{2}\int\frac{\partial L}{\partial \varepsilon_{ij}^0}d^{N}\mathbf{r} = 0 \qquad (7.27)$$

We get from Eq. (7.25) a set of equations for $j = 1,2,3$:

$$\frac{\partial}{\partial x_i}\left(C_{ijkl}\left(1-\frac{\partial u_p}{\partial x_p}-\varepsilon_{gg}^0\right)\left(\frac{\partial u_k}{\partial x_l}+\varepsilon_{kl}^0\right)\right) - \frac{1}{2}\frac{\partial}{\partial x_i}C_{mnkl}\left(\frac{\partial u_m}{\partial x_n}+\varepsilon_{nm}^0\right)\left(\frac{\partial u_k}{\partial x_l}+\varepsilon_{kl}^0\right)\delta_{ij} = 0 \qquad (7.28)$$

We get from Eq. (7.26) we get a set of equations for each variable lattice constant b_j^r, if any:

$$\frac{1}{2}\frac{1}{b_j^r}\int C_{mnkl}\left(\frac{\partial u_m}{\partial x_n}+\varepsilon_{mn}^0\right)\left(\frac{\partial u_k}{\partial x_l}+\varepsilon_{kl}^0\right)\left(1-\frac{\partial u_p}{\partial x_p}-\varepsilon_{gg}^0\right)d^N\mathbf{r}+$$
$$\int C_{ijkl}\left(\frac{\partial u_k}{\partial x_l}+\varepsilon_{kl}^0\right)\frac{1}{a_i}\delta_{ij}\left(1-\frac{\partial u_p}{\partial x_p}-\varepsilon_{gg}^0\right)d^N\mathbf{r}-$$
$$\frac{1}{2}\int C_{mnkl}\left(\frac{\partial u_m}{\partial x_n}+\varepsilon_{mn}^0\right)\left(\frac{\partial u_k}{\partial x_l}+\varepsilon_{kl}^0\right)\frac{1}{a_i}d^N\mathbf{r}=0 \tag{7.29}$$

We get from Eq. (7.27) for each shear variable ε_{ij}^0, if any:

$$\int C_{ijkl}\left(\frac{\partial u_k}{\partial x_l}+\varepsilon_{kl}^0\right)\left(1-\frac{\partial u_p}{\partial x_p}-\varepsilon_{gg}^0\right)d^N\mathbf{r}=0 \tag{7.30}$$

If the structure is homogeneous in one (QWR) or two (QW) directions then the dimension of the simulation domain reduces correspondingly and the derivatives over the "homogeneous" coordinates in Eq. (7.28-30) vanish. However, the displacements $\tilde{\mathbf{u}}(\mathbf{r})$ are always three-dimensional vector field. In the Fig. 2.15c,d) we show a deformed layer grown on a substrate. The system is homogeneous in *x* and *y* directions, but the displacements $\tilde{\mathbf{u}}(\mathbf{r})$ can have non-zero components not only in the growth direction *z*. In a particular case (see Fig. 2.15c) due to the crystal symmetry ($z \parallel [001]$) the displacements are parallel to the growth direction, but in a general case (Fig. 2.15d) $\tilde{\mathbf{u}}(\mathbf{r})$'s have also non-zero x and y components that correspond to a shear deformation.

2.7.5 Non-linear system solution method

Equations (7.28-30) are non linear. We solve them by means of simple iterations. We introduce Jacobian
J and energy density E as functions of strain at each iteration:

$$J(\mathbf{r})=1-\varepsilon_{ii}(\mathbf{r}) \tag{31}$$

$$\mathrm{E}(\mathbf{r})=\frac{1}{2}C_{ijkl}(\mathbf{r})\varepsilon_{ij}(\mathbf{r})\varepsilon_{kl}(\mathbf{r}) \tag{32}$$

Taking *J* and E from the previous iteration we get a linear system of equations.
1. Master equation:

$$\frac{\partial}{\partial x_i}\left(C_{ijkl}(\mathbf{r})J(\mathbf{r})\left(\frac{\partial u_k}{\partial x_l}+\varepsilon_{kl}^0\right)\right)-\frac{\partial}{\partial x_i}\mathrm{E}(\mathbf{r})\delta_{ij}=0,\ j=1,2,3 \tag{7.33}$$

2. Superlattice equation:

$$\int \mathrm{E}(\mathbf{r})\left(\frac{J(\mathbf{r})}{b_j^r}-\frac{1}{a_j(\mathbf{r})}\right)d^N\mathbf{r}+\int C_{ijkl}(\mathbf{r})J(\mathbf{r})\frac{\delta_{ij}}{a_i(\mathbf{r})}\left(\frac{\partial u_k}{\partial x_l}+\varepsilon_{kl}^0\right)d^N\mathbf{r}=0,\quad j\ =\ j_0 \tag{7.34}$$

$$\int C_{ijkl}(\mathbf{r})J(\mathbf{r})\left(\frac{\partial u_k}{\partial x_l}+\varepsilon_{kl}^0\right)d^N\mathbf{r}=0,\quad i=i_0,\ j\ =\ j_0 \tag{7.35}$$

If we neglect difference between deformed and undeformed geometry, then the equations become linear and simple:

1. Master equation:

$$\frac{\partial}{\partial x_i}\left(C_{ijkl}(\mathbf{r})\left(\frac{\partial u_k}{\partial x_l} + \varepsilon_{kl}^0 \right) \right) = 0,\ j = 1,2,3 \tag{7.36}$$

2. Superlattice equation:

$$\int C_{ijkl}(\mathbf{r}) \frac{\delta_{ij}}{a_i(\mathbf{r})} \left(\frac{\partial u_k}{\partial x_l} + \varepsilon_{kl}^0 \right) d^N\mathbf{r} = 0, \quad j = j_0 \tag{7.37}$$

$$\int C_{ijkl}(\mathbf{r}) \left(\frac{\partial u_k}{\partial x_l} + \varepsilon_{kl}^0 \right) d^N\mathbf{r} = 0, \quad i = i_0,\ j = j_0 \tag{7.38}$$

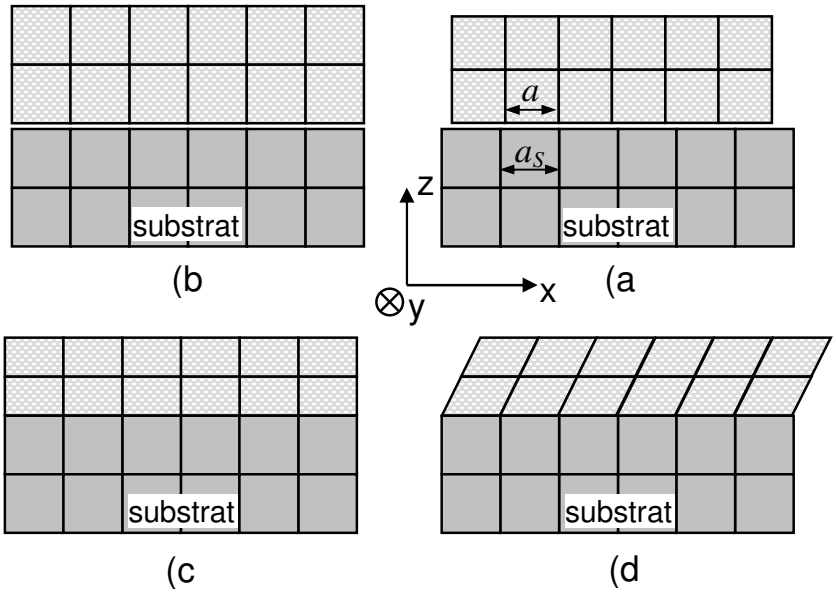

Figure 2.15: Lattice mismatched materials as constituent elements of the heterostructure: a) before contact; b) considering the lattice matching deformation $\varepsilon_{ij}^0 = \frac{a_s - a}{a}$. After minimization of the elastic energy the two situations are possible: c) without shear deformation; d) with non-zero shear

2.8 References

[1] A. Sleiman, et al. IEEE. Trans. El. Dev. Oct 2001.
[2] M. Saraniti et al., IEEE Trans. on Comp. Aided Des. of Int. Circuits and Systems, vol.15, n. 2, pp. 141-150, Feb 1996.
[3] C. Canali et al., IEEE Trans. El. Dev., vol. ED-43 (11) p. 1769,
[4] J. Kolnik et al., J. Appl. Phys. 78, p. 1033, 1995.
[5] J. Kolnik et al., J. Appl. Phys. 81, p. 726, 1997.
[6] F. Dessenne. Université des Sciences et Techniques de Lille. These de Doctorat, February 1998.

[7] I. H. Oguzman et al., J. Appl. Phys., vol. 81, pp.7827-7834, 1997.
[8] M. V. Fiscetti. IEEE Trans. El. Dev., vol. 38, pp. 634-649, 1991.
[9] Y. Yando et al., IEEE Electron Device Lett., vol. 20, pp. 454-456, 1999.
[10] M. Farahmand et al., IEEE Trans. El. Dev., vol. 48 (3) pp. 535-542, 2001.
[11] DESSIS 9.1 Reference manual, ISE AG, Zurich (Switzerland),1999. http://www.ise.ch/
[12] A. G. Chynoweth, "Ionization rates for electrons and holes in Silicon", *Phys. Rev.*, vol. 109, no. 5, pp. 1537–1540, 1958.
[13] Kolnik et al, "Monte Carlo calculation of electron initiated impact ionization in bulk zinc-blende and wurtzite GaN", J. Appl. Phys., Vol. 81, No. 2, 15 January 1997.
[14] Kazuaki Kunihiro, Kensuke Kasahara, Yuji Takahashi, and Yasuo Ohno; " Experimental Evaluation of Impact Ionization Coefficients in GaN"; IEEE Electron Device Lett, Vol. 20, N°. 12, December 1999.
[15] A. Reklaitis, L. Reggiani; "Monte Carlo study of hot-carrier transport in bulk wurtzite GaN and modeling of a near-terahertz impact avalanche transit time diode"; J. Appl. Phys., Vol. 95, No. 12, 15 June 2004.
[16] F.Bernardini, V. Fiorentini and D.Vanderbilt, Phys. Rev. B, 56, R10024, 1997
[17] O. Ambacher et al., J.Phys. :Condens. Matter 14 (2002), p. 3399
[18] V. Fiorentini, F.Bernardini, O.Ambacher, Appl. Phys. Lett. 80, 1204 (2002)
[19] B. K. Ridley, W. J. Schaff, and Eastman, L. F., "Theoretical model for polarization superlattices: energy levels and intersubband transitions" *Journal of Applied Physics* **94**, p. 3792, 2003
[20] E. Anastassakis, Solid State Comm., **78**, pp. 347-350, (1991)
[21] N.J. Ekins-Daukes, K. Kawaguchi, and J. Zhang "Strain-Balanced Criteria for Multiple Quantum Well Structures and Its Signature in X-ray Rocking Curves", *Crystal growth and design* **2**, p. 287, 2002
[22] P. Y. Yu and M. Cardona, *Fundamentals of Semiconductors*, Springer, 1996.
[23] L. A. Zepeda-Ruiz, R. I. Pelzel, B. Z. Nosho, W. H.Weinberg, and D. Maroudas, "Deformation behaviour of coherently strained InAs/GaAs(111)*A* heteroepitaxial systems: Theoretical calculations and experimental measurements," *Journal of Applied Physics* **90**, p. 2689, 2001.
[24] S. Guha, A. Madhukar, and K. Rajkumar, "Onset of incoherency and defect introduction in the initial stages of molecular beam epitaxical growth of highly strained $In_xGa_{1-x}As$ on GaAs(100)," *Applied Physics Letters* **57**, p. 2110, 1990.
[25] S.-Z. Chang, T.-C. Chang, and S.-C. Lee, "The growth of highly mismatched $In_xGa_{1-x}As$ ($0.28 < x < 1$) on GaAs by molecular-beam epitaxy," *Journal of Applied Physics* **73**, p. 4916, 1993.
[26] R. Nötzel, U. Jahn, Z. Niu, A. Tranpert, J. Fricke, and H.-P. Sch¨onherr, "Device quality submicron arrays of stacked sidewall quantum wires on patterned GaAs(311)A substrates," *Applied Physics Letters* **72**, p. 2002, 1998.
[27] R. Nötzel, M. Ramsteiner, J. Menninger, A. Tranpert, H.-P. Schönherr, L. Däweritz, and K.H. Ploog, "Patterned growth on high-index GaAs(n11) substrates: Application to sidewall quantum wires," *Journal of Applied Physics* **80**, p. 4108, 1996.
[28] J. Taylor, H. Guo, and J. Wang, "*Ab initio* modelling of quantum transport properties of molecular electronic devices," *Physical Review B* **63**, p. 245407, 2001.
[29] P. Keating, "Effect of invariance requirements on the elastic strain energy of crystals with application to the diamond structure," *Physical Review* **145**, p. 637, 1966.
[30] G. Klimeck, F. Oyafuso, R. C. Bowen, and T. B. Boykin, "3-d atomistic nanoelectronic modeling on high performance clusters: multimillion atom simulations," *Superlattices and Microstructures* **31**, p. 171, 2002.
[31] L. Landau and E. Lifshitz, *Course of Theoretical Physics: Theory of Elasticity*, Pergamon, Oxford, 1986.
[32] C. Pryor, M.-E. Pistol, and L. Samuelson, "Electronic structure of strained InP/Ga0.51In0.49P quantum dots," *Physical Review B* **56**, p. 10404, 1997.
[33] B. Jogai, "Three-dimensional strain field calculations in coupled InAs/GaAs quantum dots," *Journal of Applied Physics* **88**, p. 5050, 2000.
[34] L. De Caro and L. Tapfer, "Elastic lattice deformation of semiconductor heterostructures grown on arbitrarily oriented substrate surfaces," *Physical Review B* **48**, p. 2298, 1993.

Chapter 3

PREMATURE SATURATION AND CURRENT DISPERSION PHENOMENA

3.1 INTRODUCTION

GaN-based HEMTs are receiving great attention because of their potential applications to high power and high temperature microwave devices [1]. However, unexpected low performance on DC and RF regimes have been reported.

DC characteristics suffer of a *premature saturation* of the I_{DSS} which depends on surface and GaN-substrate interface fixed charges induced by polarisation fields and surface defects. The output DC current and the static gain are lower than expected by considering the 2DEG density. The premature saturation is not a time dependent phenomenon.

On the other hand, time dependent trapping mechanism have to be considered since slow current transients are often observed when the drain voltage or the gate voltage is changed abruptly [2]. This is called *drain lag* or *gate lag*, and is critical in circuit applications. Slow transients mean that the DC I-V curves and the AC I-V curves become quite different, resulting in lower AC power available than that expected from the DC operation [1,2]. This current reduction is also referred to as *current slump*, *current compression*, *current collapse* and *rf dispersion*. These effects are regarded as trap-related, and there are many experimental works reported on these phenomena [2–8]. However, only a few theoretical works have been recently reported for GaN-based FETs, [8–10] although several numerical analyses were made for GaAs based FETs.

In this work, we have made systematic simulations of GaN HEMTs on a semi-insulating buffer layer considering different energy levels and trap types, such as donor like and deep acceptor like. According to the experimental results we considered four different location for the traps, namely AlGaN/SiN interface traps, AlGaN bulk traps, GaN bulk traps and contact induced traps. For all these configurations we will describe in detail how they affect the gate lag and the drain lag of the HEMTs. Moreover, we will study the influence of passivation and of field plate technology on the current compression.

3.2 PREMATURE SATURATION DUE TO SURFACE STATES

The typical HEMT structure investigated in this work is sketched in Fig. 3.1 and are grown on sapphire. The epilayer consists of a 1 µm undoped GaN channel, and 32 nm of an undoped $Al_{0.26}GaN$. The gate length is 1.2 µm and drain source separation of 5.0 µm.

In order to account for the spontaneous and piezoelectric effects, polarization charges with density σ=1.3 x 10^{13} cm^{-2} were introduced at AlGaN/GaN interface, as fixed charges. This positive charges induces 2DEG in the GaN close to the interface. The HEMT simulation was performed solving the 2-D Poisson equation self-consistently coupled with MC dynamics.

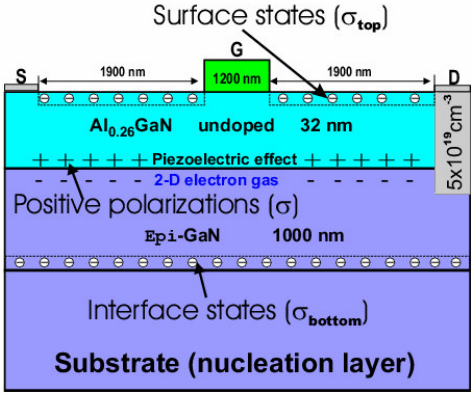

Fig. 3.1. Schematic cross section of the investigated device structures. Surface (σ_{top}) and interface (σ_{bottom}) charges are also shown. The polarization charges induced 2-D electron gas at the GaN/$Al_{0.26}GaN$ interface are also depicted. The ohmic contacts are simulated by doping the AlGaN under the contact down to the channel with a donor density of 5×10^{19} cm^{-3}. The doping

for Drain and Source (not shown) is the same.

As starting point we have simulated the HEMT considering only the positive polarization charges (σ=1.3 x 10^{13} cm^{-2}) at the AlGaN/GaN interface (Fig. 3.1). Figure 3.2 shows the calculated (continuous line) transfer characteristics I_{DS}-V_{GS} for the HEMT without surface and interface charges (σ_{top}=0, and σ_{bottom}=0) and compared with experimental measurements (continuous line with circle) at V_{DS}=10V, where the current is saturated. As can be seen, the calculated drain current is higher than measurements (courtesy of Alenia Marconi System – 2003). The calculated drain current reaches 1100 mA/mm at (V_{GS}=0V) while the typical experimental current for such kind of structure saturated at 400 mA/mm. Calculated pinch-off (-4.5V) is slightly higher than measurement of (-4V). From this comparison it is obvious that additional mechanisms exist, capable of explaining the premature saturation of the drain current observed by measurements such as surface charges (σ_{top}) and interface charges (σ_{bottom}). We first consider the effect of the surface charges at the ungated surface of the HEMT (Fig. 3.1) while holding the interface charges σ_{bottom}=0. MC drain currents have been calculated for various density σ_{top}. By increasing σ_{top} the drain current (dashed line) drops continuously as well as the slope of I_{DS}-V_{GS} (Fig. 3.2). Consequently the transconductance is reduced.
The decreasing of the current is associated with a slight shift of the threshold toward higher voltages. As can be seen in Fig. 3.2 the experimental drain current fits quite well the calculation profile with the need to include a surface charges σ_{top} of 1.1 x 10^{13} cm^{-2}, even though the experimental transconductance results higher than the simulation.

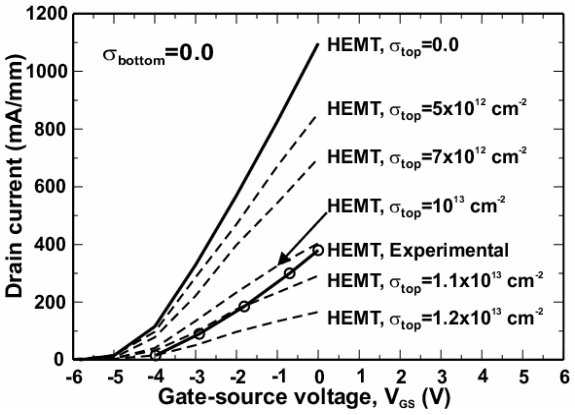

Fig. 3.2 Experimental and MC I_{DS}-V_{GS} characteristics obtained at V_{DS}=10V. The continuous line with circle is for the HEMT obtained by experimental measurements. The continuous line is for HEMT without surface charges (σ_{top}=0.0) and interface charges (σ_{bottom} =0.0) obtained by MC. The dashed lines are for the HEMT with surface charges σ_{top} obtained by MC.

The slope of the transconductance, for a fixed device geometry, is determined by the 2DEG confinement. A higher transconductance means a higher confinement. In order to reproduce such result, the MC simulator has been then used to study the effect of substrate/GaN interface charges (σ_{bottom}) on the electrical characteristics of the HEMT.
Fig. 3.3 shows the calculated I_{DS}-V_{GS} for various density σ_{bottom} (dashed line) compared with experimental current (continuous with circle). Here σ_{top}=0, the effect of the bottom interface charges is to shift towards higher V_{GS} the pinch-off bias. The interface charges have no effect on the slope of I_{DS}-V_{GS} and so on the transconductance. This study shows that σ_{bottom}= 5.0 x 10^{12} cm^{-2} limit the performance of the HEMT producing the same current observed by measurements obtained for V_{GS} =0 V. This improved carrier confinement is the main reason for strong shift of the pinch-off voltage. Therefore the effect of the interface charges is to assure a better control of the channel.

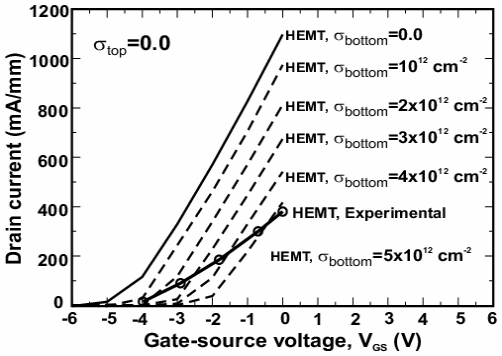

Fig. 3.3 Experimental and MC I_{DS}-V_{GS} characteristics obtained at V_{DS}=10V. The continuous line with circle is for the HEMT obtained by experimental measurements. The continuous line is obtained by MC for the HEMT without polarization charges (σ_{top} =0.0, and σ_{bottom}=0.0). The dashed lines are for HEMT with interface charges σ_{bottom} carried out by MC.

The simulation shows that neither the contribution of the air/AlGaN surface charges σ_{top} nor the substrate/GaN interface charges σ_{bottom} can alone explain the measured current saturation of the GaN-based HEMT. In order to produce the measured current we have simulated the HEMT of the Fig. 3.1 with both the surface charges σ_{top} and the interface charges σ_{bottom}. Fig. 3.4 shows the calculated I_{DS}-V_{GS} (line with square) for the HEMT by considering both the surface and interface charges. As it can be seen the experimental current (line with circle) is in good agreement with calculations for σ_{bottom}=1.5 x 10^{12} cm^{-2}, and σ_{top}=8.1 x 10^{12} cm^{-2}. Surface charges, thus dominate the experimental behaviour of the transcharacteristics while substrate charges contribute up to 20%.

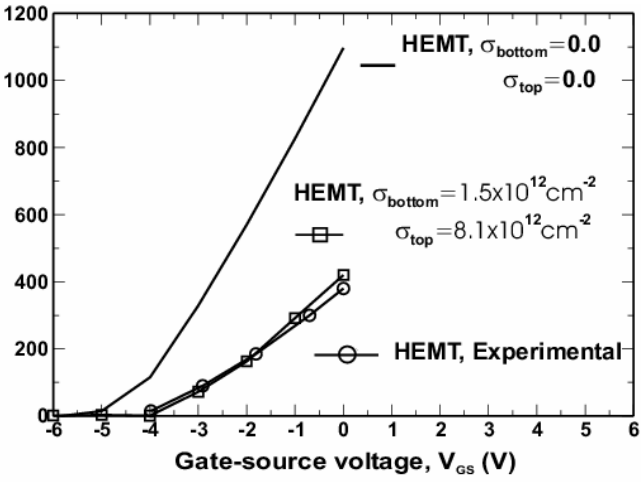

Fig. 3.4. Experimental and MC I_{DS}-V_{GS} characteristics obtained at V_{DS}=10V. The continuous line with circle is for the HEMT obtained by experimental measurements. The continuous line is the MC current obtained for HEMT without polarization charges (σ_{top}=0.0 and σ_{bottom}=0.0). The continuous line with square is the calculated current obtained for HEMT with polarization charges. Calculated and experimental currents are in good agreement for (σ_{bottom}=1.5 x 10^{12} cm^{-2} and σ_{top}=8.1 x 10^{12} cm^{-2}).

In conclusion a 2-D Monte Carlo model has been used to study the effect of the air/AlGaN surface and substrate/GaN interface charges on dc drain current in GaN-based HEMTs. MC and experimental I_{DS}-V_{GS} have been compared. We find that experimental I_{DS}-V_{GS} is 2 times lower than calculation. We have shown that the difference between the calculated and experimental dc drain current is due to the polarization-induced surface as well as interface charges. Moreover, the localisation of polarization charges have different effects on the electrical characteristics. While the surface charges act like a floating gate the interface charges induces a strong shift of the threshold voltage and improves the carrier confinement at the heterojunction. The calculations provided an estimation of polarization charges densities that limit the performance of the GaN-based HEMTs (1.1 x 10^{13} cm^{-2} for surface charges, 5.0 x 10^{12} cm^{-2} for GaN/substrate charges).

3.3 GATE LAG PHENOMENON

The Gate Lag (or Current Collapse) induces a strong RF Drain current dispersion and is one of the most limiting factors in the development of AlGaN/GaN HEMTs: various hypotheses have been made to

explain such effect. As a matter of fact, its entity is strictly connected with surface states present at the interface between AlGaN and air, and it is reduced by surface passivation [1] or by adding p^+ and n^+ doped layer at the access region [2].

An high density of surface states between the gate and source/drain contacts will act as virtual gates, modulating the depletion region, through changes in the trapped charge density. These virtual gates respond to a gate voltage pulse with times characteristic of carrier capture/emission phenomena, thus leading to a delay in I_D switching and to RF collapse.

There are two main models which have been suggested to explain these phenomena: the "electron" model [3] and the recent "hole" model [4] (see Fig. 3.5 and 3.6 for details). In the following we further introduce an original model (acceptor model) which may solve some of the problems presents in the hole model.

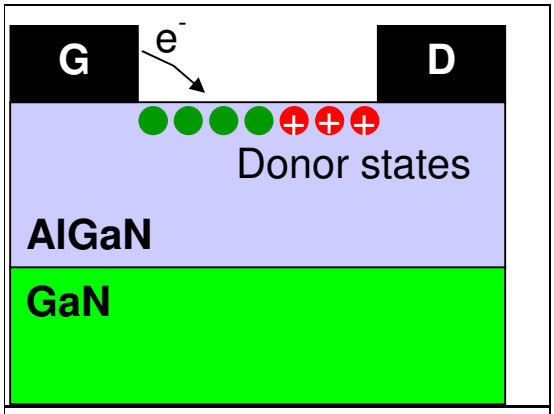

Fig. 3.5 "electron" model for current collapse.

For large $-V_{GS}$ donor states are filled with electrons and σ_{top} is negative and large (low current). When VGS becomes smaller electrons are detrapped with a given time constant

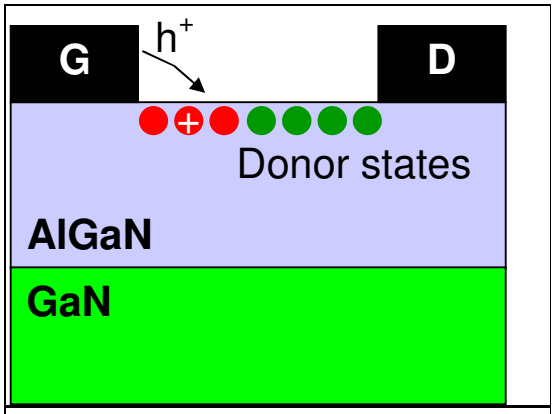

Fig. 3.6 "hole" model for current collapse.

For large $-V_{GS}$ donor states are filled (neutral) and σ_{top} is negative and large (low current). When V_{GS}

becomes smaller, holes flow from the gate into the surface accumulation layer and trapping mechanism will take place.

3.3.1 The "hole" model

In order to investigate current collapse induced by surface traps we have performed a two-dimensional time-dependent drift diffusion simulation of the device of Fig.3.7 using the DESSIS tool.

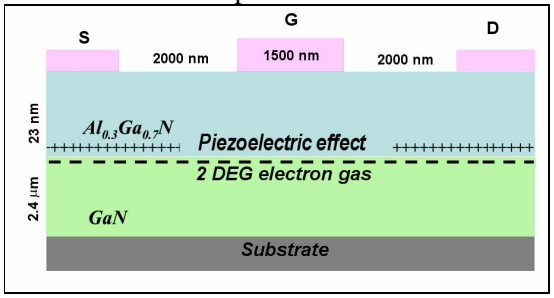

Fig. 3.7: Schematic representation of the simulated device.

We have considered the "hole" model [4] which supposes donor-like traps in the Air/AlGaN interface. Traps are charged in a characteristic time by holes so to balance the negative surface charge and to determine a higher level of current. The holes are supplied by the gate contact and, according to this model, the traps charging efficiency strictly depends on their energy level. To perform these simulation we have extended the model of Sec. 3.2 by adding a time dependent charging of surface traps. Hole trapping rates have been modelled by using the following equations

$$R_{\mathrm{Et}}^{p} = v_{\mathrm{th}}^{p}\sigma_{p}N_{\mathrm{Et}}\left[pf_{n} - \frac{p_1}{g_p}(1-f_n)\right]$$

with

$$p_1 = n_{\mathrm{i,eff}}\exp(-E_{\mathrm{t}}/k_{\mathrm{B}}T)$$

Here, E_t is a trap energy, N_{Et} the trap density p is the free hole concentrations, v_{th} is the hole thermal velocity, σ is the hole capture cross section, f_n the electron distribution (f_p=1-f_n), g_p the trap degeneration, and T is the lattice temperature. We calculated $I_D(t)$ turn-on transients (V_{GS} stepped from -10V to 0V in 10^{-8} seconds, at V_{DS}=5V) for several values of the energy level, E_T, of surface traps, to study how the transient current is affected. Donor-like traps with a density $N_{Et} = 1.0^{+13}\ cm^{-2}$ are positioned in the un-gated surface between source and gate and between drain and gate, they are assumed to have a cross section of $\sigma = 10^{-15}\ cm^{-2}$. The electron mobility is μ=800 $cm^2/(Vs)$.

The results of Fig. 3.8 show, for the case of a trap level located at E_T=0.3 eV above the valence band, a first I_D step taking place during the 10^{-8} s rise time of V_{GS}, then a first plateau value, induced by the trap delay, and finally I_D rises to its final DC value.

By increasing the trap energy level from 0.3 eV to 0.6 eV from the valence band, the hole capture rate is reduced, leading to a longer value of the trap delay, while the final I_D value is unaffected. For (E_T-E_V) > 0.6 eV, trap delay is longer than 1 s. As energy level approaches midgap value, trap delay tends to infinite. From now on, increasing E_T determines an increase of the first I_D step. As E_T approaches conduction band, the traps start to act as donors; there is no delay time before the drain current reaches its DC value, which is increased with respect to the previous case.

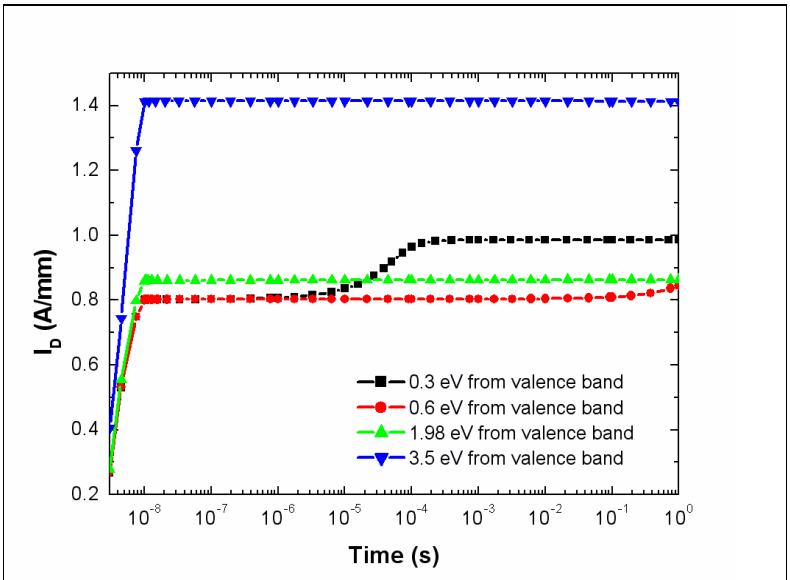

Fig 3.8: Time dependent behaviour of the drain current. The gate voltage is switched from -10V to 0V in 10^{-8} seconds and the different evolution of I_D depends on the E_T level, reported in the legend. The one which best fits experimental data is the one at 0.3 eV.

While the charge time of the traps, and so the increase of the I_{DS} current, depends on the traps concentration and on their energy level, the value of the plateau-saturation current difference depends on the ratio between n_s, the AlGaN/GaN interface charge density, and σ_{top}, the Air/AlGaN interface charge density.

3.3.2 The Acceptor model

As already stated, the "hole" model assumes the presence of donor traps very close to the valence band. However, another interpretation of the current collapse is indeed possible: we could assume acceptor-like traps in the AlGaN-air interface with an energy level around 3.8 eV from valence band, namely 0.3 eV from the conduction band. According to this alternative model, initially filled acceptor-like traps could provide electrons required to allow a time dependent increase of the drain-source current. The model simulative results strongly depends on the tunnelling through AlGaN barrier. Moreover, the application of a field dependent traps cross-section further increase the traps de-charging time. Our results demonstrate that this alternative model is reasonable, although further investigations should be made to better understand the actual effect of the tunneling process parameters on the results. In Fig. 3.9 we show the results obtained with traps having an energy level of 3.8 eV from the AlGaN valence band, which corresponds to 3.5 eV from the GaN valence band. In conclusion, our simulations indicate that beside the hole model which has been consider recently in literature [8] an "electron model" can be considered to explain experimental data. In order to distinguish between these models a more detailed experimental investigation is required in order to clearly defined the trap energy level and consequently the Gate Lag model.

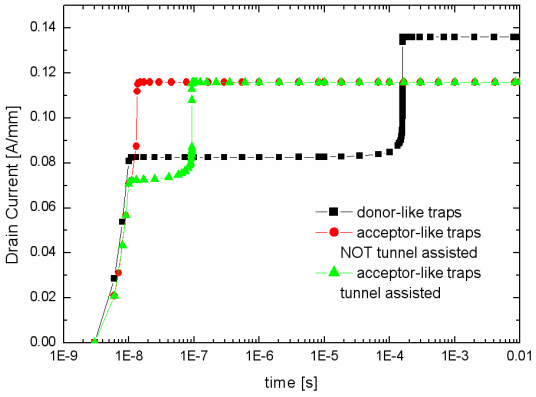

Fig 3.9: Time dependent behaviour of the drain current using donor-like traps and acceptor-like traps.

3.4 DRAIN LAG PHENOMENON

3.4.1 Physical model

The Drain Lag phenomenon has raised AlGaN/GaN HEMTs developer interest since it has important consequences on RF output power. The phenomenon can be roughly described in this way: depending on the initial applied drain voltage (drain quiescent bias point), the pulsed characteristic is higher (lower) than the DC characteristic if the final drain voltage is lower (higher) than the initial one. Surface passivation and

device annealing usually do not get any valuable results on device's performances: an accurate description of the physical transport phenomena involved is required in order to propose possible solutions.
Figure 3.10 shows a device structure analyzed in this study. The AlGaN layer thickness is 22 nm, while the GaN buffer is 2.5 µm thick. A 0.2 µm "T" shaped gate is placed at 1 µm distance from the source. The top part of the gate is 1 µm long and it is placed over 200 nm SiN passivation layer. The total drain-source distance is 6 µm. In order to introduce in Sec. 3.4.4 traps related to contacts we define two new *"contact regions"* which extends up to 0.1 µm towards the Gate from the source and drain contacts edges, their thickness is of 500 nm.

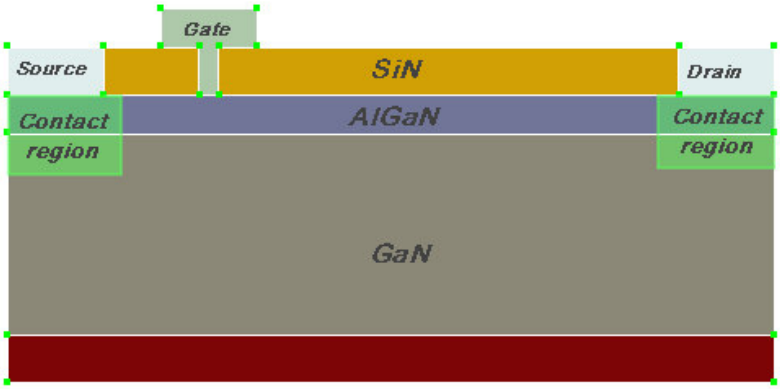

Figure 3.10: schematic view of the simulated set of devices.

In order to address the relation between current collapse and localisation of traps, their energy, and their occupation dynamics we first studied their occupation depending on the trap type (acceptor or donor) and their different placement for 0, 10 V and 20 V drain voltages, for V_{GS} =0V. The electron and hole capture cross sections for the donor and for the acceptor like traps has been set to 10^{-15} cm^2. Here, the deep-donor density N_D and the deep-acceptor density N_A are typically set to $5 \cdot 10^{17}$ cm^{-3}.
Basic equations to be solved are Poisson's equation including deep-level terms, continuity equations for electrons and holes which include carrier loss rates via the deep levels, and rate equations for the deep levels which is usually obtained within the ISE-TCAD simulation environment with a proper tuning of the models . The alternative framework, where traps formation is due to the contacts metallization, will be treated separately in the last paragraph of this section.

To compare with experimental results provided by IMEC we consider two different quiescent bias point (Q1 and Q2) for drain and gate contacts: Q1 (V_{DS}=20V, V_{GS}=-8V) and Q2 (V_{DS}=0V, V_{GS}=0).

Placing the traps in the AlGaN/SiN interface leads to time dependent results similar to those presented in Ref. [8]: the output current increase is steep and takes place at the typical traps charging time. This behaviour does not change by varying the V_{DS} as the traps occupation shows only a little dependence on the electric field.

Placing bulk traps in the AlGaN layer or in the GaN buffer leads to traps occupation and traps time charging which strongly depends on the applied voltages. In fact, for the case of traps in the AlGaN layer, all the drain quiescent bias points (V_{DS} =20,10, 0 V) induce a negative current collapse effect. This result can be explained observing that the Gate voltage strongly affect the traps occupation. Due to the fact that the traps are in the AlGaN buffer, the final positive gate voltage attracts electron, strongly affecting the traps occupation under the gate contact. Such effect dominates the whole trapping dynamics resulting in a total negative current collapse. On the contrary, GaN acceptor traps are able to reproduce negative and positive current collapse depending on the applied bias point.
In these simulations, the energy of the acceptor traps has been set to 0.3 eV from the conduction band. Small variation of this value does not produce valuable changes of the time dependent behaviour, changing almost only the occupation time (see figure 3.11). As the traps energy decrease towards the middle of the band-gap

(not shown in figure), the traps occupation is increased, but the bias dependent behaviour disappear, resulting in only positive dispersion phenomenon.

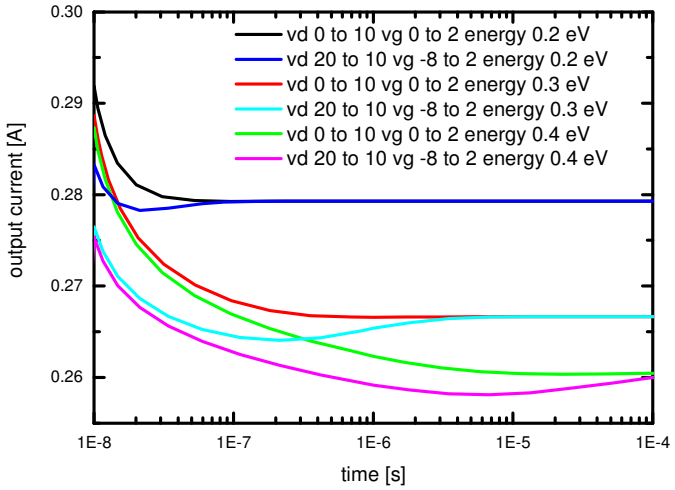

Figure 3.11: Time dependent behaviour of the drain current for different gate and drain pulses and for different traps energy for the HEMT with bulk GaN traps.

In figure 3.12 a 2-D image of the electrostatic potential inside a device for a) V_{DS} =0 and V_{GS} = 2 V, b) V_{DS} =20 V and V_{GS} = 2 V and c) V_{DS} = 20 and V_{GS} = -8 V is given. An additional 200 nm SiN layer is also placed in order to reproduce the situation device structure were field plates will be added. In figure 3.13 it is shown the traps occupation for the same applied voltages of figure 3.12. It is interesting to note what is happening for the different three cases: at V_{DS} =0 the occupation is only determined by the band bending of the AlGaN/GaN hetero-structure and the integrated value of the trapped electron is $3.6 \cdot 10^{16}$ cm^{-3}. At V_{DS} =20V and V_{GS} = 2V the high field region (gate-edge region) induces an higher trapped electron density and the integrated value of the trapped electron is now $5.14 \cdot 10^{16}$ cm^{-3}. As the gate voltage becomes negative, despite the increase of the electric field, the trapped electrons at the gate edge are reduced, due to the depleting effect of the negative applied voltage. However, due to short channel effects, the electrons starts to flow more deeply in the GaN, occupying traps far from the channels, for a total trapped electron charge of $4.4 \cdot 10^{16}$ cm^{-3}.

In conclusion we have found that the acceptor bulk traps in the GaN layer with an energy level around 0.3eV from conduction band are mainly responsible for the observed Drain lag phenomenon. The other analyzed traps (AlGaN/SiN interface, AlGaN bulk traps) do not contribute significantly to the Drain lag.
Field plates techniques can be applied to reduce the influence of trapping on drain lag. Detailed simulations however have shown that this influence is quite little and can only be appreciated for very thin passivation thickness. This is due to the type of traps involved which are bulk related and not surface related. Better control of drain lag can be obtained by using p-doped GaN buffer or by means of a back-gate.

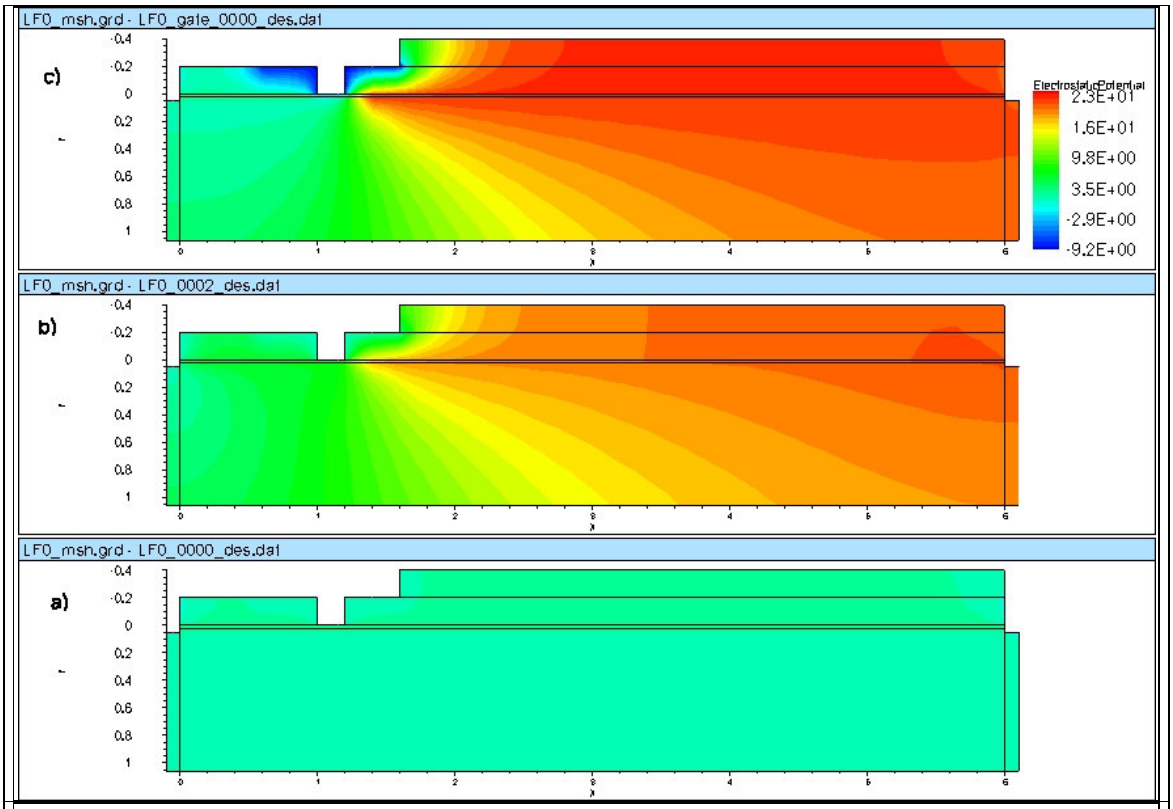

Figure 3.12: the electrostatic potential inside a device without field plate for V_{DS}=0 V_{GS} =2V (panel a), V_{DS}=20V V_{GS} =2V (panel b), V_{DS}=20V V_{GS} =-8V (panel c).

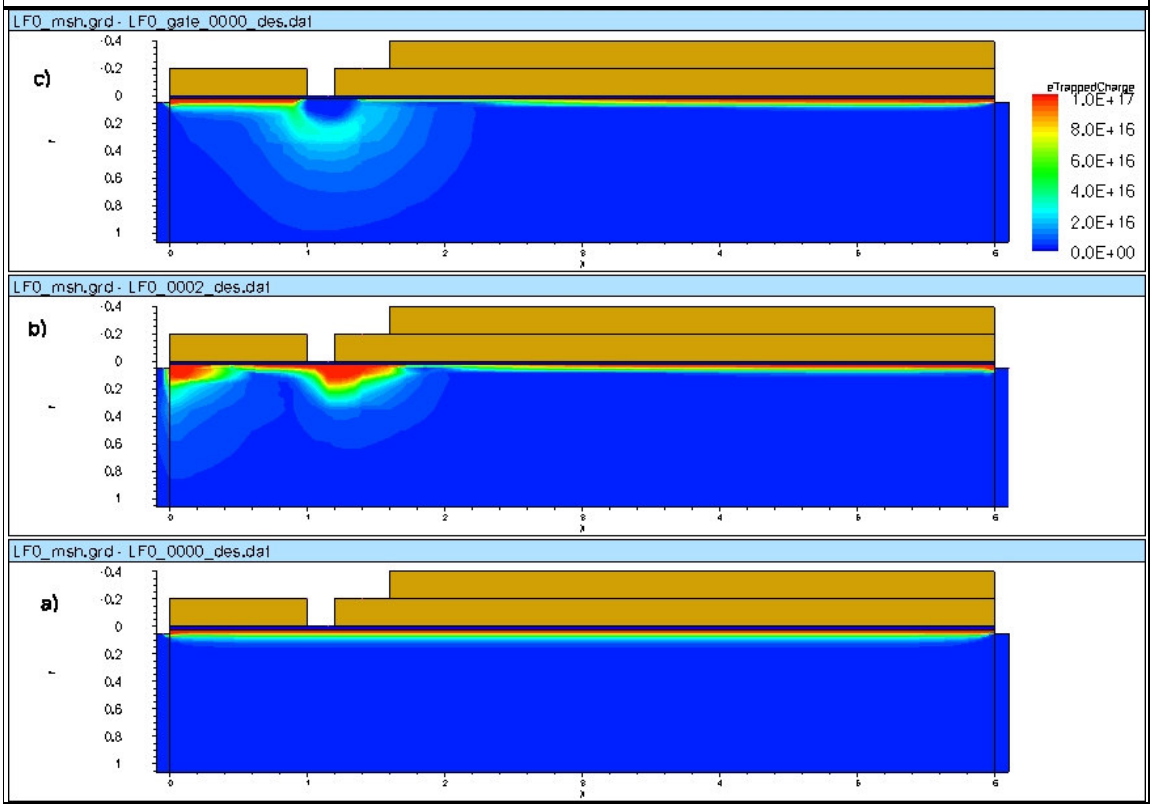

Figure 3.13: traps occupation for the same applied voltages of figure 3.12

3.4.3 Contact Traps

Another possible placement for traps, which can reproduce the experimentally observed behaviour of the studied HEMTs, is under the Source and Drain contacts. Such statement can be justified observing figure 3.14: in this graph, provided by IMEC, we show the experimentally observed negative and positive current dispersion for pulsed measurements (1.04 µs pulsed Gate and 1.00 µs pulsed Drain). DC characteristics (not shown in figure) are in between the two curves. The slopes of the two curves mainly differs for the on-resistance of the two devices: the calculated R_{DS} are 23.6 ohm and 37.5 ohm for the two quiescent bias points, respectively. On the contrary, I_{DSS} is similar for the two measurements. The difference in the two on-resistance appears as a good signature of the presence of traps under the contacts.

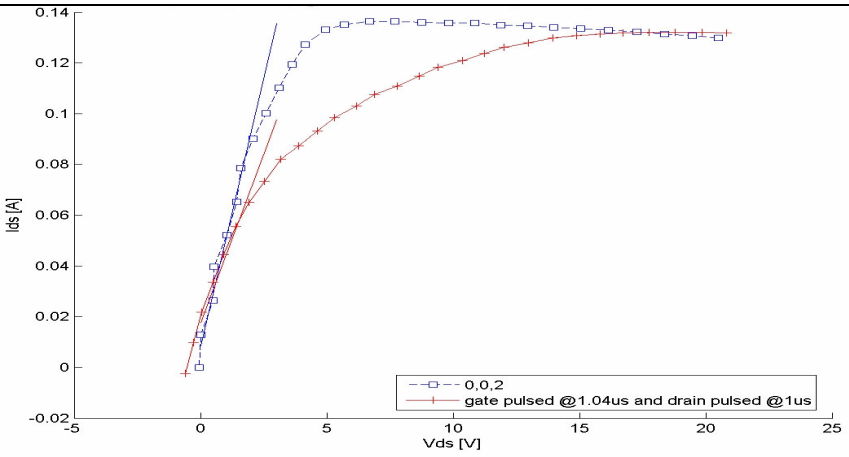

Figure 3.14: experimentally observed negative and positive current dispersion for pulsed measurements. (blue line) pulse from (V_{DS}=0, V_{GS}=0) to (V_{DS}, V_{GS}=2V); (red line) pulse from (V_{DS}=20 V, V_{GS}=-8 V) to (V_{DS}, V_{GS}=2V).

During the mesa process or contact metallization, the lattice will be damaged, producing a large amount of traps in the AlGaN layer under the contacts and in the first few layers of GaN. Such traps are then occupied as the drain voltage grows up and the electrons under the contact will get a sufficient energy to overcome the hetero-barrier. The trapped electrons either deplete the adjacent region, creating an electrostatic barrier for conducting electrons under the contacts, either decrease the amount of electrons under the contacts. The overall effect is an higher contacts resistance, which turns out in the graph of figure 3.15.
In order to verify this hypothesis we performed a DC simulation in which we turned on and off the traps under the contact. The obtained result is shown in figure 3.15. The effect of traps under the contact is just to add an additional on resistance, while the saturation current reaches the same final value.

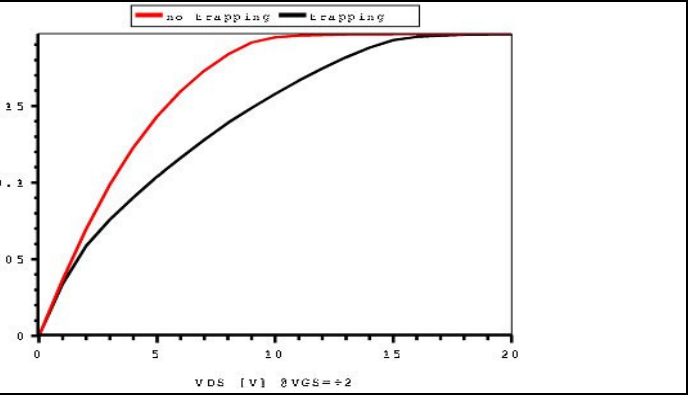

Figure 3.15: Simulated I-V characteristics with (black line) and without (red line) traps under the contacts.

3.5 REFERENCES

[1] U. K. Mishra, P. Parikh, and Y.-F. Wu, Proc. IEEE **90**, 1022 2002.
[2] S. C. Binari, P. B. Klein, and T. E. Kazior, Proc. IEEE **90**, 1048 2002.
[3] M. A. Khan, M. S. Shur, Q. C. Chen, and J. N. Kuznia, Electron. Lett. **30**, 2175 1994.
[4] P. B. Klein, J. A. Freitas, Jr., S. C. Binari, and A. E. Wickenden, Appl. Phys. Lett. **75**, 4016 1999.
[5] R. Vetury, N. Q. Zhang, S. Keller, and U. K. Mishra, IEEE Trans. Electron Devices **48**, 560 2001.
[6] G. Koley, V. Tilak, L. F. Eastman, and M. G. Spencer, IEEE Trans. Electron Devices **50**, 886 2003.
[7] T. Mizutani, Y. Ohno, M. Akita, S. Kishimoto, and K. Maezawa, IEEE Trans. Electron Devices **50**, 2015 2003.
[8] G. Meneghesso, G. Verzellesi, R. Pierobon, F. Rarnpazzo, A. Chini, U. K. Mishra, C. Canali, and E. Zanoni, IEEE Trans. Electron Devices **51**, 1554 2004.
[9] N. Braga, R. Mickevicins, R. Gaska, M. S. Shur, M. A. Khan, and G. Simin, in *Proceedings of the CSIC Symposium* IEEE, New York, 2004, p. 287.

Chapter 4

SURFACE PASSIVATION

4.1 INTRODUCTION

As previously discussed GaN-based HEMTs performances can be seriously limited by two main effects, namely the premature saturation and the current collapse which are related to surface states and traps [1],[2]. In fact, it is found that dispersion effects are reduced by SiN surface passivation [3]. Several mechanisms have been proposed to explain this result: passivation may decrease the density of deep levels, prevent electron from getting trapped at the surface, or even trap positive charge at the interface, neutralizing in this way the net negative charge at the surface.

In order to understand the effect of passivation we have developed a macroscopic model of strain in a SiN/AlGaN/GaN heterostructure which considers the free-standing nature of the system. To our knowledge, this is the first implementation of such description in a realistic device simulator.

With this model we have described the variation of the charge balance introduced by the possible additional strain induced by the SiN layer. This model has also been compared with a passivation model which has been used to describe the effect of the SiN layer in AlGaN/GaN devices in terms of a neutralization of surface states [4].

4.2 MODEL

We have developed a strain model which allows to study elastic deformations in a lattice mismatched heterostructure. The method is based on a continuous media elasticity theory. It assumes that the heterostructure layers are subjected to "chemical" forces in order to match the atomic positions at hetero-interfaces. The layers react to these forces like macroscopic samples according to the laws of elasticity theory. [5]

In order to minimize the elastic energy we introduce a finite element grid over the structure and define the vector field **u**(**r**) that stands for the grid node displacements. The mesh is built in such a way that each finite element of rectangular shape contains one material only in order to simplify discretization of the strain equation [5]. After the minimization of the strain energy the strain tensor reads:

$$\varepsilon_{ij} = \varepsilon_{ij}^{0} + \frac{1}{2}\left(\frac{\partial u_i}{\partial r_j} + \frac{\partial u_j}{\partial r_i}\right)$$

Based on the strain results, we have computed the piezoelectric polarization and, resolving self-consistent Poisson's equation, described the variation of the charge balance introduced by the additional strain induced by the SiN layer. As a result, we obtained electron sheet charge density in the channel, which was compared with experimental measurements.

The surface states passivation model has been previously used to describe the effect of the SiN layer in AlGaN/GaN devices [4]. The main point of this model is that a film of SiN can provide an amount of positive charge sufficient to neutralize the surface charge, and so to eliminate 2DEG charge depletion. We have extended it [6] to consider non-linear polarizations in GaN and AlGaN [7]; in addition the Poisson equation has been solved numerically and in a self-consistent fashion. In the following it will be referred to as Extended Cornell Model (ECM).

4.3 RESULTS AND DISCUSSION

We applied the above described strain model to study the effects of a passivating SiN layer in an AlGaN/GaN hetero-structure device. As already seen before, a passivating layer is now widely used in device fabrication, since it is found to be necessary to eliminate the unwanted effects of charges present on the HEMT's AlGaN surface between source and gate and between gate and drain. In our calculations we

model the passivation layer as a crystalline Si3N4 layer. Silicon nitride is present in nature in different crystallographic forms, such as α and β-Si3N4, the latter being the most thermodynamically stable [8, 9]. In our work, we considered β-Si3N4, which presents an hexagonal structure, and we assume a commensurate SiN/AlGaN interface, as explained previously. In this study we do not take into account dislocations, which usually reduce strain. Hence, the computed strain has to be considered as an upper limit of what is present in real devices.

We applied the simulation model to an AlGaN/GaN HEMT structure constituted by 2.4 microns of GaN, 23 nm of $Al_xGa_{1-x}N$ with x(Al) = 0.3 and a layer of SiN, placed on the surface between gate and source/drain contacts. The calculation has been performed for SiN layers with a thickness varying between 5 and 15 nm.

In Fig. 4.1(a) the structure of the passivated HEMTis shown, while in Fig. 4.1(b) we plot the results of 2D strain calculations for a 15 nm-thick SiN layer.

It can be seen that the value of lateral strain ε_{xx} in AlGaN and GaN layers is positive, since SiN induces in these two materials a tensile strain, while ε_{yy} in the same layers is negative, that is strain is compressive in the growth direction.

Sheet charge density *Ns* in the channel, obtained by integrating electron charge density along a direction normal to the gate, is shown in Fig. 4.2 for several values of SiN layer thickness. Results show that the SiN passivation determines a larger sheet charge density in the channel, in comparison to the unpassivated case ($Ns = 1.146 \cdot 10^{13}$ cm^{-2}). Besides, thicker SiN layers provide increasing value of the charge, up to $1.24 \cdot 10^{13}$ cm^{-2}. We point out that this behaviour has been found without any interface or surface charge fitting.

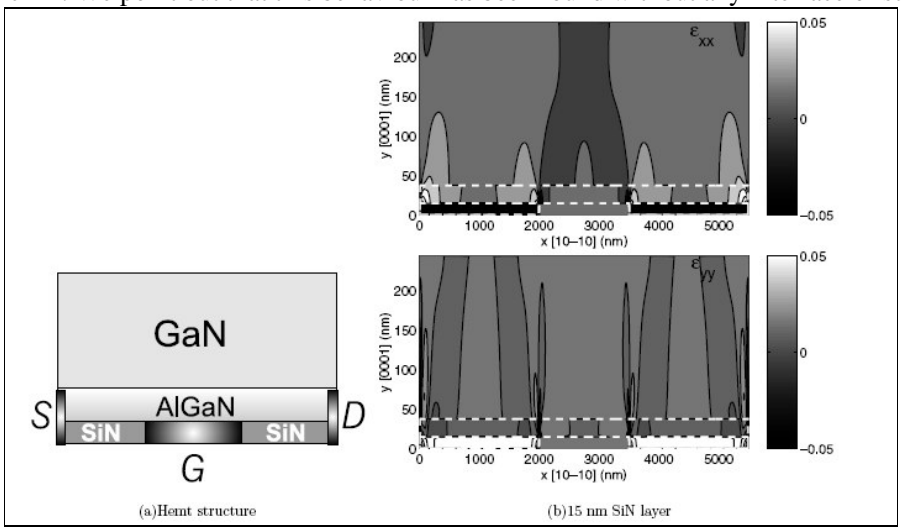

Fig. 4.1 (a) Structure of the SiN-passivated HEMT device; (b) Distribution of strain tensor components ε_{xx} and ε_{yy} in a SiN/AlGaN/GaN HEMT structure with a 15 nm-thick SiN layer: dashed white lines indicate material interfaces.

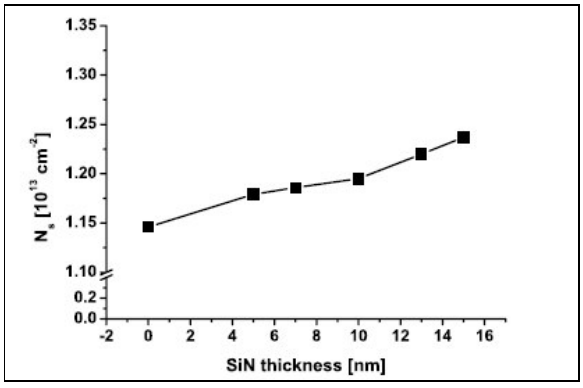

Fig. 4.2 Sheet charge density N_S for a SiN-passivated AlGaN/GaN heterostructure, as a function of SiN thickness, calculated with our strain model.

We will show now the results obtained with an alternative model, the extended Cornell model (ECM) [6]. Following the model, we placed surface and trapped (at SiN/AlGaN interface) charges of appropriate value in the SiN passivated AlGaN/GaN structure.

We calculated the value of sheet charge density in the GaN channel, as a function of the thickness of SiN layer present on the top of the structure. Silicon nitride effect on strain has been neglected in these calculations. It turns out that sheet charge density at AlGaN/GaN interface increases steadily when passivation is performed, in agreement with the analytical Cornell model [4], as soon as charge neutrality at

the SiN/AlGaN is assumed. This is due to the fact that the capacity of silicon nitride layer is now combined to that of AlGaN barrier. To quantify this point, we show in Fig. 4.3 the sheet charge density calculated with the ECM compared with results of the strain model. For the ECM we consider two situations: the first (circles) curve is related to a simulation with a surface potential which guarantees a continuous variation of the charge density in the channel. These results are comparable with strain model results. The second curve (triangles) refers to the ECM but with a different surface potential (i.e. different Fermi pinning). In this last case we observe an abrupt variation of the channel density as soon as a SiN layer is added to the device. We should point out that the pinning of the Fermi level due to the surface states of the SiN is not completely known, thus both ECM curves could represent the real situation.

A preliminary comparison with experimental data from Ref. [10] is shown in Fig. 4.4, which reports sheet charge density for three samples with the same AlGaN barrier length but with different Al composition. Calculated sheet charge densities present a correct trend, but their value are largely underestimated in both models. Interestingly, we found that one can reproduce the experimental charges, by fitting the surface potential, that is the pinning of Fermi level. In conclusion, the change of sheet charge density with SiN passivation can be reproduced with ECM with an appropriate choice of the value of surface potential ϕ_B, which pins the Fermi level at a value depending on the surface charge of SiN layer. This surface charge is related to the actual surface states present in the structure, and is in general different from what assumed in Ref.[4].

These results indicate that the main effect of the SiN passivation layer on sheet charge density is due to the change of the AlGaN surface charge [4] and to the presence of surface states, in the passivated structure, which pin the Fermi level at the surface, rather than due to additional strain induced by SiN layer.

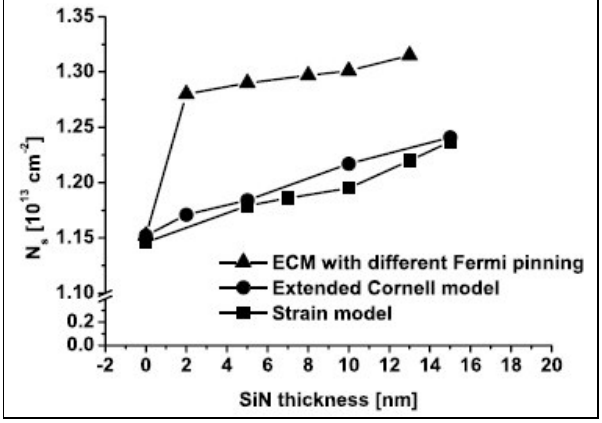

Fig. 4.3 Sheet charge density *NS* for a SiN-passivated AlGaN/GaN heterostructure, as a function of SiN thickness, calculated with our strain model (squares), and with the Extended Cornell Model [4], in two cases: with Fermi level pinning from Ref. [4] (circles) and with a different pinning (triangles).

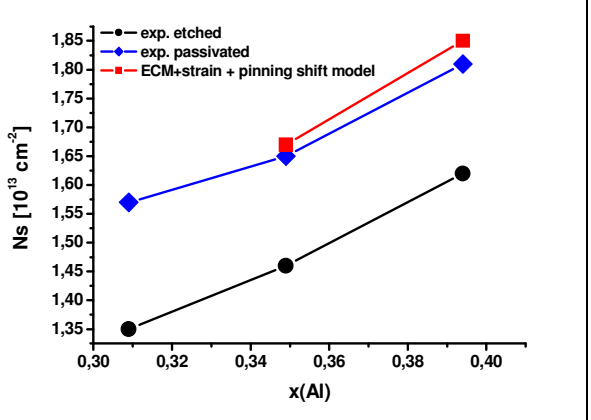

Fig. 4.4 Experimental sheet charge density for IMEC passivated and unpassivated samples [10], compared with calculated results obtained with strain model after fitting of surface potential with ECM (squares).

5.5 REFERENCES

[1] Daumiller, I., Theron, D., Gaquiere, C., Vescan, A., Dietrich, R., Wieszt, A., Leier, H., Vetury, R., Mishra, U.K., Smorchkova, I.P., Keller, S., Nguyen, C., Kohn, E.: Current instabilities in gan-based devices. IEEE Electron Device Letters **22**, 62 (2001)

[2] Sleiman, A., Di Carlo, A., Verzellesi, G., Meneghesso, E., Zanoni, E.: Current collapse associated with surface states in gan-based hemt's theoretical/experimental investigations. In: Wachutka, G., Schrag, G. (eds.), Simulation of Semiconductor Processes and Devices. Springer Verlag, Wien (2004)

[3] Green, B.M., Chu, K.K., Chumbes, E.M., Smart, J.A., Shealy, J.R., Eastman, L.F.: The effect of surface passivation on the microwave characteristics of undoped algan-gan hemts. IEEE Electron Device Letters **21**, 268 (2000).

[4] Shealty, J.R., Prunty, T.R., Chumbes, E.M., Ridley, B.K.: Journal of Crystal Growth **250**, 7 (2003).
[5] M. Povolotskyi and A. Di Carlo, "Elasticity theory of pseudomorphic heterostructures grown on substrates of arbitrary thickness", J. Appl. Phys. **100**, 063514 (2006).
[6] F. Sacconi, M. Povolotskyi and A. Di Carlo "Strain effects in SiN-passivated GaN-based HEMT devices" J. Computational Electronics 5, 115 (2006).
[7] Fiorentini, V., Bernardini, F., Ambacher, O.: Applied Physics Letters **80**, 1204 (2002).
[8] Xu, Y.-N., Ching, W.Y.: Physical Review B **51**, 17379 (1995).
[9] Cook, T.E., Fulton, C.C., Mecouch, W.J., Davis, R.F., Lugovsky, G., Nemanich, R.J.: Journal of Applied Physics **94**, 3949 (2003).
[10] Derluyn, J., Boeykens, S., Cheng, K., Vandersmissen, R., Das, J., Ruythooren, W., Degroote, S., Leys, M.R., Germain, M., Borghs, G.: Journal of Applied Physics **98**, 54501 (2005).

Chapter 5

Hemt Topology Influence on Device Performances

5.1 Effects Of Topology On Static Gain

In this section we will describe the techniques we found which can increase the device g_m. Such techniques include device doping and geometry variation.

5.1.1 Source Resistance Reduction

Introduction

High-performance AlGaN–GaN HEMTs on sapphire or SiC substrates have been successfully applied to microwave power devices and circuits, which is due to the excellent characteristics of GaN, namely a wide bandgap, a high electrical breakdown field, and a high saturation velocity. However, because of the low mobility and wide bandgap characteristics of undoped AlGaN layers, the conventional approach of AlGaN–GaN HEMTs is limiting the device performance especially for microwave power applications; moreover the shape of the potential drop between contacts leads to a low electric field component along the channel in the Source to Gate region, limiting the electronic injection. In order to reduce the source access resistance, different solutions can be applied: the following analysis we will mainly focus on the source-gate scaling.

Source to Gate distance reduction

A way to reduce the source access resistance and increase the electron injection is to reduce the Source to Gate distance.

In order to accomplish our study, we chose a typical AlGaN/GaN HEMT structure, whose schematic cross section of the simulated devices is given in Fig. 5.1.

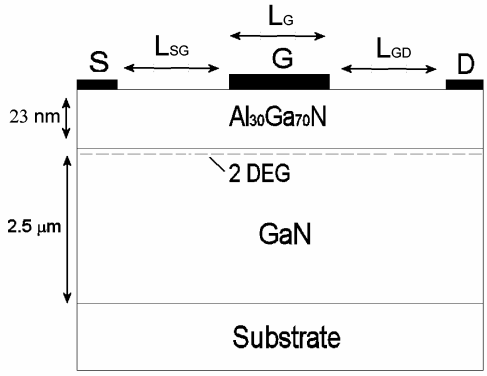

Fig. 5.1 Schematic representation of the cross section of simulated devices. The distances L_{SG}, L_G, L_{GD} which will be varied during simulations are also shown.

The AlGaN/GaN HEMT layer structures have a 2.5 μm GaN buffer and a 23 nm $Al_{0.3}Ga_{0.7}N$ barrier. The interface charge induced by piezoelectric and spontaneous polarization at the AlGaN/GaN hetero-interface, σ_i, has been set to 0.9×10^{13} cm^{-2} . We set the values of polarization charges densities of $\sigma_{Top}=-0.6\times10^{13}$ cm^{-2} at the AlGaN/Air interface, to simulate non-passivated devices and $\sigma_{Top}=0$ cm^{-2} for passivated devices. Here we suppose, according to the Cornell model [8], that passivation eliminates surface states. A charge density value of $\sigma_{Bott}=-0.25\times10^{13}$ cm^{-2} has been introduced at the GaN/Substrate interface to include both polarization charges and trap states at the interface [9]. Devices are simulated using a our in-house developed Monte-Carlo model.

Results and discussion

The central result of this work is shown in fig. 5.2 where we plot the saturated output current (I_{DSS} @ V_{GS}=0 and V_{DS}=15V) for two sets of GaN HEMTs. In the first set of simulated devices we varied L_{SG} by keeping L_G=L_{GD}=1 μm (line+squares) while in the second set we varied L_{GD} by keeping L_{SG}=L_G=1μm (line+circles).
The effects of L_{SG} scaling is quite different with respect to L_{GD} scaling. I_{DSS} increases by reducing L_{SG} while it is almost independent from the L_{GD} scaling. This is quite anomalous and, for example, is not present in conventional GaAs HEMTs where there is no dependence of the I_{DSS} on the L_{GS} (for the range of values considered here).

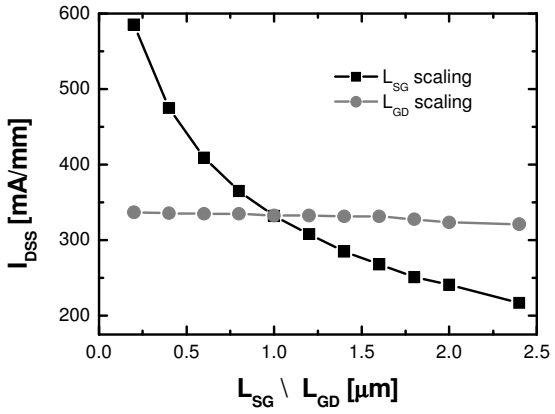

Fig. 5.2. Output current of the simulated GaN-HEMTs as a function of the S-G distance (full line, squares) and of the G-D scaling (full line, circles).

To understand the origin of this effect, which plays a crucial role in design rules of GaN HEMTs, we show in Fig. 5.3 the electric field component along the channel for the GaN-HEMT depicted in Fig. 5.1.1, with L_{SG}=L_G=L_{GD}=1μm, biased at open channel condition (V_G=0). The component of the electric field along the channel reaches its maximum (E_{GD}) at the drain end of the gate. The electric field is almost constant in the region between source and gate and presents a high discontinuity at the source end of the gate mainly due to the presence of polarization charges at the air/AlGaN interface. We will call E_{SG} the average electric field component along the channel between the source and gate contacts. In the case of Fig. 5.1.3, E_{SG} is -14.5 kV/cm while E_{GD} is -456 kV/cm. The shape of the electric field component along the channel shown in Fig. 5.1.3 is typical, with the appropriate E_{SG} and $E_{GD,}$ for all the devices simulated in this work.

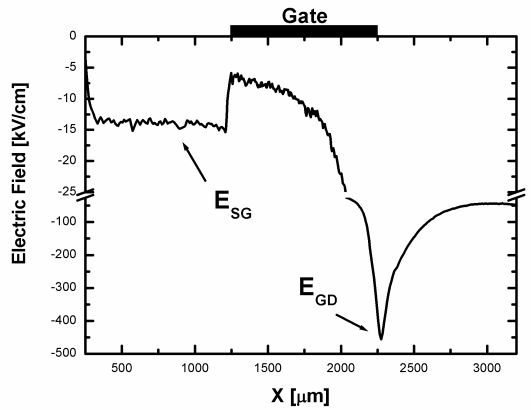

Fig. 5.3. Behaviour of the electric field component along the channel for a AlGaN/GaN HEMT with L_{SG}=L_G=L_{GD}=1μm (solid line) biased at V_{DS}= 15V V_{GS}= 0V. The electric field on the boundary of the gate

contact has been named E_{SG} and E_{GD}.

The existing relation between the electric fields defined in Fig. 5.3 and the output characteristics shown in Fig. 5.2 are pointed out in the following two sets of simulations for the unpassivated GaN HEMTs.

In the first set of simulations (L_{SG} scaling) we consider a device with L_G=L_{GD}=1.0 µm where we varied L_{SG}. In the second set of simulations (L_{GD} scaling) we consider a device with L_{SG}=L_G=1.0 µm where we varied L_{GD}. In both cases the region lengths varies in the range 0.2 to 2.4 µm. The applied voltages have been kept fixed (those of Fig. 5.3) in all the simulations. The calculated E_{SG} and E_{GD} electric field values as a function of L_{SG} and L_{GD} are reported in Fig. 5.4.

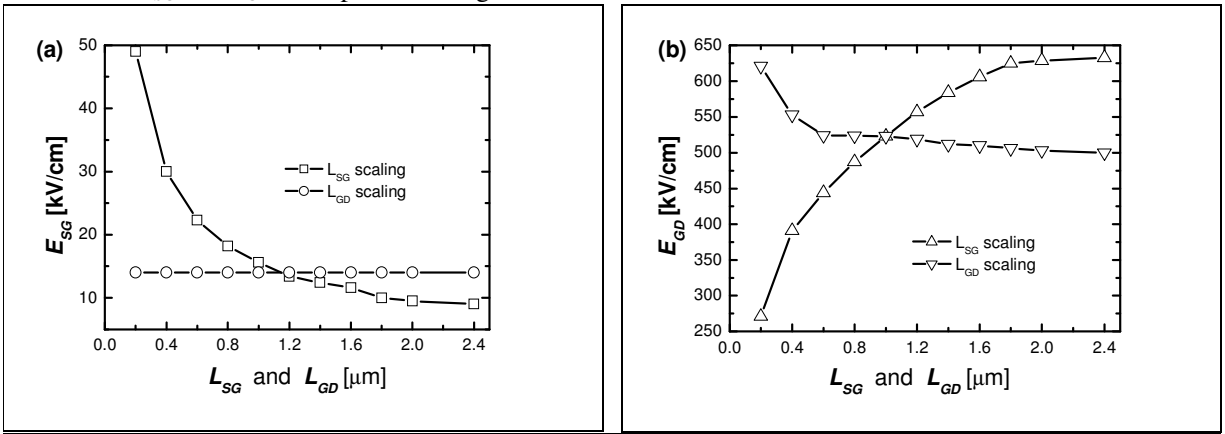

Fig 5.4. Comparison of the effect of L_{SG} and L_{GD} scaling on E_{SG} (Fig 5.1.4(a)) and E_{GD} (Fig 5.1.4(b)) for the datasets A-1 and A-2. The AlGaN/GaN HEMT are all biased at V_{DS}= 15V V_{GS}= 0V.

The figure clearly shows a marked difference between the L_{SG} scaling and the L_{GD} scaling. For the L_{GD} scaling, the value of E_{SG} remains constant, while the peak value E_{GD} increases when the L_{GD} is reduced. For L_{SG} scaling the value of E_{SG} increases by reducing the distance, while E_{GD} shows the opposite behaviour. The increase of the average electric field in the S-G region implies an increase of electrons velocity component along the channel. This effect is observable also at higher Drain bias (see Fig. 5.5).

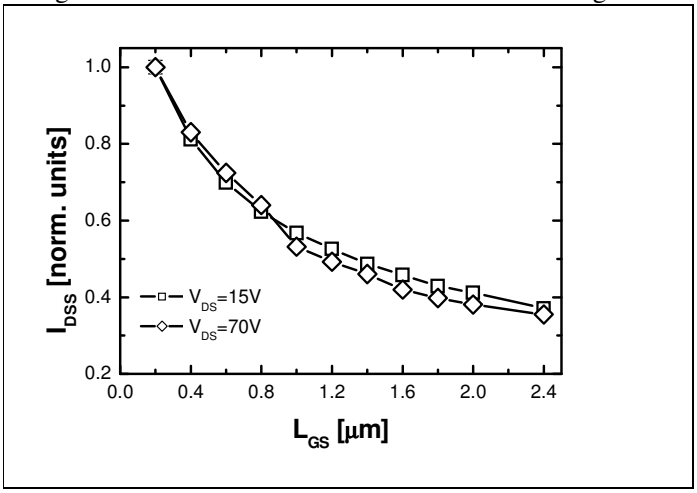

Fig. 5.5. Comparison of the output current of the simulated devices as a function of L_{SG} distance for two drain biases.

Simulation results shown in Figs. 5.4 allow us to explain the behaviour of the saturation drain current shown in Fig. 5.2. In fact, the behaviour of I_{DSS} shown in Fig. 5.2 can be understood by considering the peculiar velocity-field characteristics of the GaN where ohmic regime (electron velocity linearly dependent on the electric field) extends up to field of the order of 100 kV/cm. As shown in Fig. 5.4, for all the simulated GaN devices, E_{SG} values span in this ohmic regime. By reducing L_{SG} the component of the electric field along the channel increases and consequently the electron velocity. This result an increase of the output current. Thus, for typical GaN-HEMTs, variation of L_{SG} results in a direct variation of the channel current.

We should point out that while the electric field component along the channel decreases by increasing L_{SG}, the opposite behaviour is found for the absolute magnitude of the electric field. This effect is related to the fact that by increasing L_{SG}, the electric field component perpendicular to the channel increases, since less current is flowing in the device thus reducing the screening of the polarization charge. The downscaling of L_{SG}, has also a strong positive impact on the transconductance values. In fact, since the threshold voltage does not depend on the L_{SG}, while the output current does, the slope of the transcharacteristic (i.e. the transconductance) increases by reducing L_{SG}. Figure 5.6 shows three different transcharacteristics for L_{SG} of 0.5, 1.0 and 1.5 μm, respectively and with L_G=L_{GD}=1μm. By reducing L_{SG} the transconductance of the device increases from g_m=99 mS/mm (L_{SG} =1.5 μm) to g_m=165 mS/mm (L_{SG} =0.5 μm). The increasing of the transconductance has not, however, important effects on the cut-off frequency of the HEMT. In fact, by reducing L_{SG} we also increase the gate capacitance which balance the increase of g_m.

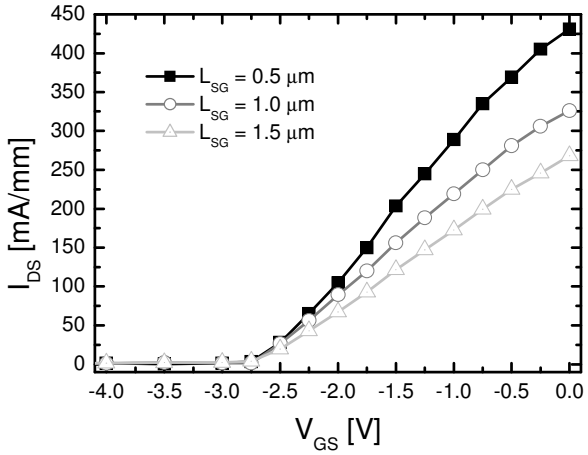

Fig. 5.6. Transcharacteristics of AlGaN/GaN HEMTs with different L_{SG}. Here V_{DS} = 15V while L_G=L_{GD}=1 μm.

We should point out that this scaling rule is valid for passivated devices and for power HEMTs as well where applied voltages are very high.

Gate Scaling

In order to understand the relation between L_{SG} scaling and L_G scaling, we performed a set of simulations where L_G is varied and L_{SG} is fixed. We repeat this set of simulations for several values of the L_{SG}. The overall result is shown in Fig. 5.7 where we plot I_{DSS} (V_G = 0 and V_{DS} = 15V) as a function of L_{SG} and L_G. In these simulations L_{GD}= 1μm. The figure shows a clear dependence of I_{DSS} on L_G, however, the increase of the current induce by L_{SG} scaling is larger with respect to the one induced by the L_G scaling. As a matter of example, by reducing L_G from 1 μm to 0.2 μm with L_{SG}=1 μm the I_{DSS} increase by 27 %. On the opposite, if we scale L_{SG} from 1μm to 0.2 μm with L_G=1 μm the I_{DSS} increase by 76 %.

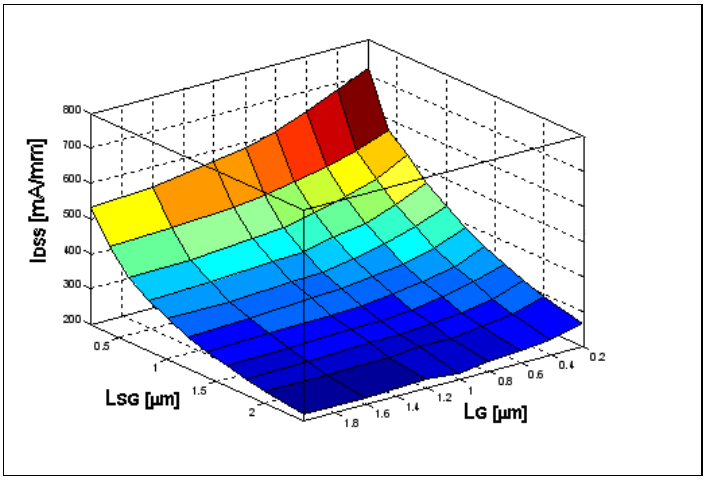

Fig. 5.7. Drain Saturation current as a function of the S-G scaling and Gate length. Here V_{DS} = 15V, V_{GS}=0V.

The scaling of the gate, however, is much more important for the cut-off frequency which increases by reducing L_G while it is almost independent on the L_{SG}.

References

[1] M. J. Manfra, N. Weimann, Y. Baeyens, P. Roux, and D. M. Tennant, "Unpassivated AlGaN/GaN HEMTs with CW power density of 3.2W/mm at 25 GHz grown by plasma-assisted MBE," Electronics Letters, vol. 39, pp. 694-695, Apr. 2003.

[2] V. Kumar, et al., "High performance 0.25 µm gate-length AlGaN/GaN HEMTs on sapphire with power density of over 4.5 W/mm at 20 GHz," Solid-State Electronics, vol. 47, n 9, pp. 1577-1580, Sep. 2003.

[3] W. Saito, M. Kuraguchi, Y. Takada, K. Tsuda I. Omura, T. Ogura, "Design optimization of high breakdown voltage AlGaN-GaN power HEMT on an insulating substrate for RONA-VB tradeoff characteristics," IEEE Transactions on Electron Devices, v 52, n 1, p 106-11, Jan. 2005.

[4] W. Saito, Y. Takada, M. Kuraguchi, K. Tsuda I. Omura, "Recessed-Gate structure approach toward normally off High-voltage AlGaN/GaN HEMT for power electronics applications" IEEE Transactions on Electron Devices, v 53, n 2, p 356-62, Feb. 2006.

[5] T. Palacios, et al., "Influence of the Dynamic Access Resistance in the gm and ft Linearity of AlGaN/GaN HEMTs," IEEE Transactions on Electron Devices, vol 52, pp 2117-2122, Oct. 2005.

[6] Blakemore, J. S., "Semiconducting and other major properties of gallium arsenide," J. Appl. Phys., vol. 53, no 10, pp. r123-r181, Oct. 1982.

[7] Gonzalez Sanchez, T., J. E. Velazquez Perez, P. M. Gutierrez Conde, and D. Pardo, "Electron transport in InP under high electric field conditions," Semicond. Sci. Technol., vol. 7, no 1, pp 31-36, Jan. 1992.

[8] J. Shealty, T. Prunty, E. Chumbes, and B. Ridley, Journal of Crystal Growth, 250, 7 (2003).

[9] A. Sleiman, A. Di Carlo, G. Verzellesi, G. Meneghesso, E. Zanoni, Proceedings of SISPAD 2004, (2004).

5.1.2 Doping of the Source-Gate region

Another possible way to enhance devices transconductance is the Source to Gate region doping. In fact, a silicon doping of the AlGaN could decrease the Source resistance, R_S. Moreover, the linearity of the device is expected to increase due to the more self aligned structure obtained by doping the access region. In our MC simulations we tried different dopings, adding donor concentrations in the AlGaN layer of 1e16 cm^{-3} (i.e. UID), 1e17 cm^{-3}, 5e17 cm^{-3}, 1e18 cm^{-3}. The layer structure is similar to that described in the previous section, with a 0.9-0.2-0.9 µm geometry. The applied Drain voltage is 15 V.

The results obtained, in terms of transcharacteristic, transconductance and electric field are shown in figures 5.8-10. From figure 5.8 and 5.9 the performance enhancements achieved by doping the S-G region are clearly visible; namely an higher output current, while keeping the threshold voltage fixed, which means an increase of the transconductance maximum.

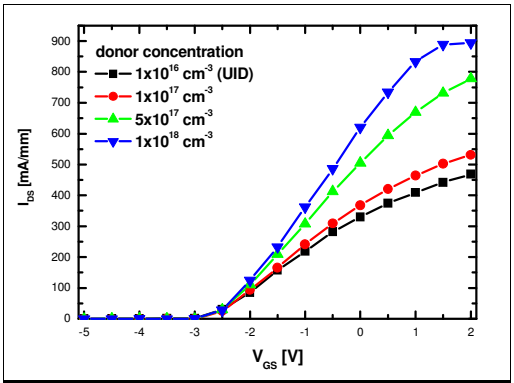

Fig. 5.8: Transcharacteristics for different devices dopings.

The current saturation for 0 V and positive Gate voltages, induced by the doping, produces a steep fall of the trans-conductance. The increased linearity of the doped devices can be evaluated considering that the device with higher doping presents a 20% variation of g_m in a V_{GS} range of 2.5 V. In the same V_{GS} range an un-doped device presents a g_m variation near 30%. Moreover the most doped device shows a g_m maximum of 260 mS/mm to be compared with 135 mS/mm for the un-doped device. In figure 5.10 we plot the electric fields (E_{SG} and E_{GD}) inside the device: both the values decrease with the increase of doping, due to the presence of the added positive centres of the donors. Such effect will, in turn, increase the breakdown threshold, since the maximum electric field in the device is reduced. Moreover, the lower electric field in the Source to Gate region will allow to get lower dynamic access resistance. However, to get the maximum effect, it is important that the doped region reaches the Gate boundary. This can be obtained by ion implantation.

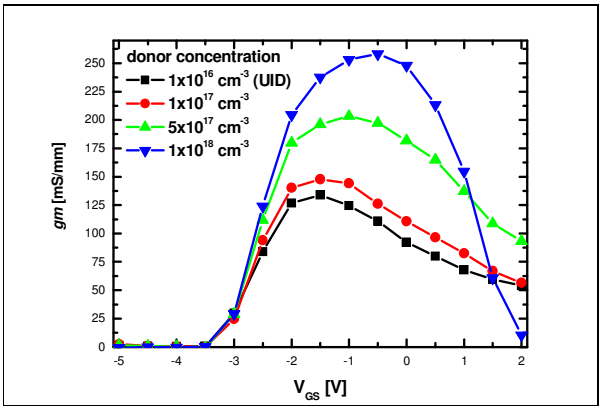

Fig. 5.9: Transconductance for different devices dopings.

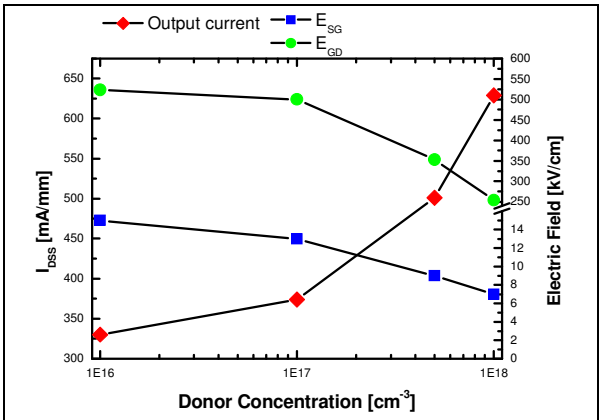

Fig. 5.10: Electric fields at the Gate boundaries for different dopings.

5.1.3 Gate Recessing

The HEMT gain could be enhanced by using recessed Gate structures. In our simulations, performed with the Drift-Diffusion techniques, we considered different depths of the Gate contact, from 2 nm to 10 nm. Due to Gate proximity to the channel, the deeper the Gate, the higher is the transconductance (see fig. 5.11 and 5.12 for the results and Fig. 5.13 for a schematic design of the device). However, it is quite interesting to observe what happens if a Gate contact not parallel to the channel is used, whose characteristics have been labelled "10 nm recessed Gate Tri" in fig. 5.11 and 5.12. In fig. 5.14 the geometry of the device is shown: the depth of the Gate varies linearly from -10 nm to 0 nm. Such a geometry is able to smooth the shape of the electric field, leading to the gain advantages offered by the field plate technique. In fact, the Gate threshold voltage increases (fig. 5.11), while the output current is almost unchanged: this implies an increase of the maximum transconductance with respect to the other devices whose Gate contact is parallel to the channel. Such solution has been also recently proposed by Nagoya University group [1].

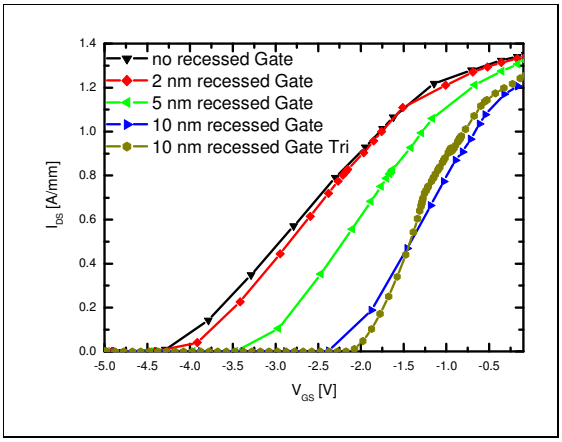

Fig. 5.11: Transcharacteristics for different Gate recess depths.

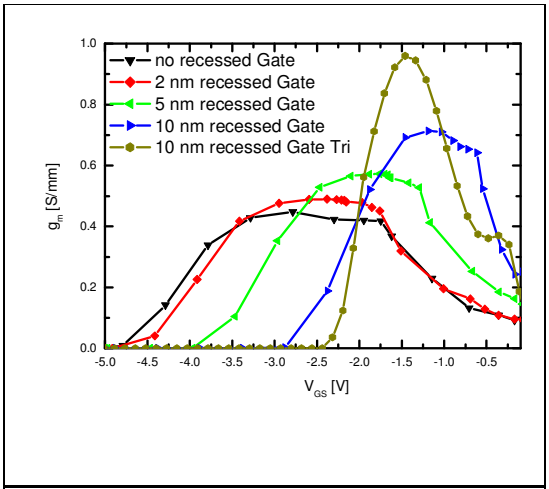

Fig. 5.12: Transconductance for different Gate recess depths.

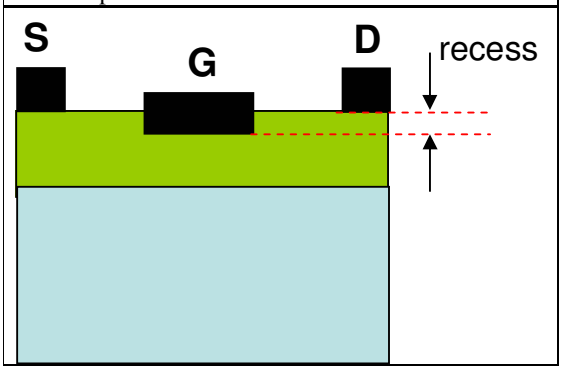

Fig. 5.13: Schematic picture of the HEMT with the Gate recess. Here S-G = G-D = 0.8 µm while the Gate length is 0.2 µm

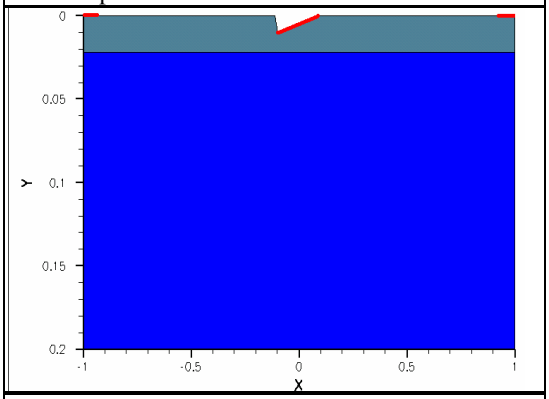

Fig. 5.14: Device geometry of the recessed Gate non parallel to the channel. Distances are measured in µm.

References

[1] Aoi, Y. (Dept. of Quantum Eng., Nagoya Univ., Japan); Ohno, Y.; Kishimoto, S.; Maezawa, K.; Mizutani, T., "AlGaN/GaN high electron mobility transistors with inclined-gate-recess structure," *Japanese Journal of Applied Physics*, Part 1 (Regular Papers, Short Notes & Review Papers), v 45, n 4B, April 2006, p 3368-71.

5.1.4 Back contact application

The new technique (IMEC) developed to remove the substrate in AlGaN/GaN HEMTs opens a wide range of possible geometries for devices design and, moreover, it offers an unique possibility to understand the real nature and effects of the sheet of negative charge present at the GaN-substrate interface, i.e. σ_{Bott}. In fact, the laser lift-off procedure allows us to remove the substrate and to vary the depth of the GaN buffer and, using it as a parameter, to design devices with better performances: such variations and possible better performances depends on what happen to the new interface between GaN and air. In fact, the lift-off procedure may have substantial effect on the σ_{Bott} value by creating new lattice defects or removing them. For this reason, in our set of simulations, by varying the depth of the device, we kept at first the value of σ_{Bott} fixed, then we reduced its value reducing the depth of GaN. Moreover, the substrate removal allows to introduce a back contact: its effect, as for the breakdown phenomena is concerned, could be essential for the future generation of GaN based devices.

The geometry of the simulated devices is shown in Fig. 5.14. The polarization charge, which induces the 2DEG at the heterointerface has been set to $\sigma_i=9\times10^{12}cm^{-2}$, while the low field mobility is 1700 cm^2/Vs. According to our AlGaN/GaN un-passivated model, we included a $\sigma_{top}=6\times10^{12}cm^{-2}$ for MC simulations and a $\sigma_{top}=6.5\times10^{12}cm^{-2}$ for D-D simulations.

As already stated, we have no theoretical model for the σ_{bottom} behaviour after a lift-off procedure, so that we performed two different sets of simulations: in the first one we kept its value fixed to $\sigma_{bottom}=2.5\times10^{12}cm^{-2}$, while varying the GaN thickness, in the second one we scaled down the σ_{bottom} value while reducing the GaN thickness. The first set of simulations could represent a situation where surface states and dangling bonds pin the σ_{bottom}, while the second one represents a situation where the growing of GaN on a substrate introduces defects, which, at last, turns out in a global σ_{bottom} depending on GaN thickness. The I_{DS}-V_{DS} and I_{DS}-V_{GS} characteristics are shown in Fig. 5.15 and 5.16: as can be seen in both graphs, if the lift-off procedure will not change the σ_{bottom} charge density (for example by remove defects introduced during the growth of GaN on the substrate), the output characteristics do not depends on the thickness of GaN layer (at least up to 1 µm) . However, even small decrease of the values of σ_{bottom} will produce enhanced output currents.

The bottom of the GaN layer could work as a back contact if a ohmic/Schottky contact is realized on the back. We then applied a back contact on the substrate removed surface, connecting it to the Gate contact. Before analysing the calculated results we have to point out that the presence of a back contact induce a Fermi level pinning at the interface which nullifies the surface/interface charge effect on the output current. This implies changes of the transcharacteristics slope and an increases of the output current. In figure 5.17, the direct characteristics for V_{GS}=0V at different GaN thickness are shown.

The saturation current is not strongly affected by the presence of the back-contact: till the thickness is bigger than 0.5 µm the pinning effect of the contact on the channel electric field is low; on the contrary, for thinner devices it causes a flattening of the I_{DS} for V_{DS} applied voltages higher than 5V.

This small detrimental effect on the direct characteristics turns out in high gain increase: in figure 5.18 we show the transcharacteristics for different GaN thickness and a 15V V_{DS} applied. As the 0.5 µm thickness is reached the pinch-off threshold is moved to less negative values, while the output current for positive Gate voltages is not so improved. At 0.2 µm the effectiveness of the back-gate becomes really high producing, at V_{GS}=+2V, a 300% increase in the *gm* with respect to the 2.5 µm thick device. Such change in the I_{DSS} can be explained considering that the current will flow in all the GaN bulk, due to the band flattening induced by the back contact biasing.

Moreover the effect of the back contact will be determinant if GaN acceptor traps are included in the simulation. As previously shown, the back contact will reduce the trapped electron density, reducing the Drain Lag and, as a consequence, increasing the output power.

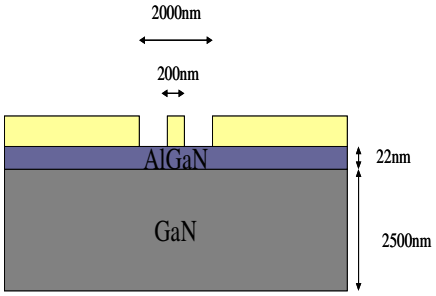

Fig. 5.14: Geometry of the simulated devices: the GaN thickness has been varied from 2.5µm to 1 µm.

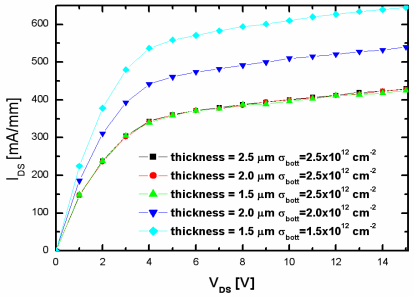

Fig. 5.15: Direct characteristic I_{DS}-V_{DS} for the substrate removed devices: a huge increment in output current is obtained as the σ_{bottom} value is reduced.

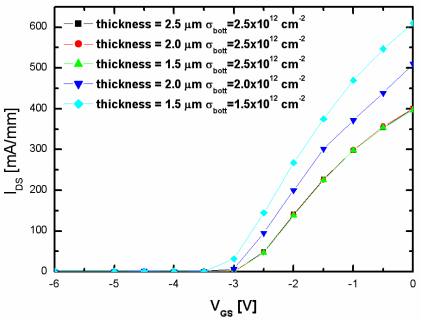

Fig. 5.16: I_{DS}-V_{GS} characteristic for the substrate removed devices.

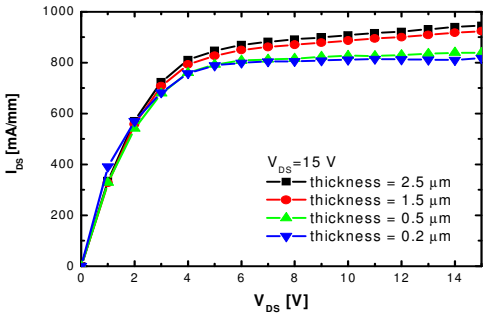

Fig. 5.17: I_{DS}-V_{DS} characteristic for the back-gated devices.

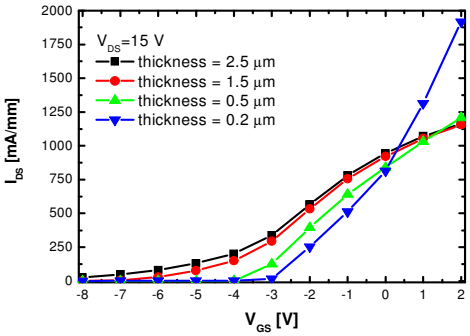

Fig. 5.18: I_{DS}-V_{GS} characteristic for the back-gated devices.

A positive and unique effect of the back contact application is the thermal management: in fig. 5.19 we show the superior performances of a device with back contact with respect to conventional substrates. Those results has been obtained solving self consistently the drift diffusion equations coupled with heat equations.
As expected, the better thermal management offered by the back contact, provides an higher output current. More in detail, the back contact has a double effect: it lowers the electric field in the channel, reducing the Joule effect, and provides an higher thermal dissipation, due to its lower thermal resistance. The negative slope of the characteristics in saturation is attributed to the decrease of the electron velocity (decrease in mobility) in the channel resulting from the increased lattice-temperature. This is consistent with the experimental result.

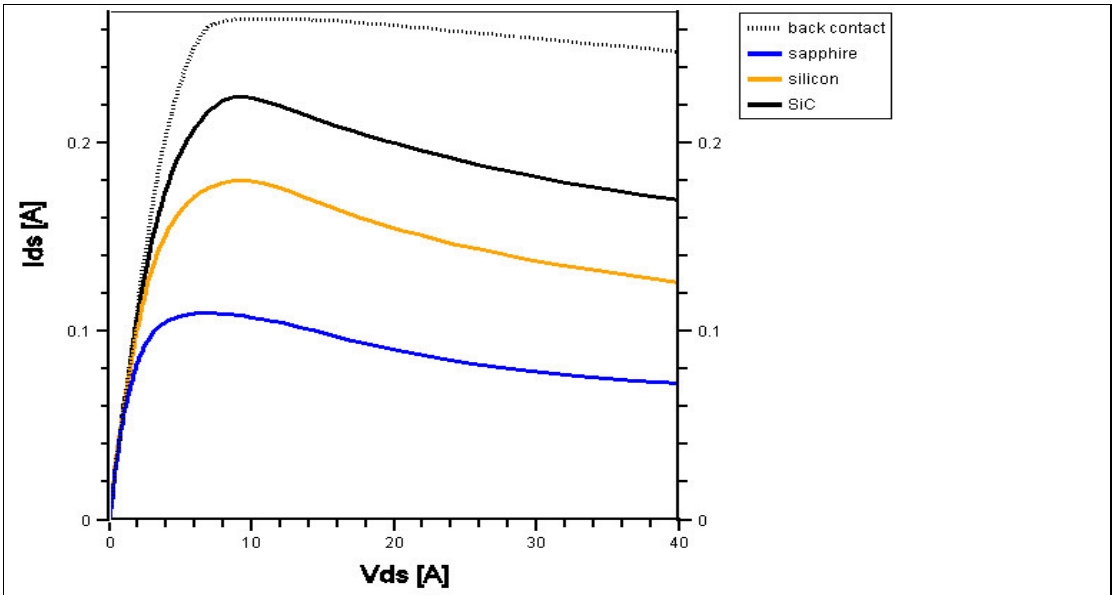

Fig. 5.19: Output current of the analysed devices.

5.1.5 Back contact application: Theoretical and Real Data

At the time this thesis is being written researches around the back contact are still ongoing. However, even if actual experimental results are limited it is possible to get a deep insight about the physics of the back contact and of the bulk GaN itself. In real devices the back current plays a determinant role, with drain current strongly depending on the back applied voltage and, up to now, to the used material physical characteristics.
In figure 5.20 the device geometry of the simulated device, whose layout is the same of the real developed device is reported.
A non intentional doping on the back contact due to the metallization has been added, this implies an increased back current due to parasitic resistance of the Schottky contact. This non intentional doping is necessary in order to reproduce the real observed behaviour. Another critical factor, as will be demonstrated with simulation, is the bulk acceptor traps density, set at **2e16 cm^{-3}**. This number is very important since it really determines the behaviour of the device (see Fig. 5.21).

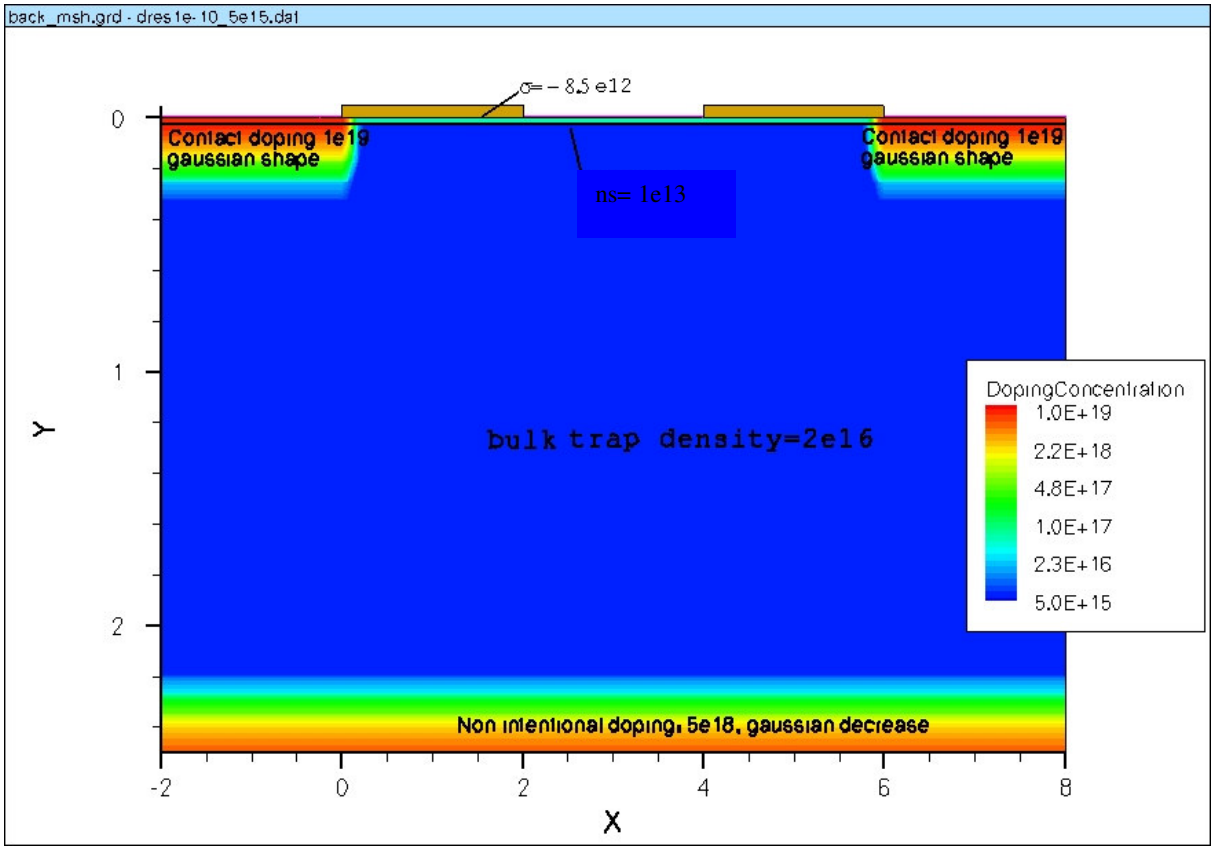

Fig 5.20: device geometry and doping

The model used for the back contact is a Schottky contact with a distribute resistance. The equation which rules the contact behaviour are the following:

$$R_d = R_\infty \exp\left(\frac{q\Phi_B}{E_0}\right)$$

$$E_0 = E_{00}\cosh\left(\frac{E_{00}}{kT}\right)$$

$$E_{00} = \frac{qh}{4\pi}\sqrt{\frac{|N|}{\varepsilon_s m_t}}$$

where:

- Φ_B is the Schottky barrier (in this model, for electrons, this is the difference between the metal work function and the electron affinity of the semiconductor; for holes, this is the difference between the valence band energy of the semiconductor and the metal work function).
- R_∞ is the Schottky resistance for an infinite doping concentration at the contact (or zero Schottky barrier).
- N is the doping concentration equal to $N_D - N_A$ at the contact
- ε_s is the semiconductor permittivity.
- m_t is the tunneling mass.
- T is the device lattice temperature

The values used in the simulations of figures 5.20 and 5.21 are the following:
R_∞ = 1.000e-11 , 1.000e-11 # [Ohm*cm^2]
Φ_B = 0.7 , 0.7 # [eV]
m_t = 0.2 , 0.2 # [1]

According to simulations, in open channel conditions V_{GS}=0, when the back contact is negative is providing current to the drain (negative value as current is "going out"). With increasing voltage of the back contact we get a double effect: from one side the difference V_D-V_{back} is less, providing less **outgoing** current (negative), on the other side the back contact is getting current from the source. When the voltage difference between source-back and drain-back is almost the same (+7.5 Vback) the back current gets a minimum.
As previously mentioned, the amount of traps plays a very important role in the determination of the device behaviour (figure 5.21): in fact the traps has to provide the correct "resistance" between ohmic contacts and back contacts so that the flowing current in open channel conditions is determined more by potential variation induced by the back contact rather than by the fact that is not perfectly Schottky and it is providing currents. On the contrary, a too high density of traps will make the back current almost 0 due to the depleting effect of the trapped electrons in the bulk (which provide higher confinement for the 2DEG).

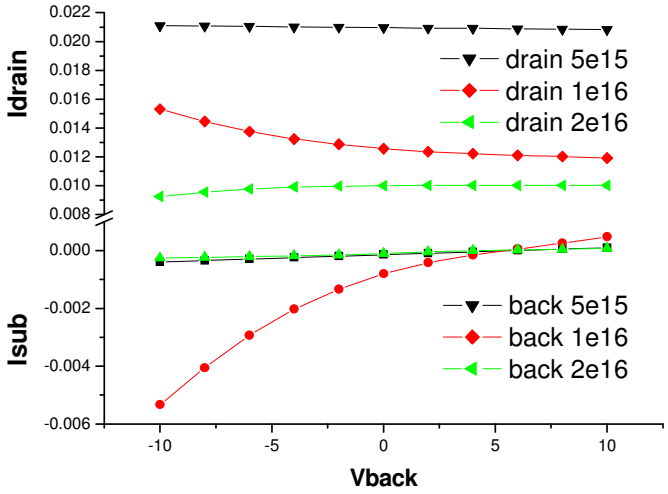

Figure 5.21: currents as function of traps density

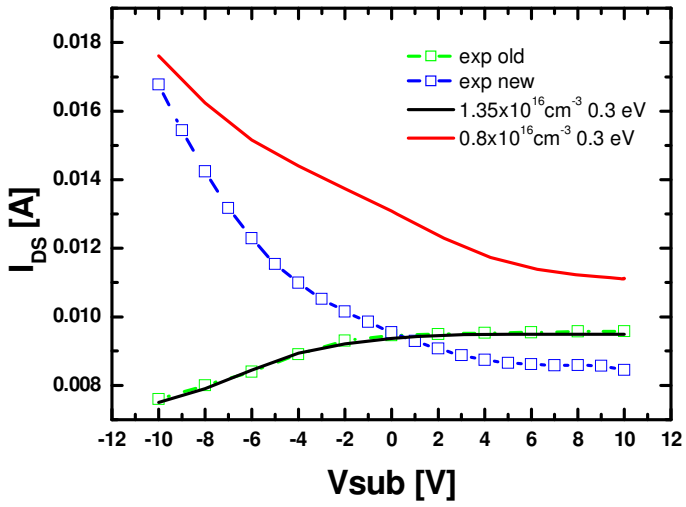

Figure 5.22: currents as function of Vsub for real and simulated device.

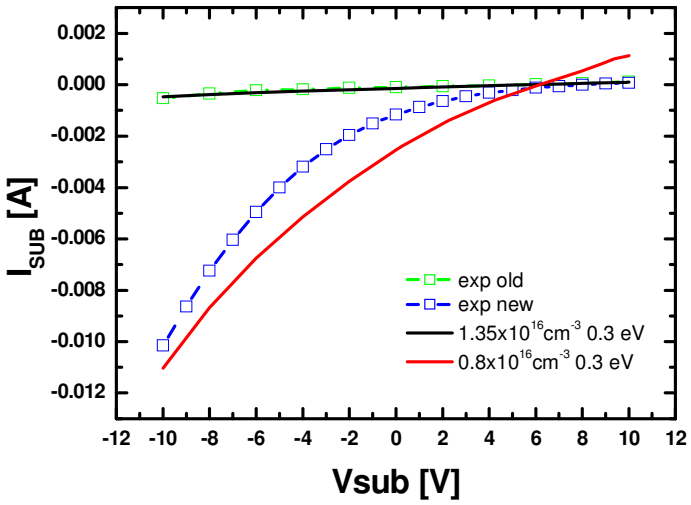

Figure 5.23: currents as function of Vsub for real and simulated device.

In figure 5.22 and 5.23 the behaviour of the real and simulated devices as a function of the applied back voltage is reported. The difference between two devices with the same layout stress the importance of the used material and developing techniques. Anyway, the very good matching obtained between simulations and real performances allows us to give a very good physical characterization of the actual GaN development.

The explanation of the observed anomalous behaviour is given in the following figures (Fig. 5.24, 5.25, 5.26).

In each image the left column represents the 1.35e16 cm^{-3} trap density bulk, while the right column is 0.8e16 cm^{-3} trap density. The top panels are biased with V_{DS}=15 V_{SUB}=-10, the middle panels are with bias V_{DS}=15 V_{SUB}=0, the bottom panels are with bias V_{DS}=15 V_{SUB}=10.

In the first image we can see the static potential, almost no difference can be observed due to different trap density. On the contrary if we look at the second image and third, e-trapped charge and current density respectively, we find big differences. Here the lower density of traps allows an higher current flow. Such difference lead to different device characteristics, with ID much more influenced on the back contact applied voltage as the material properties allows higher current flow from the back. The small differences observed in fig 5.24 are showing how the potential distribution in the device is slightly depending on the GaN properties. On the contrary the current flow is strongly depending on the acceptor traps density/energy.

According to private communications with IMEC we know that such devices are not suffering from drain lag. Our framework for simulations agrees with those experimental evidences, in fact the back contact is providing the charges which saturates traps in the bulk, thus reducing the observed current time dependence for different drain biasing.

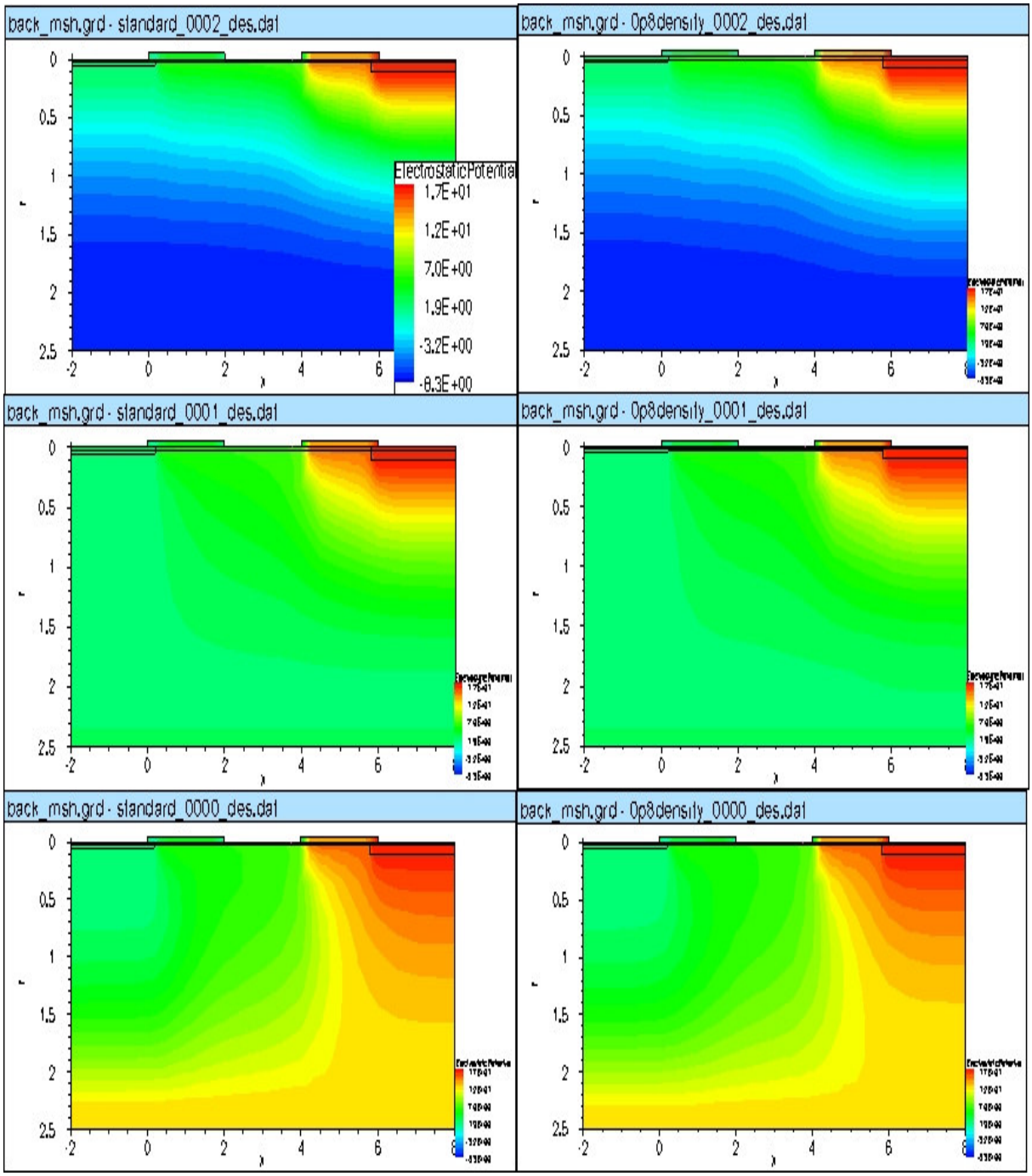

Fig. 5.24. Comparison of the electrostatic potential due to different bulk traps concentration for three contacts biasing. Left column represents the 1.35e16 cm^{-3} trap density, while the right column is 0.8e16 cm^{-3} trap density. In both cases trap energy is of 0.3 eV.

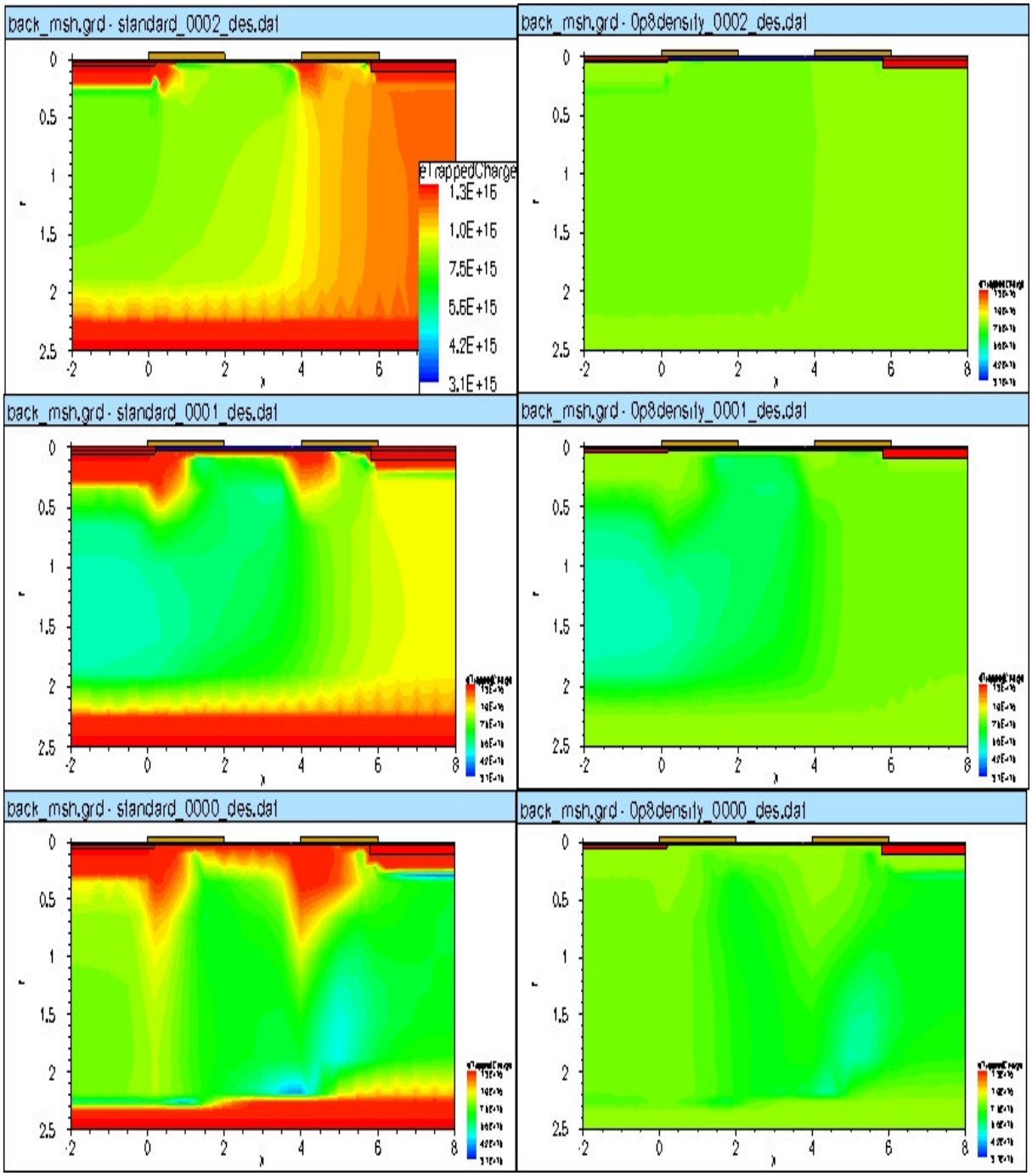

Fig. 5.25. Comparison of the electron trapped charge densities due to different bulk traps concentration for three contacts biasing. Left column represents the 1.35e16 cm^{-3} trap density, while the right column is 0.8e16 cm^{-3} trap density. In both cases trap energy is of 0.3 eV.

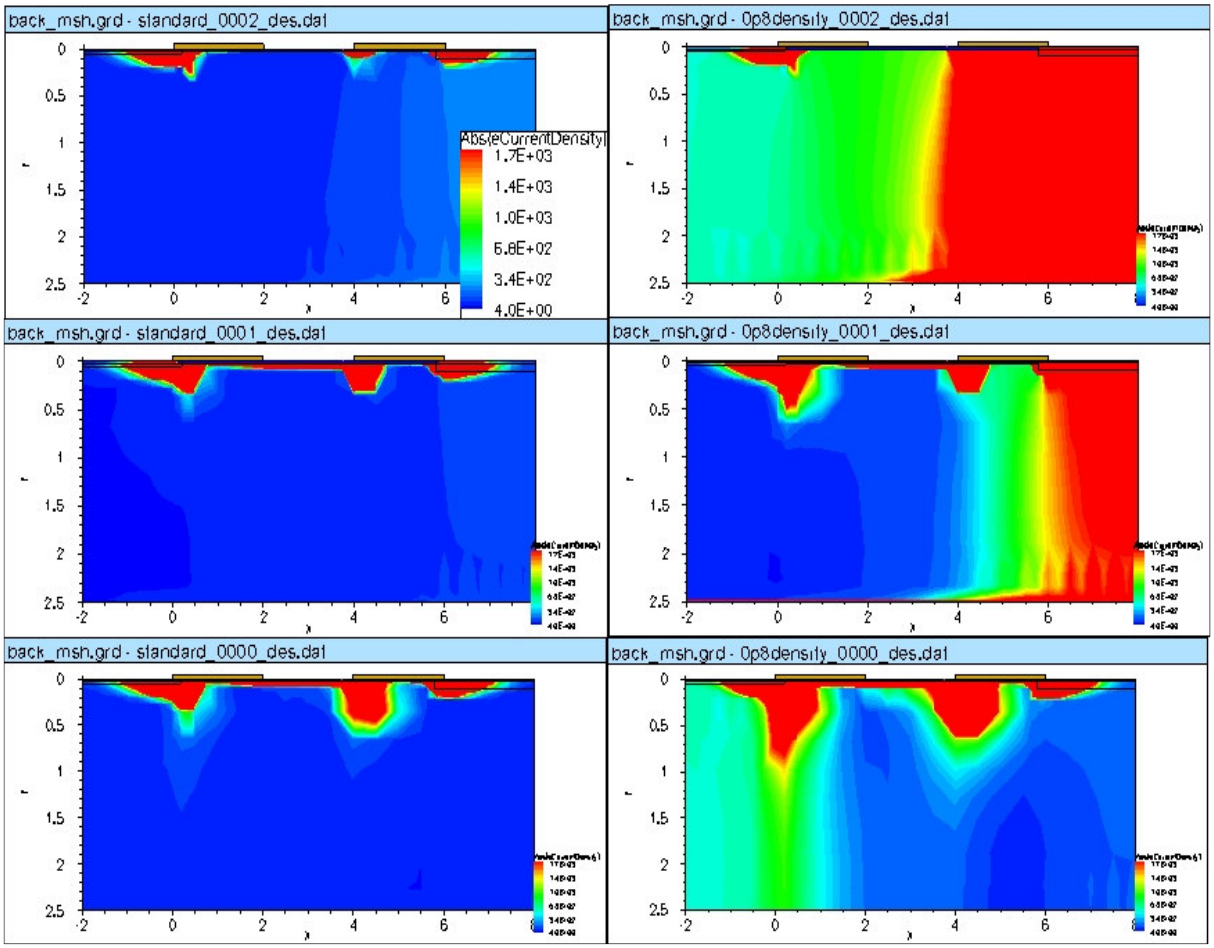

Fig. 5.26. Comparison of the absolute current density due to different bulk traps concentration for three contacts biasing. Left column represents the 1.35e16 cm^{-3} trap density, while the right column is 0.8e16 cm^{-3} trap density. In both cases trap energy is of 0.3 eV.

5.2 FREQUENCY CHARACTERISATION

In this section we will present the AC analysis we performed by means of the drift-diffusion simulator. Our study has been performed to understand the effects of the techniques presented in the previous section and by introducing a field plate (FP).

5.2.1 Gate length scaling and S-G scaling

The optimisation rules we explained in section 5.1-2 focussed on the DC behaviour of the AlGaN/GaN HEMTs. In this section we will extend our analysis to the AC domain. We simulated devices with different geometries, regarding S-G distance and Gate length, applying a Gate signal with frequencies from 10^6 to 10^{11} Hz with a DC Drain bias of 10 V. From the output characteristics we then extracted small signal parameters and the cut-off frequency.

The cut-off frequencies as a function of V_{GS} are shown in figure 5.27.

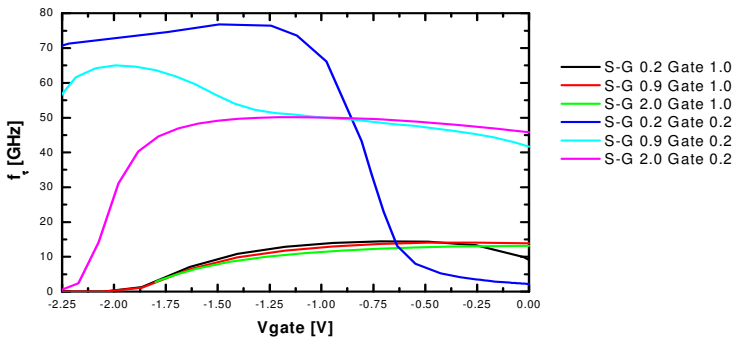

Fig. 5.27: cut-off frequencies for devices with different S-G distance and Gate length. Lengths are in micron.

The black, red and green lines represents the f_τ obtained by scaling the S-G region from 0.2 to 2.0 µm with fix gate length (= 1 µm): we notice, due to increase of the C_{GS}, the S-G distance does not highly affect the AC behaviour of the device. On the contrary a reduction of the Gate length strongly affect the HEMTs AC response: for all S-G distance simulated with 0.2 µm Gate the f_τ results highly increased. It is interesting that for the small Gate cases, the S-G distance starts to play a role for the cut-off frequency determination. In the borderline case of a 0.2 µm S-G distance there is a steep fall of the f_τ near -1V_{GS}. This effect is mainly due to the shift of the saturation of the transcharacteristic toward negative Gate voltages induced by the Gate and S-G scalings. Such saturation shifts the maximum transconductance point toward negative Gate voltages with deleterious effects on the gain at V_{GS}=0.

5.2.2 S-G doping and Gate Recessing

Device simulations were performed in the range of frequencies from 10^6 to 10^{12} Hz with a DC polarization of V_{DS} = 20 V and for several V_{GS}. From the output characteristics we then extracted small signal parameters, the cut-off frequency and the maximum operating frequency.

The cut-off frequencies and the maximum frequency as a function of V_{GS} are shown in fig. 5.28.

According to our simulation results the recessed Gate structure performance is slightly worst than the unmodified structure: the enhanced gain due to the better control on the channel charges the recessed Gate offer, is not enough to compensate the higher parasitic capacitance introduced with this technique.
On the contrary, the S-G doping has an AC response similar to that of undoped devices.

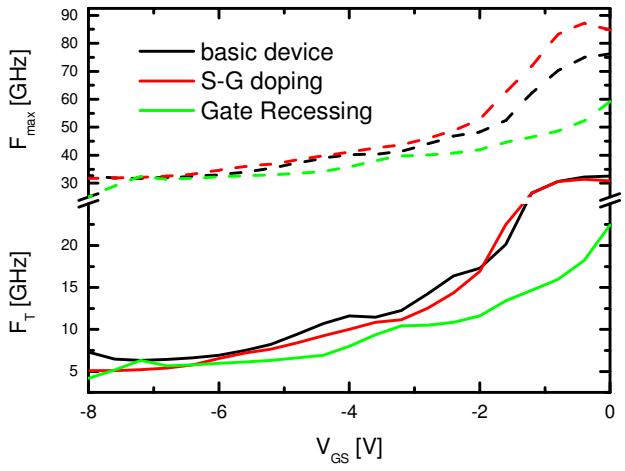

Fig. 5.28: Cut-off frequencies for the analysed devices.

5.2.3 Back contact

The application a back contact will produce an increase of the parasitic capacitance of the device, which may limit the AC response of AlGaN/GaN HEMTs. To understand the effect of the back contact and of its depth we performed AC analysis in the same way we explained in the previous section. The geometry of the device is 1.0-1.0-1.0 µm. The results, shown in fig. 5.29, panel A, indicates a lowering of the f_τ of near 15% (from 14 GHz to 11.8 GHz) at the maximum (V_{GS} ~ -0.5 V), while the distance of the back contact from the channel (i.e. thickness of the GaN) does not affect the AC response. We should consider that, in the investigated devices, the back-contact capacitance is much smaller than the gate capacitance. In the panel B of fig. 5.29 the same calculation is performed for a 0.2 µm gate device whose geometry is given in fig. 5.31. Also here the back contact is not considerably affecting the AC performances, with a maximum loss of 20%.

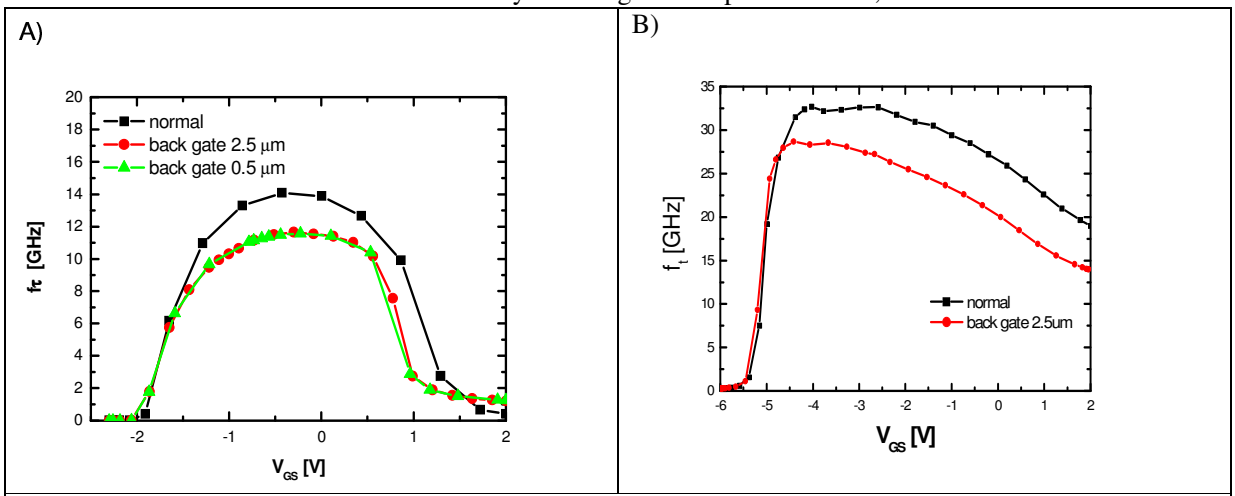

Fig. 5.29: cut-off frequencies for devices with and without back contact, for Gate lengths of 1 µm (panel A) and 0.2 µm (panel B). The thickness of the GaN is reported in the label.

In conclusion the back contact technique does not penalize the cut of frequency too heavly and only a reduction of 20% has been observed.

5.2.4 AC analysis on Field Plate structures

In fig. 5.30 we show the cut-off frequency for the FP devices whose geometry has been provided by IMEC. A schematic view of the devices is shown in Fig. 5.31.. As expected, the devices without field plate presents the best AC performances. On the contrary, the dimension of the field plate plays an important role: the device which has a 2 µm Gate connected FP, is showing a reduced f_t. The additional parasitic capacitance introduced by the FP technique also depends on the FP connection. A gate connected FP will introduce a stronger parasitic capacitance, because the voltage switching will be applied to a wider metal plate.

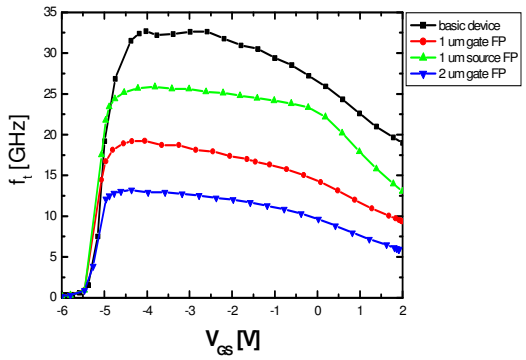

Fig. 5.30: Cut-off frequencies for the analysed devices.

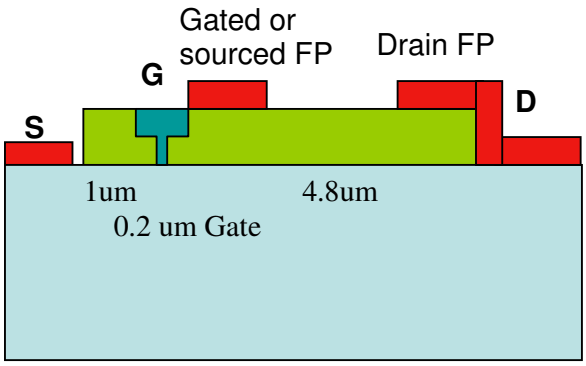

Fig. 5.31: schematic view of the simulated devices. we have 22 nm of $Al_{30}GaN$ followed by a 1 nm AlN spacer, grown on 2.5 µm thick GaN. A 200nm T gate is positioned at 1 µm from the source.

5.3 Breakdown Analysis and Optimizations

In this section we will show MC simulation results relative to the breakdown phenomenon. Having introduced new realization techniques presented in the last section it is important to study in which way improved layouts/structures can affect the breakdown threshold and the kind of breakdown (soft of hard). In this section we will analyse the high applied voltage behaviour for a HEMTs with back contacts placed at different deepness, for HEMT with a S-G scaling and, at last, HEMT with the S-G region doped. In the last paragraph a short overview of possible FP geometries is given in order to demonstrate the simulative ability to determine the best design for high power applications.

5.3.1 Application of a back contact

The use of a back contact to increase the breakdown threshold in HEMTs is not new, as it has already been presented for other III-V compound based HEMT. Its presence can prove really useful as, due to the band structure bending in the buffer, it is able to collect holes, reducing the number of particles participating to the avalanche process. However, the effect on AlGaN/GaN HEMTs of a back contact has not yet been studied. Our aim is to understand its efficiency depending on the thickness of the device and on the height of the Schottky barrier.

The AlGaN/GaN HEMTs structure is the same as presented previously (1.0-1.0-1.0) whose GaN thickness *d* has been changed to 1.5, 1.0 and 0.5 µm. The schematic cross section of the devices is given in figure 5.32.

Before analysing the calculated results we have to point out that the presence of a back contact induce a Fermi level pinning at the interface which nullifies the surface/interface charge effect on the output current. According to the framework in which the σ_{bot} charges are localised at the GaN/Substrate interface, the substrate removal and the following application of a back contact nullify the effects of the σ_{bot}. This implies changes of the transcharacteristics slope and an increases of the output current. For this reason, to understand the efficiency of the back contact, we compared the results with an ideal device with zero σ_{bot} and no back contact.

At first we applied, for all the devices, increasing V_{DS} voltages from 0 to 100V, with Gate and Back Contact voltages fixed to 0V and Schottky barriers of 1.2 eV for the gate contact and 1.0 eV for the back gate. The calculated output currents are shown in figure 5.33.

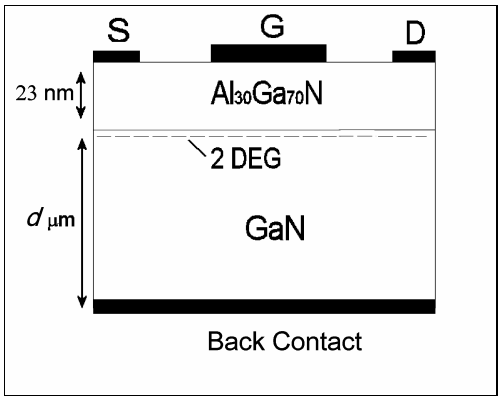

Fig. 5.31: Schematic representation of the devices cross section.

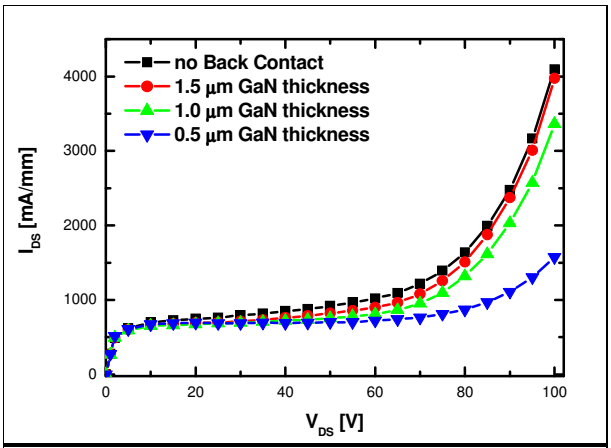

Fig. 5.33: Output current for different device depths.

The improvements in the breakdown voltage of the back contact increases by reducing the thickness of the device. A valuable effects is obtained for 0.5 µm (this limit can be reached with IMEC technology): here the breakdown voltage results increased of near 20V.

Such depth of the back contact required to inhibit the breakdown phenomenon is mainly due to: i) collection of holes which prevent the holes accumulation under the source (parasitic bipolar effect, PBE) ii) back-contact acting like a field plate (i.e. the field plate is shaped by the presence of the back contact). The 2-D maps of holes densities in the devices are shown in figure 5.34. Here the effect of the back contact as an hole collector is evident as the hole densities are quite reduced after the application of the back-contact.

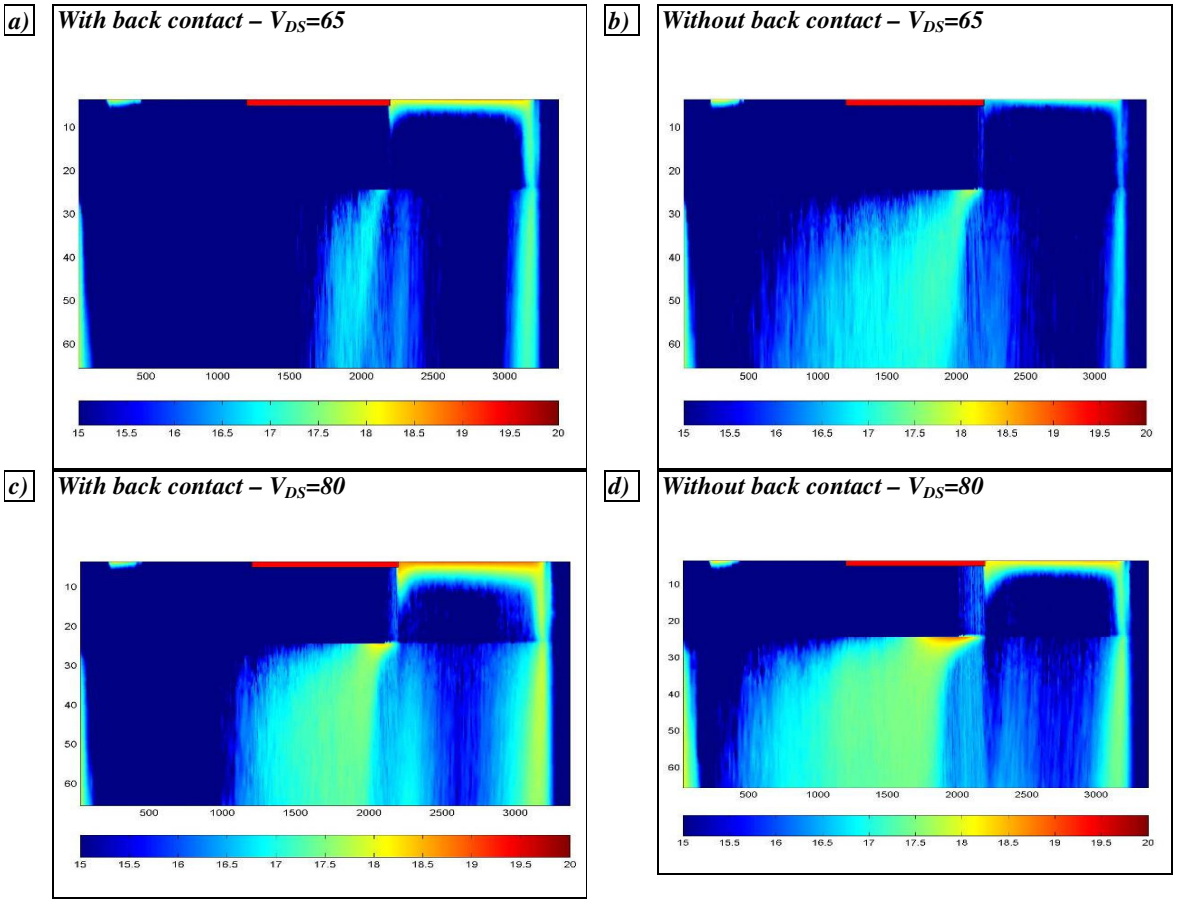

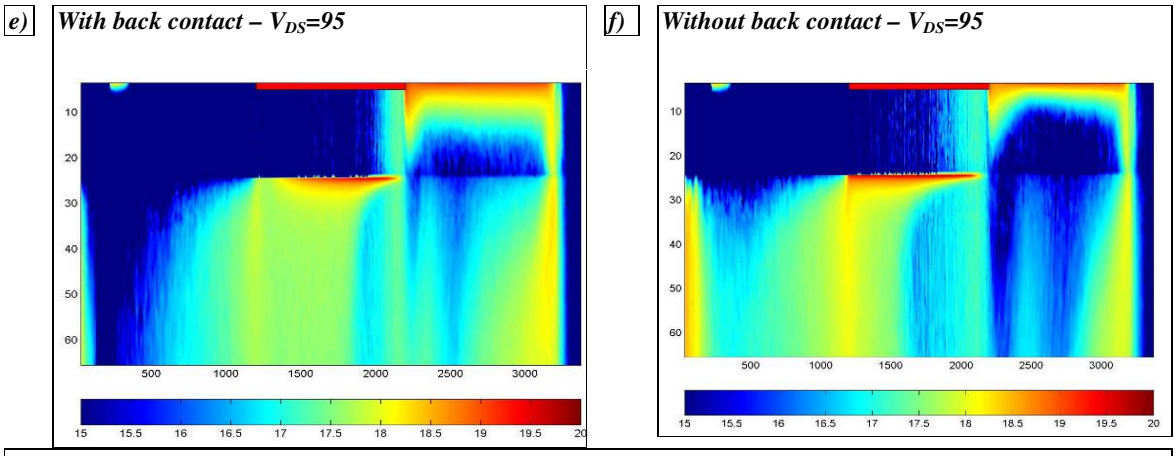

Fig. 5.34: In the left column 2-D maps of holes densities in a device with back contact and 0.5 µm on GaN; in the right column holes density in a device without back contact. Applied voltages are 65 V_{DS} for a) and b); 80 V_{DS} for c) and d); 95 V_{DS} for e) and f); V_{GS} is 0 in all cases. Spatial coordinates are measured in nm and the color scale is a log scale in cm^{-3}.

5.3.2 Effects on Breakdown of S-G Scaling , AlGaN Doping and Recessed Gate

The breakdown phenomenon and the subsequent avalanche generation are controlled mainly by two different factors, the electric field and the carrier concentration. More in details, as the electric field provides enough energy to electrons avalanche generation is initiated and the hugeness of the effect on the device will depend on the amount of carriers involved. Detailed MC simulations were performed to understand the breakdown behaviour for devices with scaled S-G distance and with doped S-G region.

In figure 5.35 we show the output current for devices with geometry $L_{GS} = x\ L_G = 1.0$ µm and $L_{GD} = 1.0$ µm (in short, *x*-1.0-1.0) with *x* equal to 0.2, 1 and 2 µm, and no additional doping. The smaller S-G distance induce a very steep increase in the output current as the avalanche is initiated (hard breakdown). This effect is mainly due to the fact that, for this small S-G distance and high applied voltages, the electric field in the S-G region becomes enough high to induce avalanche generation even there. On the contrary, with longer S-G regions, the avalanche generation occurs only at the drain end of the Gate as well as at the Drain contact. We note that reducing the S-G distance we move from a soft breakdown behaviour to a hard breakdown behaviour.

In figure 5.36 we show the output current for devices with geometry 1.0-1.0-1.0 with additional donor doping in the AlGaN barrier in the Source to Gate region with concentrations 1×10^{16} cm^{-3} cm^{-3}, 5×10^{17} cm^{-3} and 1×10^{18} cm^{-3}. There is only a small change in the threshold breakdown voltage and moreover the steepness of the curves does not increase too abruptly. This behaviour can be explained considering the lowering of the electric field induced by the additional doping centres. We also have to note that the scattering centres added by doping seems not to affect in a highly detrimental way the device performance.

Such observation suggest us the possibility to increase the breakdown threshold by correctly doping the high field regions (which may be obtain with selective ion implantation): in this way we will partly reduce the peak electric field, with positive ionized donor centres. However, we have to remark that this additional doping could affect AC behaviour due to the mobility degradation induced by doping.

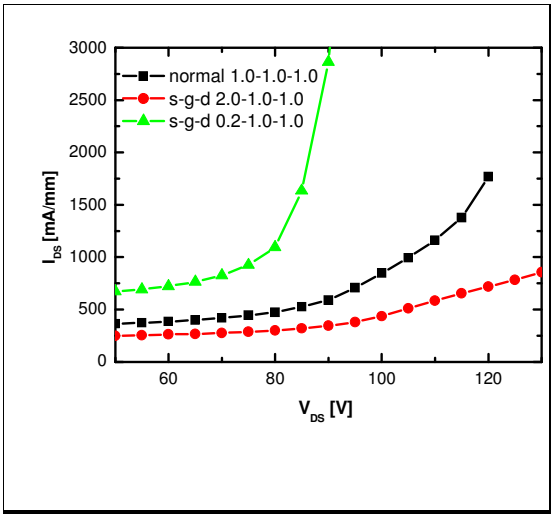

Fig. 5.35: Output current for different device geometries.

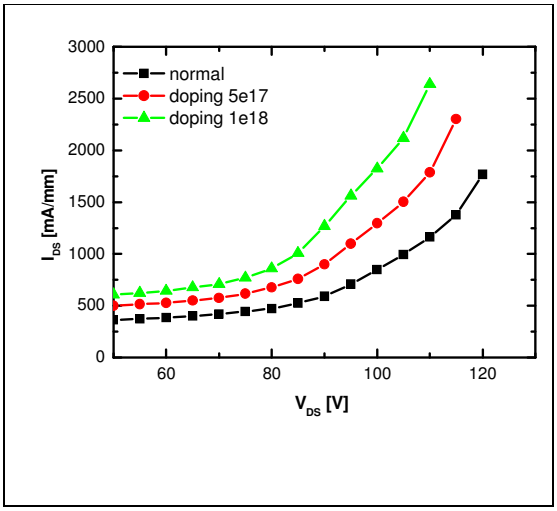

Fig. 5.36: Output current for different device dopings.

As far as the Gate recessed device is concerned, our simulation results indicates that the breakdown voltage is slightly increased using a triangular recessed gate. Such difference could be explained considering a sort of field plate effect due to the triangular shape of the recessed structure: in fact the down-slope of the gate contact from the drain edge to the gate-edge is able to smooth the electric field peak, enhancing the breakdown voltage.

5.3.3 Field plates

In this section we will show simulation results relative to the relation between field plate (FP) structures and breakdown voltage (BV). Besides the conventional FP geometries, we presented a various number of non-conventional FPs. In this document we will describe only the one actually under development at IMEC, namely the fingered FP, while only a short overview of the other geometries will be provided. The fingered FP consist of a double FP, source and drain connected, where small fingers of the FP metal penetrates in the oxide. The dimension, the depth and the spacing of the fingers can be varied in order to optimise the electric field distribution.

Conventional Field Plate geometries

The simulations we performed, whose aim is to define the optimized Field Plate geometry for a GaN based HEMT, has been accomplished by use of the ISE-TCAD simulation tool.
A sketch of the simulated devices is shown in figure 5.37: according to the IMEC technology we have 22 nm of $Al_{30}GaN$ followed by a 1 nm AlN spacer, grown on 2.5 µm thick GaN. In order to investigate the maximum BV obtainable we chose the longest S-D distance available, 8 µm. A 200nm T gate is positioned at 1 µm from the source. The carrier concentration at the heterointerface is of 1.5 10^{13} cm^{-2}. The SiN thickness is 400 nm and both gate and source connected FP structures have been considered. Moreover we consider an additional configuration where both gate and drain field plates are introduced at the same time.
The results of our simulation for such devices are reported in the table 5.1. The source connected geometry and gate connected geometries present almost the same performances, on grey the best geometry found.

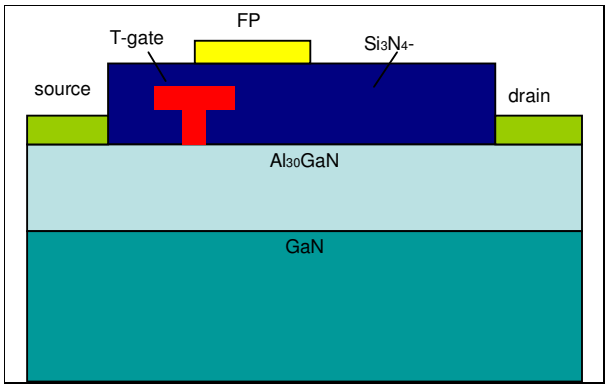

Fig. 5.37: schematic view of the simulated set of devices.

Gate connected FP	**Source connected FP**
fpgate= 0 fpdrain= 0 BV=256	fpsource= 0 fpdrain= 0 BV=256
fpgate= 0 fpdrain= 1 BV=301	fpsource= 0 fpdrain= 1 BV=301
fpgate= 0 fpdrain= 2 BV=245	fpsource= 0 fpdrain= 2 BV=245
fpgate= 1 fpdrain= 0 BV=302	fpsource= 1 fpdrain= 0 BV=296
fpgate= 1 fpdrain= 1 BV=486	fpsource= 1 fpdrain= 1 BV=482
fpgate= 1 fpdrain= 2 BV=558	**fpsource= 1 fpdrain= 2 BV=555**
fpgate= 2 fpdrain= 0 BV=297	fpsource= 2 fpdrain= 0 BV=290
fpgate= 2 fpdrain= 1 BV=513	fpsource= 2 fpdrain= 1 BV=507
fpgate= 2 fpdrain= 2 BV=493	fpsource= 2 fpdrain= 2 BV=493
fpgate= 3 fpdrain= 0 BV=286	fpsource= 3 fpdrain= 0 BV=281
fpgate= 3 fpdrain= 1 BV=493	fpsource= 3 fpdrain= 1 BV=487
fpgate= 3 fpdrain= 2 BV=449	fpsource= 3 fpdrain= 2 BV=450
fpgate= 4 fpdrain= 0 BV=242	fpsource= 4 fpdrain= 0 BV=243
fpgate= 4 fpdrain= 1 BV=420	fpsource= 4 fpdrain= 1 BV=416
fpgate= 4 fpdrain= 2 BV=266	fpsource= 4 fpdrain= 2 BV=272

Table 5.1: breakdown voltages as a function of different geometries, lengths are in micron.

From the analysis we performed some important conclusion about the FP technique can be traced:
The FP geometry (i.e. plates extension and passivation thickness) is a key factor in order to increase the device performances but a correct optimisation is needed. In fact the redistribution of the electric field in the device does not follow an easy analytic rule, since contacts dimension and shape, presence of traps (surface and bulk) and passivation material characteristics strongly influence the breakdown knee and subsequent avalanche generation intensity.
The drain connected FP is essential in order to increase the BV voltage but symmetry between drain connected and gate or source connected FP is not mandatory, on the contrary, our best result foresee not symmetrical FP.
The influence of Drain connected FP strongly depends on the contact processing technique: the not intentional doping extension and density can act as an intrinsic FP, making an additional one not useful.

Source and gate connection of the FP doesn't affect the Breakdown Threshold, but as previously shown the source one is less affecting AC behaviour.

Non Conventional Field Plate geometries

In this section we present the results relative to the fingered FP technique: two fingered field plate are connected with source and with drain respectively. Their length and the deepness of the finger are free parameters, but technology requirements impose the same depth for all the fingers. Results of the simulations are shown in the following.
To understand the behavior of this FP design we consider a device with the geometry of Fig 5.37 where L_{GD} is 13 µm. Without fingers on the FPs we find the breakdown voltages reported in Figure 5.38 as a function of the FP length and passivation thickness.
The subsequent step is to find the best configuration of the finger according to their number, depth and length. Since with the wrong configuration it is possible to even reduce the BV and the simulative work becomes really important. However, with a huge number of simulations it has been possible to find the configuration which enhances the BV up to 1710 V: it consist of 4 fingers on 3 µm field plate, extending for 0.2 µm in the passivating layer, whose total depth is 0.4 µm. In Figure 5.39 the electrostatic potential at 4000VDS is shown for the best device geometry.

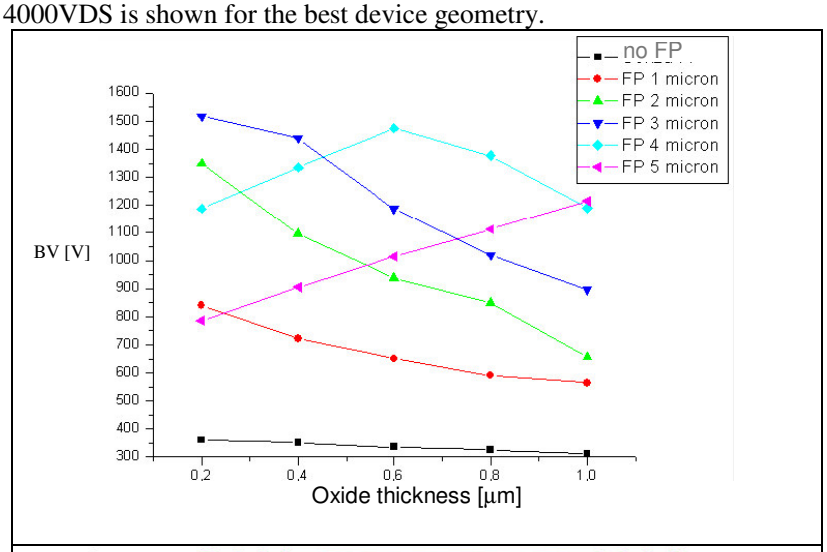

Fig. 5.38: Breakdown voltages of the un-fingered devices as a function of FP length and passivation thickness.

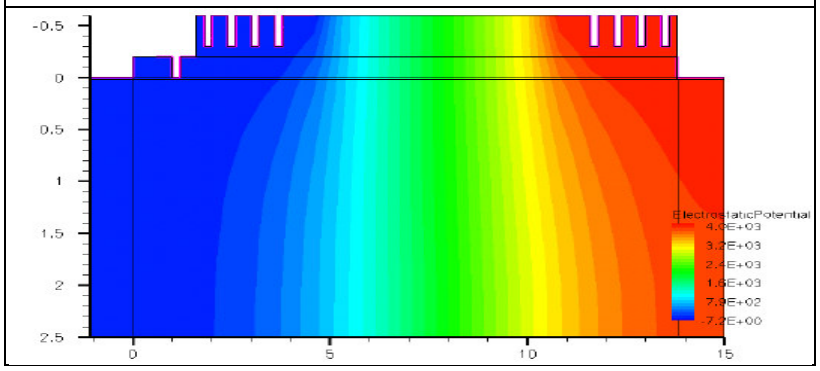

Fig. 5.39: electrostatic potential at V_{DS} = 4000 V for a four fingers FP. The fingered FP can enable a better spreading of the electric field along the channel.

Non Conventional Field Plate geometries: an overview

Non Conventional Field Plate geometries
triple FP

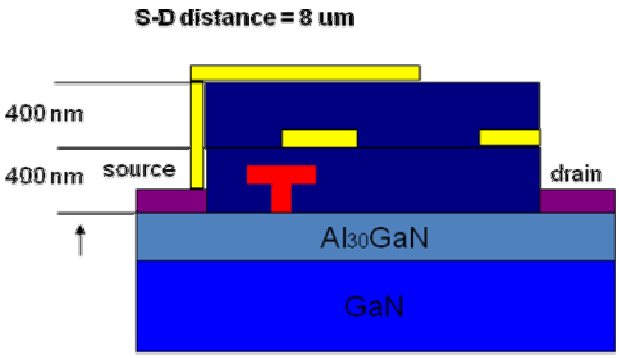

k= 1	fpgate= 0	fpdrain= 0	fpsource= 0	BV=	256
k= 2	fpgate= 0	fpdrain= 0	fpsource= 3	BV=	275.8391
k= 3	fpgate= 0	fpdrain= 0	fpsource= 6	BV=	162.6918
k= 5	fpgate= 0	fpdrain= 1	fpsource= 0	BV=	301
k= 6	fpgate= 0	fpdrain= 1	fpsource= 3	BV=	510.6423
k= 7	fpgate= 0	fpdrain= 1	fpsource= 6	BV=	299.7416
k= 8	fpgate= 0	fpdrain= 1	fpsource= 9	BV=	327.9099
k= 9	fpgate= 0	fpdrain= 2	fpsource= 0	BV=	245.2261
k= 10	fpgate= 0	fpdrain= 2	fpsource= 3	BV=	495.9284
k= 11	fpgate= 0	fpdrain= 2	fpsource= 6	BV=	316.8546
k= 12	fpgate= 0	fpdrain= 2	fpsource= 9	BV=	349.0723
k= 14	fpgate= 1	fpdrain= 0	fpsource= 3	BV=	279.7210
k= 15	fpgate= 1	fpdrain= 0	fpsource= 6	BV=	145.4326
k= 17	fpgate= 1	fpdrain= 1	fpsource= 0	BV=	521.5189
k= 18	fpgate= 1	fpdrain= 1	fpsource= 3	BV=	516.0831

Non Conventional Field Plate geometries multipad FP

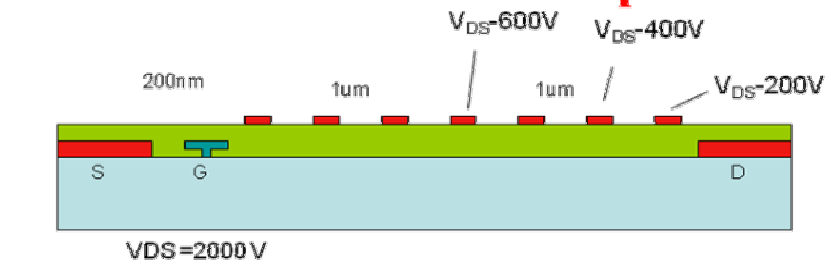

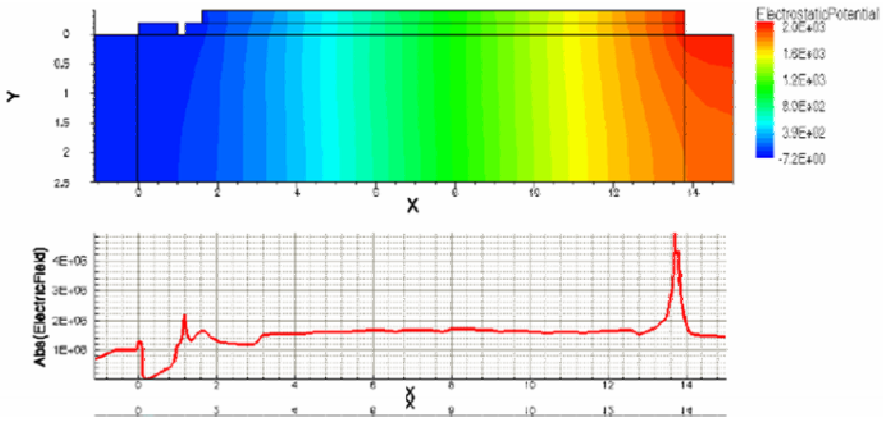

A multi-pad field plate allows an almost complete control on the electric field shape. The 10 different field plate contacts are positioned at 1 μm distance, starting from the drain contact towards the gate contact. Each contact has a length of 200 nm and the voltage difference between two adjacent pads is 200 V (the first one is drain connected while the last one is grounded). In the lower panel the calculated electric field along the channel is shown. As shown, beside the drain-end peak, the electric field is quite flat and does not show peaks.
The device is quite difficult to process from a technological point of view because of the multiple connection required to manage the pads.
Such geometry at now is under patenting.

Non Conventional Field Plate geometries doping FP

S-D distance = 18 um

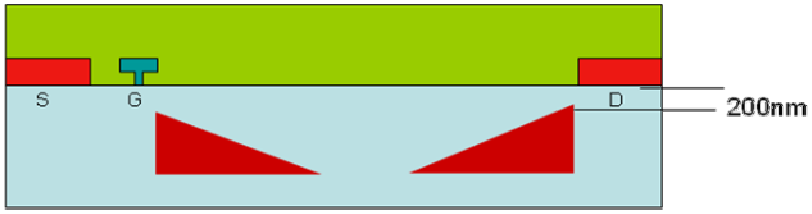

depth	extension	
0.2000000	1	BV= 16.67080
0.2000000	2	BV= 16.50034
0.2000000	3	BV= 16.09701
0.2000000	4	BV= 151.1743
0.2000000	5	BV= 143.0242
0.2000000	6	BV= 149.7367
0.2000000	7	BV= 139.2638
0.2000000	8	BV= 14.78276
0.6000000	1	BV= 631.1660
0.6000000	2	BV= 528.5830
0.6000000	3	BV= 459.0453
0.6000000	4	BV= 455.4968
0.6000000	5	BV= 296.8407
0.6000000	6	BV= 189.6718
0.6000000	7	BV= 111.5582
0.6000000	8	BV= 55.57491
1.000000	1	BV= 734.3137
1.000000	2	BV= 681.3251
1.000000	3	BV= 540.8333
1.000000	4	BV= 378.5522
1.000000	5	BV= 356.7921
1.000000	6	BV= 339.1126
1.000000	7	BV= 151.3551
1.000000	8	BV= 81.26596
1.400000	1	BV= 846.4019
1.400000	2	BV= 638.5830
1.400000	3	BV= 562.9353
1.400000	4	BV= 479.4584
1.400000	5	BV= 336.4133
1.400000	6	BV= 240.4154
1.400000	7	BV= 158.3248
1.400000	8	BV= 84.82941
1.800000	1	BV= 693.7225
1.800000	2	BV= 788.3047
1.800000	3	BV= 545.0026
1.800000	4	BV= 472.3321
1.800000	5	BV= 295.0069
1.800000	6	BV= 167.6619
1.800000	7	BV= 86.36862
1.800000	8	BV= 27.45126

The model works and should in principle offer the same advantages of the slant FP. Other simulations are required to optimize the doping geometry.

Non conventional FP geometries Multiple FP

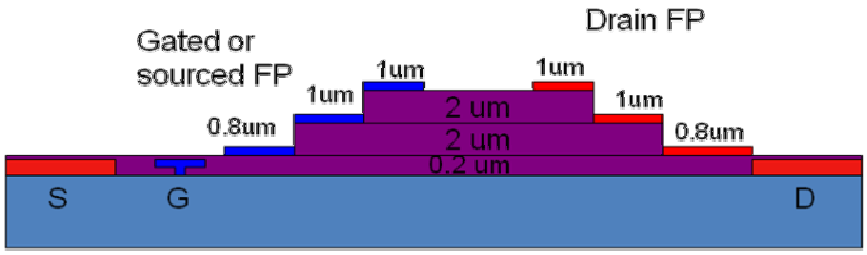

LDS=14um

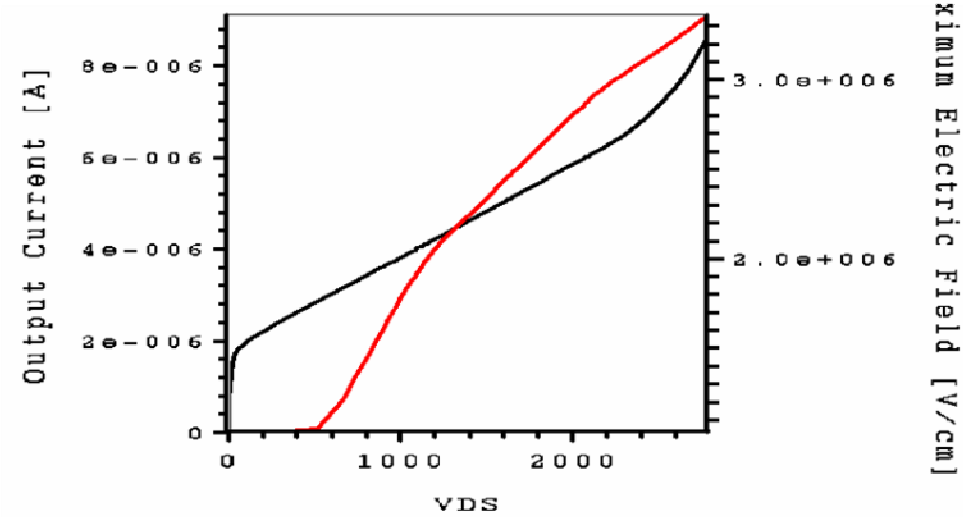

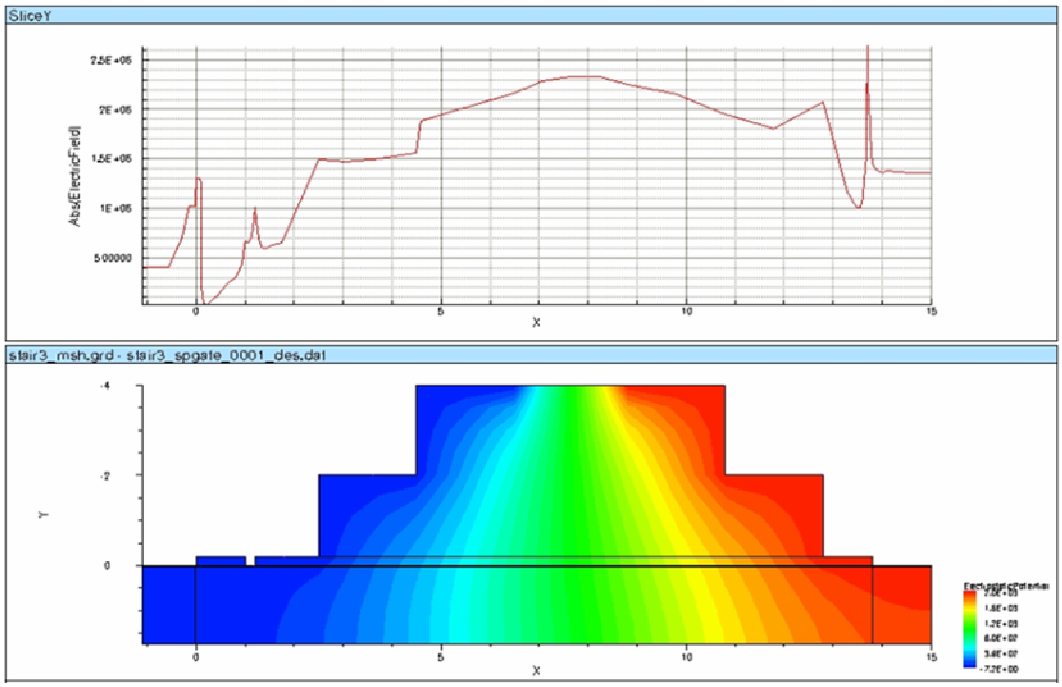

V_{DS}=2000V

Non conventional FP geometries: fingered with modulated deepness and resistive FP

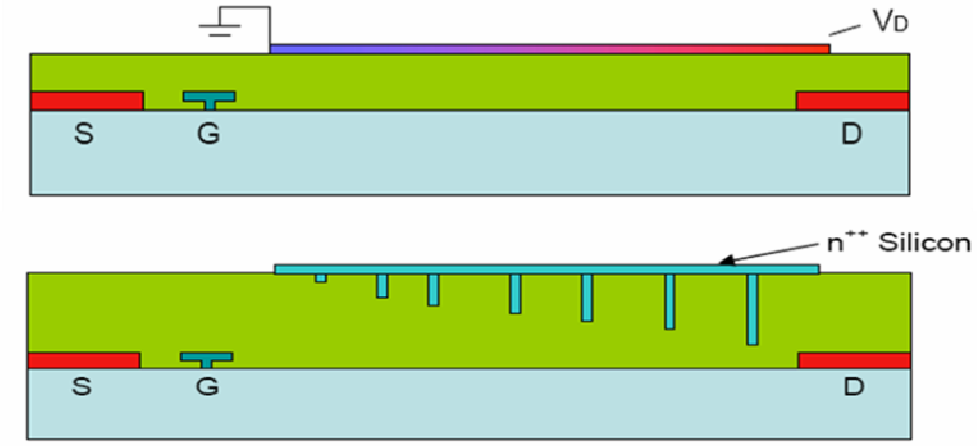

Chapter 6

Optimisation Matrix

We can sumerize the results presenteded in the previous sections in a matrix form. In this Optimization Matrix (Fig. 6.1) we summarize the obtained results showing which optimization approaches are good or bad for important figures of merit, namely I_{DSS}, g_m, cut-off frequency (f_T) and breakdown voltage (V_{BD}). A particular remark has to be devoted to the Back Contact: this technique can be implemented also together with the other techniques offering its breakdown and thermal advantages.
In figure 6.2 we report a similar matrix for non conventional FP geometries where the double FP is considered as the standard.

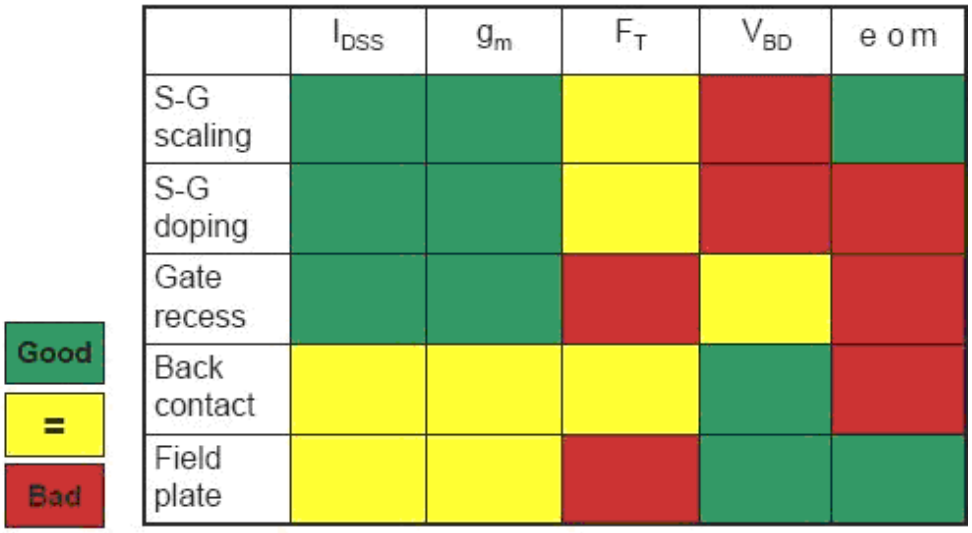

Fig. 6.1.: Optimization matrix for GaN-HEMTs. “eom” stands for ease of manufacture.

FP technique	Effectiveness	Design difficulties	Processing difficulties
Double FP technique			
Triple FP technique			
Multipad			
Multiple FP			
Fingered FP			
Doping FP	???		
Back Contact			

Fig. 6.2.: Optimization matrix for GaN-HEMTs Field Plated structures. For design difficulties we mean the correct design of the FP geometry, while for processing difficulties we mean the ease of manufacture.

Chapter 7

Schottky diode simulations

7.1 INTRODUCTION

Schottky rectifiers are a key element of inverter modules because of their high switching speeds and low switching losses, which are important for improving the efficiency of inductive motor controllers and power supplies. In power conversion applications, GaN power Schottky diodes have numerous advantages over more conventional Si rectifiers, achieving a maximum electric field breakdown strength over 10 times larger and on-state resistance (R_{ON}) approximately 400 times lower at a given voltage. These characteristics have made GaN devices potential candidates in power conditioning in large industrial motors, pulsed power for avionics and electric ships, in solid-state drivers for heavy electric motors, and in advanced power management and control electronics. Both GaN and SiC power Schottky diodes have shown faster turn-on than comparable Si devices.
While excellent reverse blocking voltages (*V*B) have been achieved in lateral GaN rectifiers on sapphire (*V*B up to 9.7 kV), these devices have limited utility because of their poor thermal characteristics and low on-state current. The reverse breakdown voltages in all GaN rectifiers reported to date are still limited by avalanche breakdown at defects and/or surfaces.
The use of a Guard Ring geometry should provide a sufficient reduction of the surface current in order to increase the breakdown voltage using non planar devices. In this way it would be possible o reach high BV with an high ON-current and quick switch-on time.

7.2 DEVICE GEOMETRY

The simulated device structure is shown in figure 7.1. The length of the contacts are free parameters, while the n-doped region can have a $5 \cdot 10^{17}$ cm^{-3} or $1 \cdot 10^{18}$ cm^{-3} donor concentration. The height of the NID region can range from 1 μm to 5 μm. The Schottky contact barrier height is 1.3 eV. The guard ring contact will have in each simulation a fixed voltage of -0.5 V while its barrier height will be 2 eV.

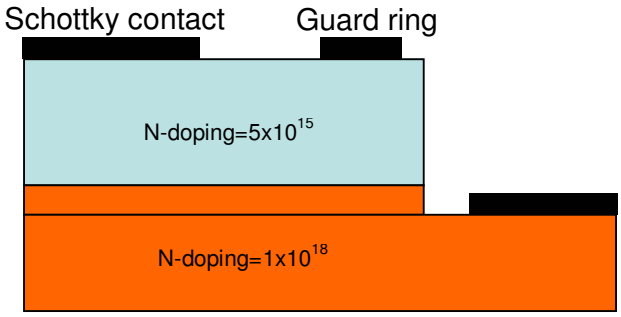

Figure 7.1:Schematic representation of the simulated devices.

7.3 FORWARD CHARACTERISTICS

A first set of simulations have been performed whose geometries has been reported in table 7.1.

Schottky contact length [µm]	Schottky-G.Ring distance [µm]	Guard Ring length [µm]	G.Ring - Ohmic contact distance [µm]	Doping [cm^{-3}]
600	100	50	10	1e18
100	100	50	10	1e18
600	100	50	10	5e17
600	10	400	10	1e18

Table 7.1: Geometries of the simulated devices for forward characteristics determination.

In Figure 7.2 the obtained forward characteristics are shown. According to our simulations, while the threshold is the same for all the studied devices, the forward current densities are not. The dimension of the guard ring is highly increasing the on resistance of the devices, even more than the n-doping.
Looking at figure 7.3 it is possible to have a deeper insight in the carriers dynamic at 5 V forward bias. Almost all the current from the Schottky contact to the Ohmic contact is flowing from the border of the Schottky contact towards the n-doped region. The collected current accumulate in the doped region having its maximum at the edge of the mesa. It is interesting to notice the presence of a large amount of current at the border of the mesa structure which may affect high frequency behaviour of the device.

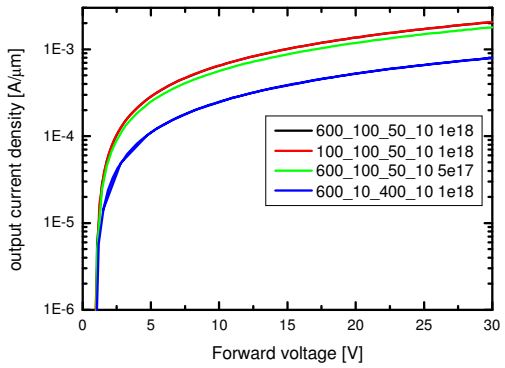

Figure 7.2: forward characteristics of simulated devices.

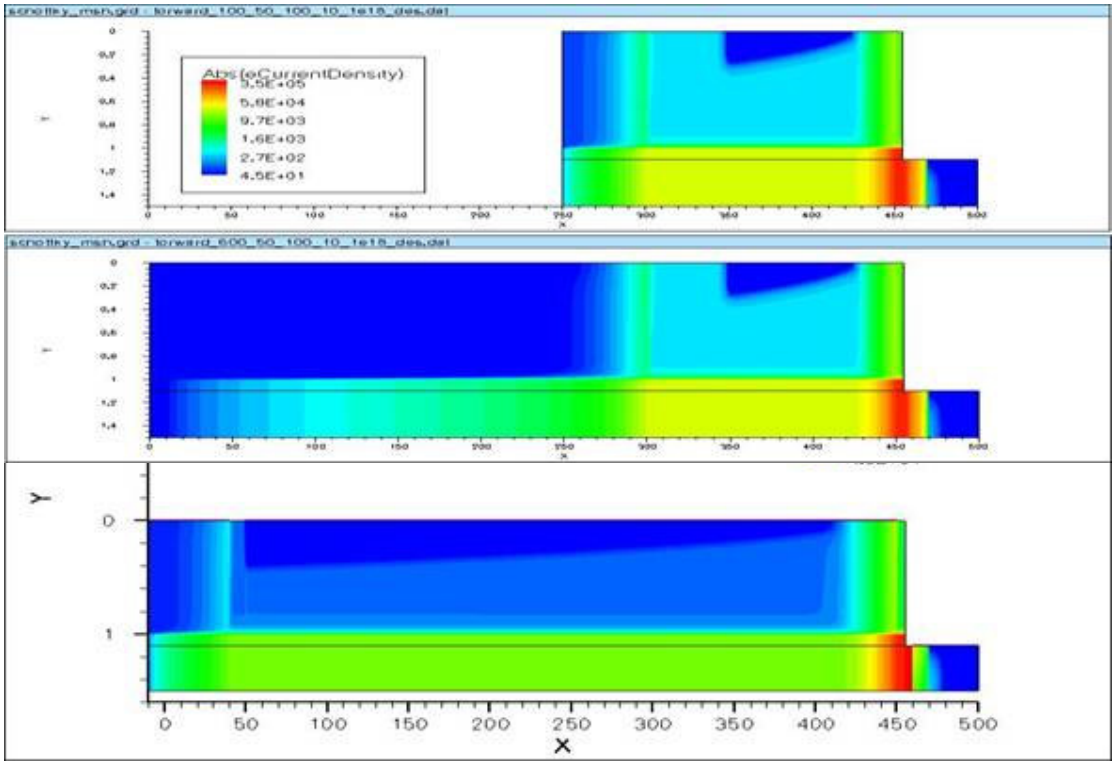

Figure 7.3: Current densities for three devices geometries, the notation is the same of table 7.1: a) 100-100-50-10; b) 600-100-50-10; c) 100-10-400-10.

7.4 Breakdown Voltage and Field Plates

In order to study the breakdown dynamics of the Schottky diodes we used as the starting point a device with the following geometry: the length of the Schottky contact is 600 µm; the distance between the Schottky contact and the guard ring is 50 µm; the length of the guard ring is 100 µm; the distance between the ring and the mesa is 5 µm; and 5 µm is the distance between the mesa and the ohmic contact. The guard ring contact voltage has been fixed for all simulation at -0.5 V.

For this device, we found a breakdown voltage around -150 V (see figure 7.4). In order to increase the breakdown voltage we consider a field plate at the Schottky contact edge. This is motivated by the observation that the maximum electric field occur at the edges of the Schottky contact. Thus, a FP technique should smooth this electric field similarly to the HEMT FP discussed in the previous sections.

For this purpose we consider a passivation layer over the top of the device to place the FP. Several simulation where performed with a passivation thickness of 10nm, 200nm and 400nm, respectively. On the top of this layer a field plate of 1 µm, 10 µm or 20 µm connected with the Schottky contact has been applied. We also investigated the possibility of two different thickness of the passivation layer, in order to get a double field plate effect.

The obtained results are shown in figure 7.4. As it is possible to observe, the most effective field plate is 10µm long with a passivation thickness of 200nm. The advantages obtained with a double field plate look too small to be interesting, as they will require a more complicate processing of the devices.

The subsequent step has been to vary the vertical dimension of the device: we made the undoped region length of 2 µm, 3 µm, 4 µm and 5 µm, keeping the same field plate structure in all the cases (10 µm long on 200 nm SiN thickness): the breakdown threshold increases up to -536 V, -670 V, -715 V and -850 respectively.

Using a doubled passivation thickness on the 5 µm undoped region device, that is 400 nm of SiN, it is possible to obtain an even higher BV, that is near -975V.

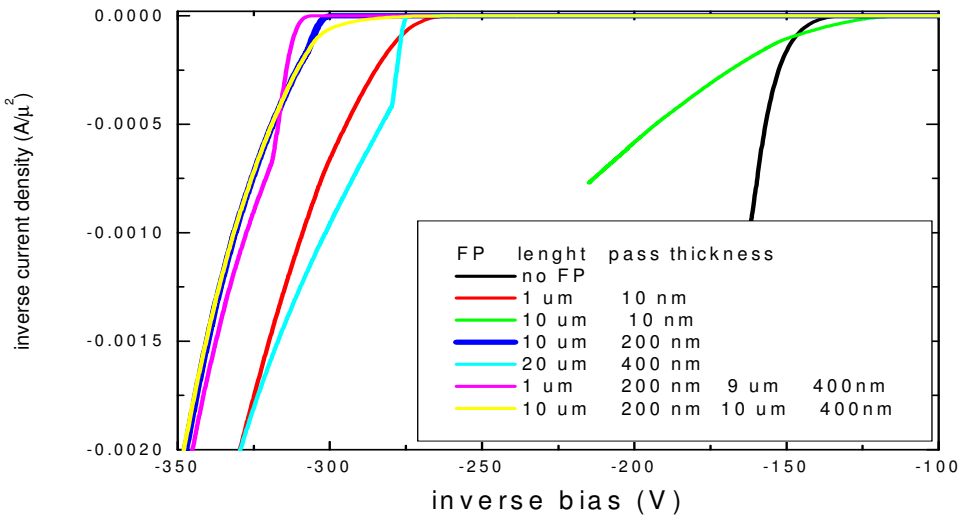

Figure 7.4: Reverse current and breakdown threshold for different FP applied.

The best geometry for devices without field plates but where the guard ring distance from other contacts is a free parameter has also been studied. The main results of this study can be summarised in figure 7.5: **The only parameter affecting the breakdown voltage is the Schottky contact-Guard ring distance** while guard-ring ohmic contact distance and the presence of the guard ring itself are not influencing the device breakdown voltage.
Overall results are reported in table 7.2.

X [μm]	BV [v]
10	-163,3
50	-174,08
150	-174,5
200	-187,7
250	-176,22
300	-185,15
400	-203,2
600	-209,75

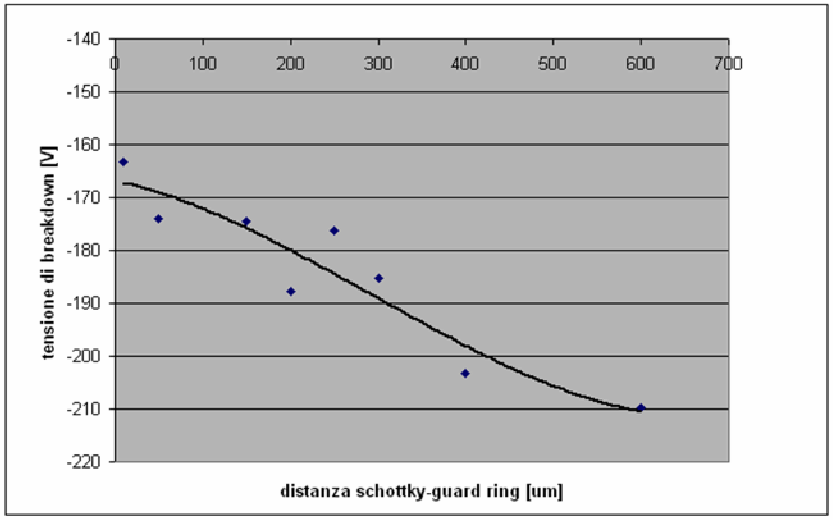

Figure 7.5: Breakdown Voltage as a function of the schottky-guard ring distance.

Breakdown Voltage[V]	Schottky Length [um]	Guard ring distance [um]	Guard ring length [um]	Omich-Guard ring [um]
-161,47	600	10	100	10
-162,25	600	10	100	50
-171,5	600	50	100	10
	600	50	100	50
	600	50	400	10
-171,64	600	50	400	50
-161,23	600	10	400	10
	600	10	400	50

-163,35	100	10	100	10
-163,29	100	10	100	50
-174,08	100	50	100	10
-175,21	100	50	100	50
-173,99	100	50	400	10
	100	50	400	50
-163,3	100	10	400	10
	100	10	400	50

Table 7.2: breakdown voltage as a function of the device geometry.

CHAPTER 8

Simulation Tools And Area to be addressed

8.1 KEY AREA TO BE ADDRESSED

Here is a list of the area which are still under investigation and whose development will follow in the forthcoming collaboration.

a) Source to Gate distance. The downscaling of this distance has to be studied for lengths shorter than 200 nm. Here overshooting phenomena are expected to play an important role and device behaviour can change significantly for both linearity and maximum gain.
b) Source-Gate doping. A high doping in AlGaN between Source and Gate will lead to an increase of the carriers in the device, with consequent increase of the output current and transconductance. However the influence of the depth of the doping and its extension up to the Gate has to be addressed.
c) Enhancement mode GaN based HEMTs and AlInGaN barrier HEMTs. These new kind of GaN HEMTs are showing interesting characteristics. Their potentialities have to be addressed.
d) Field plate techniques. Non conventional FP techniques constitutes a wide field of investigation. A thorough analysis is still required.
e) The back contact study in not complete: different topologies of this technique has to be compared.
f) The "VIA" structure has to be studied and compared with other techniques.
g) The reliability issue is still under development.

8.2 SIMULATION ACCURACY

The accuracy of simulations has improved since the beginning of the cooperation. As new physical details about the studied devices has been understood, the experimental behaviour has become more reproducible.
Moreover new simulations tools has become available allowing the possibility to get an even more physical simulation of the device, including in the drift diffusion scheme spontaneous and piezo polarization and phonons effect as well.
Up to now, when quantum correction are not necessary (that is the case for the dimensions of the devices we are studying) the accuracy of simulations can be quite high. The experimental data fitting depends only on the provided data and the time (human and simulative) devoted to it.

CHAPTER 9

Conclusions

In this thesis we have presented our research activities and achievements within the ATHENA project.
The aim of the project was to complement the Athena programme with modelling and simulation of GaN HEMTs and Schottky diodes for microwave applications.
We managed to produce exhaustive documentation and complete understanding of the surfaces related phenomena. Our approach followed two different ways: from one side we developed a physical model to describe strain and the effect of passivation, from the other side we enquired the reasons for GaN-HEMTs performances degradation. In this way we were able to address all the phenomena which are limiting the devices performances under RF regime and to address which effects can be overcome with the aid of passivation. We isolated the different effects of fixed polarization charges at the interfaces, surface trapping and bulk trapping.
The first one is the main cause of the premature saturation and it is due to the intrinsic polarization of the material which lead to charge accumulation at the hetero-interface. The effect of the negative top interface which is acting like a floating gate can be partially suppressed with the passivation technique.
Trap localisation at the AlGaN/GaN interface leads to current collapse phenomenon. A state of the art passivation will highly reduce their density and thus the power slump induced by RF gate switching.
The presence of deep acceptor traps in the GaN bulk induce the Gate lag phenomenon which leads to a RF behaviour depending on the initial applied bias. The only efficient way to solve this phenomenon is the use of p-doping or of back contacts.

Our simulation analysis was applied to the study of the HEMTs topology influence on the source access resistance. Our main finding, from this point of view, is the influence of the source to gate distance scaling on the HEMT performances. A downscaling of the Source-Gate distance can improve device performance, enhancing the output current and the device transconductance. The main reason for this effect is related to the peculiar dynamic of electrons in the GaN based HEMTs which leads to a non saturated velocity regime in the source access region, even for high drain applied voltages. On the contrary, the Gate-Drain distance does not affect the output current within the analysed devices geometries. Based on these results, new optimization strategies for GaN HEMTs could be defined.

Particular attention has also been paid to the effect of a back contact: it will reduce self heating effects, it will decrease the density of GaN bulk trapped electrons, and, associated with GaN thinning, will also increase the breakdown voltage.
A detailed analysis has also been devoted to the study of Field Plates geometries in order to increase the device maximum output power of the studied devices, including also non conventional Field Plate geometries: we performed a large amount of simulations finding the best geometry in order to increase the maximum power. Moreover we demonstrate the possibility to further increase the the breakdown voltage with the use of a fingered field plate.
The breakdown phenomenon has been widely studied together with AC performances for all the optimization techniques we have found in order to define a optimization matrix. This matrix includes I_{DSS}, g_m, f_T, V_{BD}.
Schottky diodes geometries are also investigated: with the application of an optimized field plate on the Schottky contact it is possible to achieve near 1 kV Breakdown Voltage for a geometry which is experimentally accessible now.

Chapter 10

Presentations and Publications

A. Di Carlo, S. Russo, F. Sacconi and M.Povolotskyi, "**Monte Carlo and Drift-Diffusion simulations for GaN-HEMTs optimizations**", invited talk at the Ferdinand Brown Institute, Berlin 7 April 2006

S. Russo, and A. Di Carlo, "**Influence of the Source-Gate Distance on the AlGaN/GaN HEMT Performance**" Electron Devices, IEEE Transactions on Volume 54, Issue 5, May 2007 Page(s):1071 – 1075.

S. Russo, and A. Di Carlo, "**Scaling effects in AlGaN/GaN HEMTs: Comparison between Monte Carlo simulations and experimental data**" Journal of Computational Electronics, 5, 109 – 113 (2006).

S.Russo, A.Di Carlo, J.Das, M.Germain, Gustaaf Borghi, **"AlGaN/GaN HEMTs with Backside Schottky Contact"** WOCSDICE 2007 - May 20 - 23, Venice Italy.

S.Russo, A.Di Carlo, **"Influence of a Back Contact on AlGaN/GaN HEMT Performance"** Wide-bandgap Semiconductor Quantum Structures August 27 - September 1, 2006 / Monte Verità (Ascona), Switzerland.

A. Di Carlo, S. Russo, F. Sacconi and M.Povolotskyi, talks at ESA meetings held in Norvick 2005-2006 and Paris 2005.